COUPLED ARRAY OF CO_2 WAVEGUIDE LASERS

Thesis by

Yongfang Zhang

In Partial Fulfillment of the Requirements

for the Degree of

Doctor of Philosophy

California Institute of Technology

Pasadena, California

1993

(Defended May 11, 1993)

ACKNOWLEDGEMENT

It has been a great five years for me at Caltech and in the research group of Professor W. B. Bridges. Not only I have learned a great deal from Dr. Bridges in the way of thinking and experimental skills in research, but I have also seen in him a man of extensive knowledge, sharp insight and caring personality. The originality displayed in class by my Caltech professors will always be an inspiration in my career. I also learnt a lot from my fellow students, especially Arthur Sheiman and Finbar Sheehy, through all the discussions we have had and all the things we have done together.

I am also grateful to Reynold Johnson, who has been there all the time when I have needed help in the lab; to Laura Rodriguez and Connie Rodriguez, who as Dr. Bridges' secretaries, have provided much assistance in the mysterious formalities of Caltech.

I want to express my gratitude to Caltech as an institution, for creating an interactive environment for study and exposing me to the cutting edge of modern science and technology. My only regret is not having enough time to grasp all the opportunities I have been given.

I am very thankful to the Air Force Office of Scientific Research and the Hughes Aircraft Company for their financial support of my thesis project.

My deepest gratitude goes to my parents who, in those extremely difficult years when I grew up, gave me love and encouragement and steered me in the right directions. I am also very grateful to my wife Liangfang and my son Charley for their love, their support, and the hopes we cherish together. I am so glad that we have been close together all these years in our new lives in America.

ABSTRACT

In this thesis, arrays of coupled waveguide CO_2 lasers and some aspects of coupled laser arrays in general are studied. The in-phase coupled supermode is desirable in almost all laser applications, but it is not always obtained in laser arrays. An analytical method is used to investigate the spatial overlap between the distributions of laser mode intensity and the medium gain and cavity loss, and its effect on mode. The result shows that the gain/loss in the inter-element regions of an array determines which supermode to oscillate: for a fixed gain level a high loss favors the out-of-phase supermode while a low loss, the in-phase supermode. Several waveguide CO_2 lasers, including wall-slot coupled ceramic and metal arrays, uncoupled arrays, single slab waveguide lasers, and slab waveguide lasers with unstable resonators were tested for their modal properties and power output. A new structure, the groove-coupled strip waveguide CO_2 laser array, that favors the in-phase coupled supermode was proposed and tested in two, three and five-element arrays. The experimental results showed that this new structure yields robust, pure in-phase coupled mode operation with a reasonable amount of output power.

Also discussed in this thesis are the coupling of Gaussian waves in active media, the experiments in an all-metal, ridge-waveguide CO_2 laser pumped by microwaves, a new type of optical switching based on the unique properties of a coupled twin-element laser, and two-dimensional array of gas discharge lasers.

TABLE OF CONTENTS

CHAPTER 1. INTRODUCTION

CHAPTER 2. THEORETICAL ANALYSIS OF MODE COMPETITION AND STABILITY WITH SPATIAL LOSS/GAIN DISTRIBUTIONS

CHAPTER 3. EXPERIMENTAL STUDIES OF CO_2 LASER ARRAYS OF HOLLOW BORE WAVEGUIDES

CHAPTER 4. SLAB WAVEGUIDE CO_2 LASERS

CHAPTER 5. A NEW STRUCTURE—THE GROOVE-COUPLED STRIP WAVEGUIDE ARRAY

CHAPTER 6. MICROWAVE EXCITED CO_2 WAVEGUIDE LASER

CHAPTER 7 SOME NEW IDEAS ON FUTURE RESEARCH

LIST OF ILLUSTRATIONS

Chapter 1. Introduction

Chapter 2. Theoretical Analysis of Mode Competition and Stability with Spatial Loss/Gain Distributions

Chapter 3. Experimental Studies of CO_2 Laser Arrays of Hollow Waveguides

Chapter 4. Slab Waveguide CO_2 Lasers

Chapter 5. A New Structure—The Groove-Coupled Strip Waveguide Array

Chapter 6. Microwave Excited CO_2 Waveguide Laser

Chapter 7. Some New Ideas on Future Research

LIST OF TABLES

Chapter 2. Theoretical Analysis of Mode Competition and Stability with Spatial Loss/Gain Distributions

Chapter 4. Slab Waveguide CO_2 Lasers

CHAPTER 1. INTRODUCTION

§1.1 Some Thoughts on the Discovery and Development of Lasers

The history of lasers is filled with the emergence of new ideas and breaks with prevailing thought in both theoretical and experimental fronts.

Before Albert Einstein, it was the popular belief in the scientific community that atoms can only absorb or spontaneously radiate light. Einstein[1] pointed out the possibility of stimulated emission, where atoms in excited states can be made to radiate light before the spontaneous emission can happen when they are irradiated with photons. This is a basic principle necessary for laser operation, and it was proposed in 1916, 44 years before the first laser was made. The concept of stimulated emission was first applied only to spectroscopy, not to the amplification of light because people blindly assumed that thermal equilibrium was the norm for all matter, which dictates that any higher energy level should have less population than the lower levels by the law of Boltzman distribution. In the early 1950's Townes[2], Weber[3], and Prokhorov and Basov[4] proposed independently that a population inversion, which defies thermal equilibrium, was possible to achieve, demonstrated its use in producing microwave amplification and a microwave oscillator. Breaking another prevailing thought barrier, that a resonator should be of the size of the radiation wavelength, Schawlow and Townes[5] published their ideas of using a Fabry-Parot resonator hundreds of thousand wavelength in size to provide feedback for a light oscillator. When Maiman succeeded in demonstrating the first laser[6], a pulsed ruby laser in 1960, he also was at odds with the popular belief that ruby was not suitable for laser action. And, ironically, this belief was fostered by a calculation made by Schawlow[7].

Today laser action has been demonstrated in all phases of matter, with

wavelengths from the far infrared to soft x-ray regions. And they are used in all aspects of life. Still, it is necessary for us to keep open minds in our research in order to expand to new frontiers of laser technology and application.

§1.2 A Brief Introduction to CO_2 Lasers

The first CO_2 laser was made by Patel et al.[8] in 1964. It has gained tremendous popularity since because of its versatility. It is used in material processing, surgery, lidar, communication, and a host of other applications. To this day it has the biggest commercial market (in dollars) of any type of laser, and its application and commercial market is still expanding and at a rate about the same as diode lasers[9].

CO_2 lasers' power outputs range from a few watts to megawatts; it can be operated in continuous or pulse mode; it can be excited by a variety of means: electric discharge, thermal dynamic, chemical and electron beam, with the most popular being electric discharge excitation.

There are four vibration modes associated with the linear carbon dioxide molecule, the symmetric stretching mode, two bending modes in perpendicular orientations, and the asymmetric stretching mode. They are illustrated in Figure 1. The laser related transition diagram of the rotational-vibrational energy states for electric discharge excited lasers is given in Figure 2. The most common laser transition originate from the 00^01 state of the excited asymmetric vibrational mode, and end at either 10^00 of the symmetric vibration mode (10.6 μm band) or the 02^00 bending mode (9.6 μm band). Each of these vibrational energy levels is actually composed of many rotational energy levels. The laser transition usually

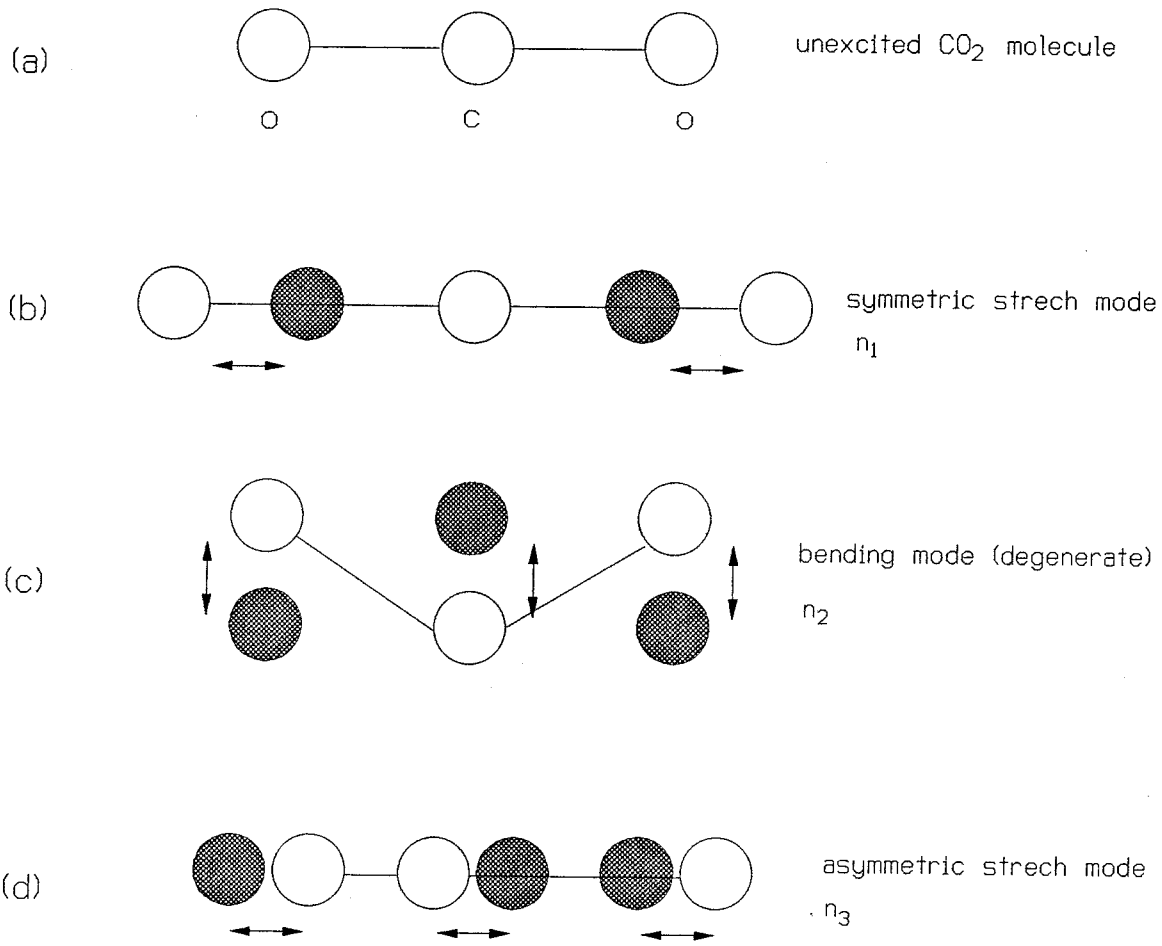

Figure 1. Illustration of CO_2 molecule vibrational modes. (a) Unexcited molecule, (b), (c) and (d) The three normal modes of vibration.

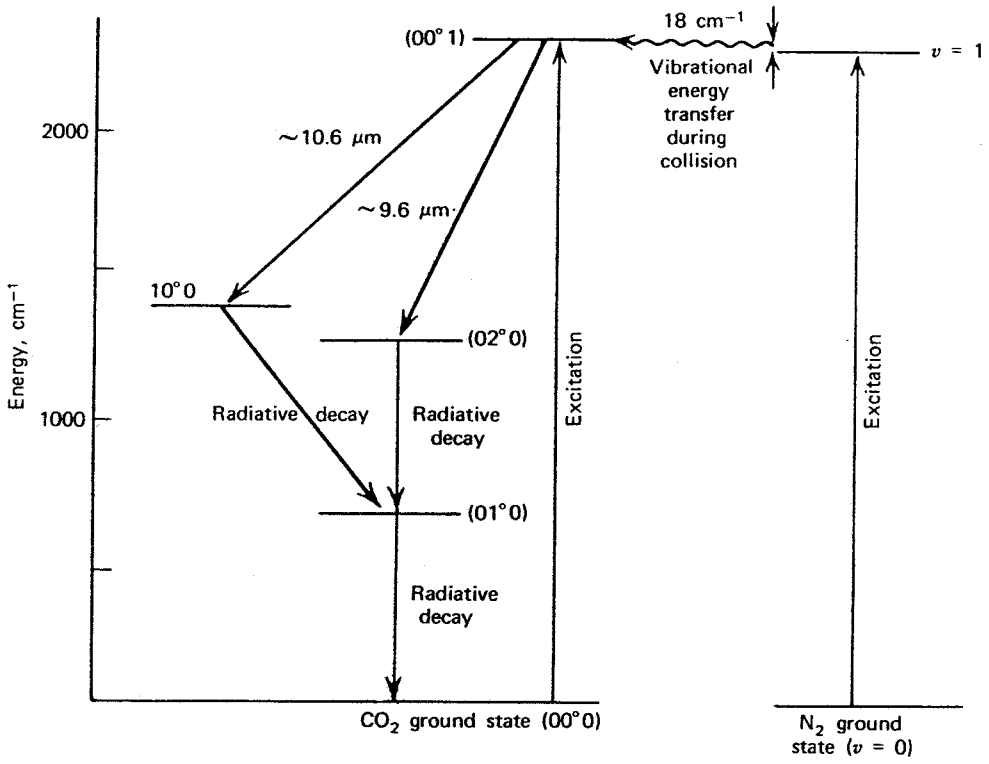

Figure 2. Laser related vibrational levels of the CO_2 molecule, and the laser related N_2 ground level and first vibrational state $N_2^*(\nu=1)$. Source: Ref. 14.

occurs between only a single pair of these rotational levels at a time, due to competition and relaxation among the rotational states. This is depicted in Figure 3. The upper energy level, 00^01, has a longer collision lifetime than the two lower energy levels, 10^00 and 02^00. This makes CO_2 gas system ideal for a laser system. N_2 is added to the gas mixture used in electric discharge excited CO_2 lasers to make the electron-to-CO_2 energy transfer much more efficient. This occurs because the first excited vibration level of nitrogen molecule, $N_2^*(\nu=1)$, has coincidentally nearly the same energy as the CO_2 00^01 level, and the vibration levels of N_2 have large excitation cross-sections at the electron energy of around 2 ev, that is characteristic of the CO_2+N_2 glow discharge. Being a metastable state, the radiative lifetime of $N_2^*(\nu=1)$ is very long, on the order of seconds. In collisions with CO_2 molecules, N_2 readily transfers its vibrational energy to the CO_2 00^01 level. The net effect is that the energy is "funneled" from the discharge electric to the electrons, then to the Nitrogen vibrational manifold, and finally to the single CO_2 level. Helium is also typically added to the gas mixture of CO_2 lasers because it has a large heat conductivity, reducing the gas temperature and helping to depopulate the lower laser level via collision[10].

In discharge-excited gas lasers, there is always an optimum pressure at which the the electron temperature is at the best to excite the molecules so that the laser power output is maximum. The scaling laws of discharges[11] states that one can change the characteristic size of the discharge vessel (usually the diameter or distance between nearest walls) and keep the electron temperature the same by following some simple rules to adjust other parameters of the discharge, most importantly, the pressure. One rule is that the electron temperature will remain constant if the pressure P varies inversely with the bore diameter D; that is

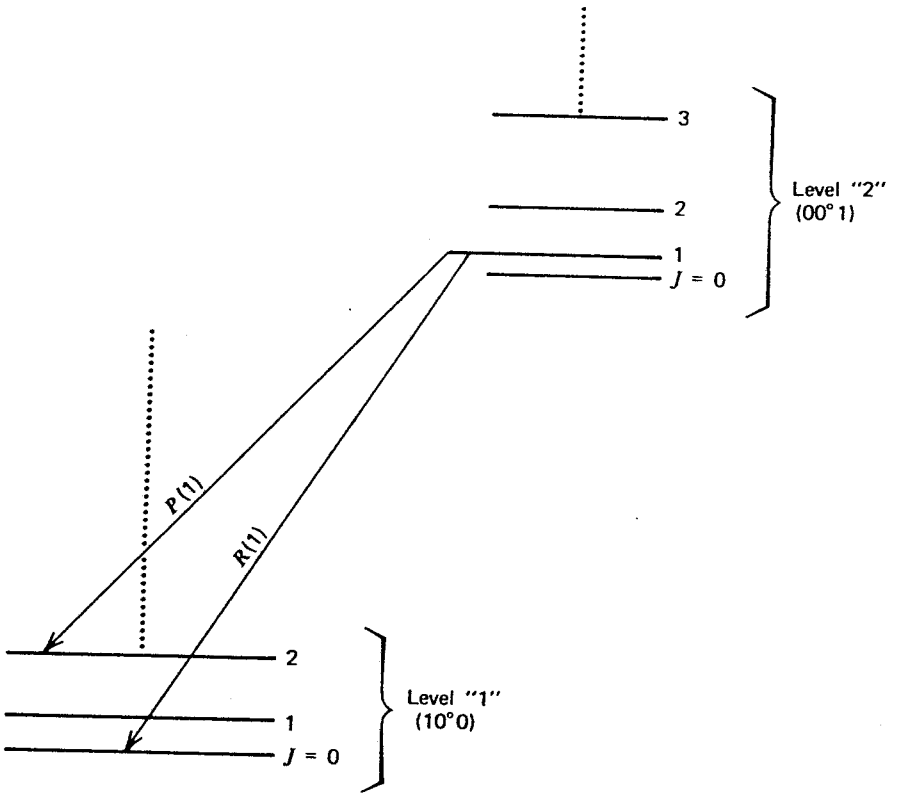

Figure 3. The rotational levels within each vibrational level near the 10.6 μm laser transition of a CO_2 molecule. Source: Ref. 14.

PD = constant. A waveguide CO_2 laser has a small bore, and will thus require a higher pressure. This will collision-broaden the gain line width and increase the saturation intensity. One consequence of this is that the laser power density increases. Another consequence is a wider range of operating frequency. Thus waveguide CO_2 lasers are suited for compact devices, wide frequency tunable sources, and mode-locked short pulse generators. An undesirable consequence of the higher pressure in small diameter lasers is the higher electric field and higher voltage required for the discharge. This disadvantage was alleviated by means of transverse RF excitation, demonstrated by Laakman[12].

The interest in waveguide laser arrays developed as higher powers were desired. Although one can increase the length of a waveguide laser to obtain higher power, the device becomes a thin, long shape that is hard to implement and handle, and more importantly, the higher power density thus obtained will increase the optical flux on the laser mirrors, which will eventually fail. However, if one can put several waveguide lasers in parallel and phase-couple them, one can obtain a high power, coherent device in a small size with a reasonable aspect ratio, and with power density in the laser optics basically the same as in a single waveguide laser.

§1.3 Coupled Mode Systems

Probably the first reported observation of two modes coupled together occurred in 1665[13], when Christiaan Huygens noticed that two pendulum clocks hanging close together on the same wall would tick precisely together for an arbitrarily long period of time. He attributed the mechanism of coupling to small vibrations transmitted through the wall. In all large systems composed of smaller, similar systems, there are interactions among these small systems. That is why now, more than two hundred years after Huygens' discovery, there is scarcely a branch of science whose theory does not involve wave motion with its related concepts of modes, energy flow, and mode coupling.

A complicated coupled oscillation system can often be divided into a number of isolated elements, whose equations of motion can be solved and the solutions expressed in terms of normal modes. The original complex system is then assumed to be made up of the individual elements *weakly coupled together.* The mutual coupling perturbs the state of each elements slightly, and this perturbation serves to "coordinate" the individual elements into the single complex system. This complex system of identical elements has more than one overall solution even if all the constituent elements are in the same mode, because of the various ways of coupling among the elements. These overall solutions of the system in the optical field can be called "supermodes," a term used by Yariv[14] and others in the case of coupled waveguides.

In our theoretical treatment of the coupled laser array, we used the concept of supermodes and calculated the competition between two such supermodes: the all-in-phase coupled mode and the alternating in-and-out-of-phase coupled mode. Based on the analysis, we conceived and tested a new coupled waveguide array structure which favors the all-in-phase coupled supermode.

§1.4 Outline of the Following Chapters

In Chapter 2 we set out from Maxwell's equations to treat the spatial mode competition problem. Our approach includes the spatial distribution of the competing modes, the spatial variations of the medium gain and the loss in the laser array. Numerical examples of coupled CO_2 laser array systems are carried out and the results show that the loss in the inter-element region of the coupled is the main factor in determining the mode of oscillation.

Chapter 3 gives experimental results for wall-slot coupled arrays, including the pressure-power relationship, the waveguide material factor (same geometry with different wall materials), and the supermode behavior. We compared the oscillation modes of different inter-element region loss with the analysis in Chapter 2.

Chapter 4 discusses the results of our study of slab waveguide lasers, the modes of this particular structure, the effects different dielectric coatings have on the waveguide losses, the relationship between the laser power output and surface finishes, etc.

Chapter 5 presents our new structure, the groove-coupled strip waveguide CO_2 laser array. This is a successful attempt to reduce the loss in the inter-element region and to ensure the oscillation of the all-in-phase coupled mode. It is related to the mode competition studies in Chapter 2. We obtained pure in-phase coupled mode operation in arrays of two, three and five elements. The concept of coupling between free-space Gaussian modes is proposed.

Chapter 6 reports our on-going experiment on microwave excited CO_2 waveguide lasers, based on an idea of making an all metal, low cost device. Waveguiding is provided for both the microwave and the laser by the same structure.

Chapter 7 describes two proposals for future study: a new type of optical switch based on the supermode of two-element array lasers; and two-dimensional arrays of phase coupled CO_2 lasers.

REFERENCES

1. A. Einstein, "Strahlungs-Emmission und Absorption nach der Quantentheorie," Verh. der. D. Physika. Ges. **18** (1916) 318; for an English translation see B. L. van der Waerden edited, Sources of Quantum Mechanics, North-Holland, Amsterdam, 1967.

2. J. P. Gordon, H. J. Zeiger and C. H. Townes, "Molecular microwave oscillator and new hyperfine structure in the microwave spectrum of NH_3," Physical Review Vol. 95, p. 282, 1954.

3. J. Weber, "Amplification of microwave radiation by substances not in thermal equilibrium," Transactions IRE Professional Group on Electron Devices PGED-3 p. 1, June 1953.

4. N. G. Basov and A. M. Prokhorov, "3-level gas oscillator," Zh. Eksp. Teor. Fiz (JETP) Vol. 27, p. 431, 1954.

5. A. L. Schawlow and C. H. Townes, "Infrared and Optical Masers," Physical Review Vol. 112, p. 1940, 1958.

6. T. H. Maiman, "Stimulated Optical Radiation in Ruby," Nature, Vol. 187, p. 493, August 6, 1960.

7. A. Schawlow, at the First International Quantum Electronics Conference, indirectly quoted by T. Maiman in the book, Laser Pioneer Interviews, by the staff of Lasers & Applications, High Tech Publications, 1985.

8. C. K. N. Patel, W. L. Faust and R. A. McFarlane, "CW Laser Action on Rotational Transitions of the Σ_u^+—Σ_g^+ vibrational band of CO_2," Bull. Am. Phys. Soc. 9, 500, 1964.

9. D. Kales, "Review and Forecast of Laser Markets: 1993," Laser Focus World, Vol. 29, No. 1, pp. 70–88, January 1993.

10. C. S. Willett, Introduction to Gas Lasers: Population Inversion Mechanisms, Pergamon Press, 1974.

11. K. D. Laakman, U.S. Patent No. 4,169,251, September 25, 1976.

12. R. L. Abrams and W.B. Bridges, "Characteristics of Sealed-off Waveguide CO_2 lasers," IEEE J. Q. E., Vol. QE-9, No. 9, pp. 940–946, September 1973.

13. See the account given by M. Sargent III, M. O. Scully and W. E. Lamb, Jr., Laser Physics, Addison Wesley, 1974.

14. A. Yariv, Quantum Electronics, 3rd edition, John Wiley & Sons, 1989.

CHAPTER 2. THEORETICAL ANALYSIS OF MODE COMPETITION AND STABILITY WITH SPATIAL LOSS/GAIN DISTRIBUTIONS

§2.1 Introduction

Laser mode selection has been an important part of the study and application of lasers since their discovery in 1960. Traditionally, the selection of modes is necessary to obtain a single frequency with a single transverse mode, which in single-channel lasers is usually the fundamental Gaussian mode, and in laser arrays, the all-in-phase coupled array mode[1,2]. Recent progress in active photonic switching and logic devices uses the different modes to represent different states, with the oscillation being switched back and forth between the modes to change the state[3,4]. These modes can be the longitudinal or transverse modes of the laser cavity, including polarization. Usually the different modes have different field distributions in the laser cavity. The differences in their overlap with the gain and loss distributions over the cavity volume play an important role in their competition with each other. Understanding of these differences is then fundamental to the proper selection of lasing modes. The original theoretical work on multimode laser operation was done by Sargent, Scully and Lamb[5], and we are greatly indebted to them. However, because they did not include spatial dependence in their laser modes, medium gain, and loss, their theory can not be directly applied to the coupled-laser arrays. Also, their treatment was limited to cases where the laser intensity is much smaller than the saturation intensity. In this chapter we develop a general analytical method, which takes into account both spatial distributions and strongly staturated gain, to help understand better the interactions between the modes and the medium, and their effects on mode competition. Conditions on gain and loss distributions for competing modes to oscillate are derived with special attention to the in-phase

coupled and the out-of-phase coupled modes of an array. Section 2 of this Chapter considers the spatial variation of cavity loss and gain, and gain saturation. Differential equations for laser mode development in time are derived. Section 3 studies the stability of single mode solutions in a two-mode system. Conditions on gain and loss distribution for competing modes to oscillate are derived. Section 4 presents one-dimensional numerical examples of competition between the in-phase and out-of-phase array modes in a two-channel CO_2 laser array. Section 5 extends the theory to two-dimensional numerical examples to reveal some finer aspects of mode competition as affected by the array structure. Section 6 discusses the stability of a two-mode state for the laser system.

§2.2 Model and Theory

We concentrate our attention to the coupled-waveguide laser array, the general form of which is shown in Figure 1. For this model, Maxwell's equations can be written as:[6]

$$\left.\begin{aligned} \nabla \times \mathbf{H} &= \mathbf{J} + \epsilon \frac{\partial \mathbf{E}}{\partial t} + \frac{\partial}{\partial t}\mathbf{P}_{\text{laser}} \\ \nabla \times \mathbf{E} &= -\mu \frac{\partial \mathbf{H}}{\partial t} \end{aligned}\right\}, \tag{1}$$

where the current density $\mathbf{J}$ is introduced to account for the loss that is not in resonance with the laser (for example, the mirror transmission loss or the loss introduced by the waveguide boundaries) and $\mathbf{P}_{\text{laser}}$ is the complex polarization of the medium that resonates with the laser.

Using a normal mode expansion of a resonator field, the total electric and magnetic fields are:

$$\left.\begin{aligned} \mathbf{E}(\mathbf{r},t) &= \sum_j e_j(t)\ \phi_j(\mathbf{r}) \\ \mathbf{H}(\mathbf{r},t) &= \sum_j h_j(t)\ \psi_j(\mathbf{r}) \end{aligned}\right\}, \tag{2}$$

where the modal functions $\phi_j(\mathbf{r})$ and $\psi_j(\mathbf{r})$ are dimensionless and are normalized to the volume of the cavity, V:

$$\left.\begin{aligned} \frac{1}{V}\int_V \phi_j(\mathbf{r})\cdot\phi_k(\mathbf{r})\ dv &= \delta_{kj} \\ \frac{1}{V}\int_V \psi_j(\mathbf{r})\cdot\psi_k(\mathbf{r})\ dv &= \delta_{kj} \end{aligned}\right\}, \tag{3}$$

The loss and resonant polarization become:

$$\left.\begin{aligned} \mathbf{J} &= \sigma(\mathbf{r})\sum_j e_j(t)\phi_j(\mathbf{r}) \\ \mathbf{P}_{\text{laser}}\ (\mathbf{r},t) &= \epsilon_0\chi(\mathbf{r},\omega)\sum_j e_j(t)\ \phi_j(\mathbf{r}) \end{aligned}\right\}. \tag{4}$$

The formal conductance $\sigma(\mathbf{r})$ and the complex dielectric susceptibility $\chi(\mathbf{r})$ are functions of space here, while in reference 6 they are treated as constants. The first of Maxwell's equations becomes:

$$\sum_j h_j(t)\nabla\times\psi_j(\mathbf{r}) = \sigma(\mathbf{r})\sum_j e_j(t)\phi_j(\mathbf{r}) + [\epsilon+\epsilon_0\chi(\mathbf{r})]\sum_j \dot{e}_j(t)\ \phi_j(\mathbf{r})\ . \tag{5}$$

Taking the time derivative of equation (5), we obtain:

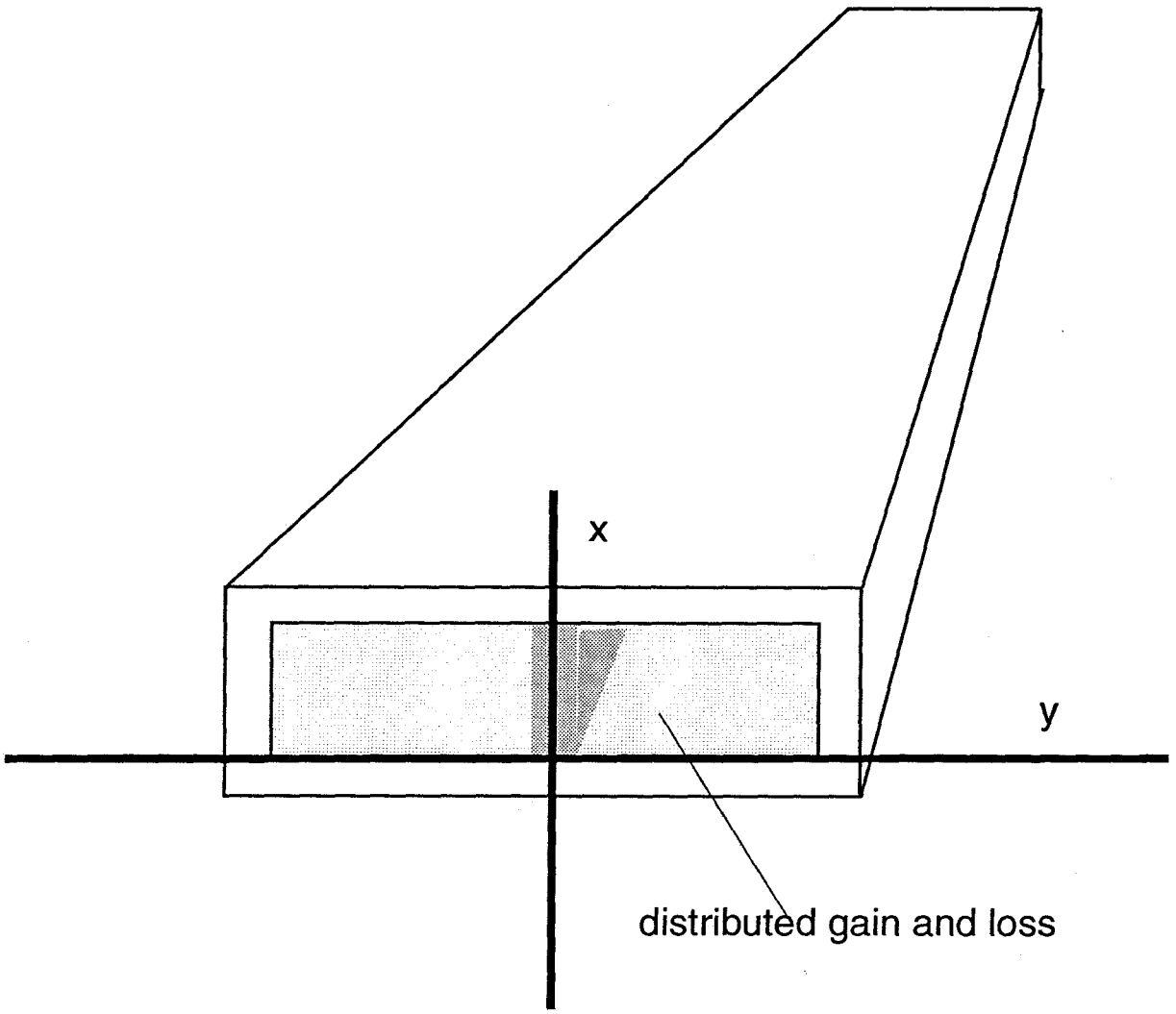

Figure 1. Schematic showing the general structure of the waveguide array of two channels with distributed gain and loss.

$$\sum_j \dot{h}_j(t)\ \nabla\times\psi_j(\mathbf{r}) = \sigma(\mathbf{r})\sum_j \dot{e}_j(t)\ \phi_j(\mathbf{r}) + [\epsilon+\epsilon_0\chi(\mathbf{r})]\sum_j \ddot{e}_j(t)\ \phi_j(\mathbf{r})\ . \tag{6}$$

The normal-mode field functions satisfy Maxwell's equations for the empty unperturbed resonator, which is charge free, uniform and passive and lossless:

$$\left.\begin{aligned}\nabla\times\phi_j(\mathbf{r}) &= -i\omega_{j0}\mu\psi_j(\mathbf{r})\\ \nabla\times\psi_j(\mathbf{r}) &= i\omega_{j0}\epsilon\phi_j(\mathbf{r})\end{aligned}\right\}, \tag{7}$$

where ω_{j0} is the normal frequency for the j-th mode in the passive cavity. Substituting the first line of (7) into the second of Maxwell's equations, we have:

$$e_j(t) = -\frac{i}{\omega_{j0}}\dot{h}_j(t)\ . \tag{8}$$

Using equations (7) and (8) in (6):

$$\sum_j -{\omega_{j0}}^2\epsilon\ e_j(t)\ \phi_j(\mathbf{r}) = \sigma(\mathbf{r})\sum_j \dot{e}_j(t)\ \phi_j(\mathbf{r}) + [\epsilon+\epsilon_0\chi(\mathbf{r})]\sum_j \ddot{e}_j(t)\ \phi_j(\mathbf{r}). \tag{9}$$

Rearranging the above, we obtain:

$$-\epsilon\sum_j\left({\omega_{j0}}^2\ e_j+\ddot{e}_j\right)\phi_j(\mathbf{r}) = \sum_j[\sigma(\mathbf{r})\dot{e}_j+\epsilon_0\chi(\mathbf{r})\ \ddot{e}_j]\ \phi_j(\mathbf{r}). \tag{10}$$

Multiplying both sides of the above equation with $\frac{1}{V}\phi_k(\mathbf{r})$ and integrating over the volume V, we have

$$-\epsilon\left({\omega_{k0}}^2\ e_k+\ddot{e}_k\right) = \sum_j\left(\sigma_{jk}\dot{e}_j(t)+\epsilon_0\chi_{jk}\ddot{e}_j(t)\right)\phi_j(\mathbf{r})\ , \tag{11}$$

where

$$\left.\begin{aligned} \sigma_{jk} &\equiv \frac{1}{V}\int_V \sigma(\mathbf{r})\ \boldsymbol{\phi}_j(\mathbf{r})\cdot\boldsymbol{\phi}_k(\mathbf{r})\ \mathrm{dv} \\ \chi_{jk} &\equiv \frac{1}{V}\int_V \chi(\mathbf{r})\ \boldsymbol{\phi}_j(\mathbf{r})\cdot\boldsymbol{\phi}_k(\mathbf{r})\ \mathrm{dv}. \end{aligned}\right\} \tag{12}$$

We may write $e_j(t)$ as:

$$e_j(t) \equiv \frac{1}{2}\, e_{j0}(t)\, e^{-i\omega_j t} + \text{c.c.}\ , \tag{13}$$

where ω_j is the laser frequency, and $e_{j0}(t)$ is the slowly-varying part of the time-dependent $e_j(t)$. We assume e_{j0} varies slowly, $|\ddot{e}_{j0}| \ll \omega_j\ |\dot{e}_{j0}(t)|$, so that the second derivative of $e_j(t)$ can be approximated as:

$$\ddot{e}_j(t) \simeq \frac{1}{2}[-\omega^2 e_{j0}(t) + i2\omega\ \dot{e}_{j0}(t)]\ e^{i\omega t}\ , \tag{14}$$

and equation (11) can be written as:

$$-\epsilon[(\omega_{j0}{}^2 - \omega_j{}^2)\ e_{j0} + i2\omega_j\ \dot{e}_{j0}] =$$

$$\sum_k [(i\omega_k e_{k0} + \dot{e}_{k0})\sigma_{kj} + (-\omega_k{}^2 e_{k0} + i2\omega_k \dot{e}_{k0})\epsilon_0 \chi_{kj}]. \tag{15}$$

We see from this equation that the spatial variation of the loss and gain causes direct coupling between different modes. This is distinct from the kind of coupling that is our main object, in which the interaction is via the cross saturation of one laser mode by another. Because laser gain and loss can never be

truly uniform in space, direct coupling will in general be present and must be given due consideration. Only under the conditions that the orthogonality between the modes is not violated by the presence of $\chi(\mathbf{r})$ and $\sigma(\mathbf{r})$ in equation (12), so that the following inequalities are true, can the direct coupling terms be omitted:

$$\left.\begin{aligned} \int_V \phi_k(\mathbf{r})\cdot\phi_j(\mathbf{r})\,\chi(\mathbf{r},\omega)\,dv \ll \int_V \phi_j(\mathbf{r})\cdot\phi_j(\mathbf{r})\,\chi(\mathbf{r},\omega)\,dv \\ \int_V \phi_k(\mathbf{r})\cdot\phi_j(\mathbf{r})\,\sigma(\mathbf{r})\,dv \ll \int_V \phi_j(\mathbf{r})\cdot\phi_j(\mathbf{r})\,\sigma(\mathbf{r})\,dv \end{aligned}\right\} \; k\neq j\,. \quad (16)$$

Inequalities (16) are well-satisfied in the cases we are treating here, where $\sigma(\mathbf{r})$ and $\chi(\mathbf{r})$ are nearly symmetrical functions, and the k-th and j-th modes are of the opposite spatial symmetry. If $\sigma(\mathbf{r})$ and $\chi(\mathbf{r})$ are exactly symmetrical, then the left sides of inequalities (16) becomes exactly zero. With this approximation, equation (11) becomes:

$$\left[\, i2\omega_j\left(1+\frac{\chi_j}{n^2}\right) + \frac{\sigma_j}{\epsilon}\,\right]\dot{e}_{j0} = \left[-{\omega_{j0}}^2+{\omega_j}^2+\frac{\chi_j}{n^2}\,{\omega_j}^2 - i\,\frac{\omega_j\sigma_j}{\epsilon}\right] e_{j0}\,, \quad (17)$$

where n is the index of refraction of the medium in the absence of the gain, and σ_j and χ_j are shorthand for σ_{jj} and χ_{jj}, respectively. The modal susceptibility χ_j can be further written in terms of its real and imaginary parts:

$$\chi_j \equiv \frac{1}{V}\int_V \phi_j(\mathbf{r})\cdot\phi_j(\mathbf{r})\,\chi(\mathbf{r},\omega)\,dv = \frac{1}{V}\int_V \phi_j(\mathbf{r})\cdot\phi_j(\mathbf{r})\left(\chi'(\mathbf{r}) - i\,\chi''(\mathbf{r})\right)dv. \quad (18)$$

When we require $\dot{e}_{j0}=0$ in equation (17), we obtain the steady state solution, which then yields two conditions for steady state laser oscillation; the first one is

for phase and the second one for amplitude:

$$\omega_j = \frac{\omega_{j0}}{\sqrt{1+\frac{Re(\chi_j)}{n^2}}} , \qquad Im(\chi_j) = \frac{\sigma_j}{\epsilon_0 \omega_j} . \tag{19}$$

To simplify the problem further, we consider only homogeneously-broadened media, since in Section 4 of this chapter we will treat CO_2 lasers, which are essentially homogeneously broadened. From Appendix A, the imaginary part of χ_j can be written as:

$$Im(\chi_j) = -\frac{1}{V}\int_V |\phi_j(\mathbf{r})|^2 \ \chi''(\mathbf{r})\ dv \ = \frac{1\, nc}{V\omega_j}\int_V \frac{\gamma_0(\mathbf{r})\ |\phi_j(\mathbf{r})|^2\ dv}{1+\frac{\sum_k e_{k0}e^*_{k0}\phi_k(\mathbf{r})\cdot\phi_k(\mathbf{r})}{2\eta I_s}} , \tag{20}$$

where the wave impedance of space filled with dielectric material of permitivity $\epsilon = \epsilon_r\epsilon_0$ is defined as:

$$\eta \equiv \sqrt{\frac{\mu_0}{\epsilon_r\epsilon_0}} . \tag{21}$$

The small signal gain γ_0 [m^{-1}] and homogeneous saturation intensity I_s [W/m^2] are defined in the usual way; their relations to the laser atomic parameters are given in Reference 6, and are cited in Appendix A. Solving equation (17) for $\dot{e}_{j0}$ and substituting the laser frequency ω_j as given in the first of (19) we obtain:

$$\dot{e}_{j0} = \frac{(\frac{\chi_j}{n^2}\omega^2 - i\frac{\omega\sigma_j}{\epsilon})}{i2\omega(1+\frac{\chi_j}{n^2}) + \frac{\sigma_j}{\epsilon}}\ e_{j0} . \tag{22}$$

For most gas-laser media, $|\chi| \ll 1$, and thus $|\chi_j|/n^2 \ll 1$ in equation (22). If the cavity loss is small, i.e., $\sigma_j/\epsilon \ll 2\omega$, the denominator above is effectively $i2\omega_j$ and equation (22) can be further simplified. Using these simplifications and expanding the electric field using equation (2) in (20), equation (22) becomes:

$$\dot{e}_{j0} = \frac{1}{2}\left(\frac{\mathrm{Im}(\chi_j)}{n^2}\omega - \frac{\sigma_j}{\epsilon}\right)e_{j0} = \left[\frac{c}{2nV}\int_V \frac{\gamma_0(\mathbf{r})|\phi_j(\mathbf{r})|^2 dv}{1 + \frac{\frac{1}{2\eta}\sum_k e_{k0}e^*{}_{k0}\phi_k(\mathbf{r})\cdot\phi_k(\mathbf{r})}{I_s}} - \frac{\sigma_j}{2\epsilon}\right] e_{j0} \cdot \qquad (23)$$

It is seen clearly in equation (23) that the coupling between the modes now exists in the form of cross saturation through all the $e_{k0}e_{k0}{}^*$ terms. This is the basis of mode competition. In expressing (22) in the form of (23), some assumptions about the population inversion were made, which are described in more detail in the derivation of the population inversion in Appendix A.

Equation (23) is the differential equation for the laser field coefficients, each including phase and amplitude. In mode competition cases we are only concerned with the change in the intensity of a laser mode, an easily measurable quantity, so we will write equations for the intensities of each mode using equation (23). In doing so we also eleminate information on the phase of each mode that we are not interested in and further simplify the treatment. The intensity coefficient for the j-th mode is defined as:

$$b_j \equiv \frac{e_{j0}e_{j0}{}^*}{2\eta} . \qquad (24)$$

It represents the power density [W/m^2] in the j^{th} mode. The differential equation for b_j may be found from equation (23):

$$\dot{b}_j = \frac{d}{dt}\left(\frac{e_{j0}e_{j0}^*}{2\eta}\right) = \frac{1}{2\eta}(\dot{e}_{j0}e_{j0}^* + e_{j0}\dot{e}_{j0}^*) =$$

$$= 2\left[\frac{c}{2nV}\int_V \frac{\gamma_0(\mathbf{r})|\phi_j(\mathbf{r})|^2 dv}{1 + \frac{\sum_k b_k \phi_k(\mathbf{r})\cdot\phi_k(\mathbf{r})}{I_s}} - L_j\right] b_j \,. \quad (25)$$

In deriving (25), we used the fact that the square bracket term is real. We also introduced a modal loss coefficient as:

$$L_j \equiv \frac{\sigma_j}{2\epsilon} \,. \quad (26)$$

§2.3 Mode Stability Analysis

We can now use the results of the previous section to investigate the stability of a given mode when it is possible for a second mode, i.e., one with a different transverse field distribution, to oscillate. We make the following assumptions:

1. There are only two modes that are sufficiently near the threshold to be appreciably excited. The total field is then:

$$\mathbf{E}(\mathbf{r},t) = e_1(t)\,\phi_1(\mathbf{r}) + e_2(t)\,\phi_2(\mathbf{r}) \,. \quad (27)$$

2. The z-dependence of the modal fields is a simple standing wave, and is the same for all modes considered, since we have assumed they all have the same

longitudinal mode number. Thus the spatial hole-burning resulting from this fine standing-wave pattern in the z-direction does not favor one mode over another and can be ignored. Integrals over volumes can thus be replaced by integrals over the transverse cross-section.

3. The gain does not depend on z, so the integral in equation (25) is only affected by the field variations in the transverse direction (x,y);

4. The loss $\sigma(\mathbf{r})$ is divided into a spatially-varying part and a constant part:

$$\sigma(\mathbf{r}) = \sigma'(\mathbf{r}) + \sigma_0. \tag{28a}$$

With these assumptions, the effects of the localized loss and the distributed loss on laser mode competition can be separated. The modal loss is then:

$$L_j = \frac{1}{2\epsilon V}\int_V \sigma'(\mathbf{r})\ \phi_j(\mathbf{r})\cdot\phi_j(\mathbf{r})\ dv + \frac{\sigma_0}{2\epsilon} \equiv L'_j + L_0\ . \tag{28b}$$

To obtain steady-state solutions for equation (25), we require $\dot{b}_j = 0$ for $j = 1,2$. Then on the right hand side of equation (25) either the term in the square brackets is zero or b_j is zero. All possibilities considered, we have three non-trivial steady state solutions:

$$(b_1, b_2) = (f, 0), (0, g), \text{ or } (p_1, p_2). \tag{29}$$

It is necessary to analyze the stability of these solutions and find the conditions for them to be stable and unstable. We will only treat the single-mode solutions (f,0) and (0,g) in this section, since they are of more interest; two-mode oscillation will be the subject of Section 6 of this chapter. In our experiment, we did indeed

obtain oscillations corresponding to (f,0) and (0,g), as will be discussed in Chapter 3.

First, consider the stability of the state (f,0). Under perturbation (δ_1,δ_2), this state becomes $(f+\delta_1,\delta_2)$. We use equation (25) to study the dynamics of the perturbations δ_1 and δ_2:

$$\left.\begin{aligned}\dot{\delta}_1 &= 2\left[\frac{c}{2nS}\int_S \frac{\gamma_0(x,y)\,|\phi_1(x,y)|^2\,dxdy}{1+\dfrac{(f+\delta_1)|\phi_1(x,y)|^2+\delta_2|\phi_2(x,y)|^2}{I_s}} - L_1\right](f+\delta_1)\\ \dot{\delta}_2 &= 2\left[\frac{c}{2nS}\int_S \frac{\gamma_0(x,y)\,|\phi_2(x,y)|^2\,dxdy}{1+\dfrac{(f+\delta_1)|\phi_1(x,y)|^2+\delta_2|\phi_2(x,y)|^2}{I_s}} - L_2\right]\delta_2\end{aligned}\right\}. \quad (30)$$

Here, S is the total cross-sectional area of the laser cavity. Because the perturbation is very small, $f \gg |\delta_1|,\ |\delta_2|$, we can ignore all the second-order δ–terms in equation (30):

$$\dot{\delta}_1 \simeq 2\left\{\frac{c}{2nS}\int_S \frac{\gamma_0(x,y)\,|\phi_1(x,y)|^2}{1+\dfrac{f|\phi_1(x,y)|^2}{I_s}}\left[1-\frac{\delta_1|\phi_1(x,y)|^2}{I_s\left(1+\dfrac{f|\phi_1(x,y)|^2}{I_s}\right)}\right]dxdy - L_1\right\}(f+\delta_1). \quad (31)$$

The fact that (f,0) is a steady state solution implies that the saturated gain equals the total loss:

$$\frac{c}{2nS}\int_S \frac{\gamma_0(x,y)\,|\phi_1(x,y)|^2\,dxdy}{1+\dfrac{f|\phi_1(x,y)|^2}{I_s}} - L_1 = 0\,. \quad (32)$$

Equation (30) evolves into the following form:

$$\left.\begin{aligned}\dot{\delta}_1 &\simeq -\frac{cf}{nI_sS}\int_S \gamma_0(x,y)\ |\phi_1(x,y)|^2\ \frac{\delta_1|\phi_1(x,y)|^2}{\left[\,1+\frac{f|\phi_1(x,y)|^2}{I_s}\,\right]^2}\,dxdy \\ \dot{\delta}_2 &= 2\left[\frac{c}{2nS}\int_S \frac{\gamma_0(x,y)\ |\phi_2(x,y)|^2\,dxdy}{1+\frac{f|\phi_1(x,y)|^2}{I_s}} - L_2\right]\delta_2\end{aligned}\right\}. \tag{33}$$

We can write (33) in a matrix form by defining a vector δ:

$$\delta \equiv \begin{pmatrix}\delta_1 \\ \delta_2\end{pmatrix}.$$

The time derivation of δ is:

$$\dot{\delta} \equiv \begin{pmatrix}\dot{\delta}_1 \\ \dot{\delta}_2\end{pmatrix} = \begin{pmatrix}A & B \\ C & D\end{pmatrix}\begin{pmatrix}\delta_1 \\ \delta_2\end{pmatrix}. \tag{34}$$

From (33), the matrix elements B and C are zero. Thus the eigenvalues for the operating matrix are A and D. If both of them are negative, then the vector δ will not grow, and the steady state (f,0) is stable; if either A or D is positive, (f,0) will be unstable. We see from (31):

$$\left.\begin{aligned}A &= -\frac{cf}{nI_sS}\int_S \frac{\gamma_0(x,y)\ |\phi_1(x,y)|^4}{[\,1+\frac{f|\phi_1(x,y)|^2}{I_s}\,]^2}\,dxdy\ < 0 \\ D &= 2\left[\frac{c}{2nS}\int_S \frac{\gamma_0(x,y)|\phi_2(x,y)|^2}{[\,1+\frac{f|\phi_1(x,y)|^2}{I_s}\,]^2}\,dxdy - L_2\right]\end{aligned}\right\}. \tag{35}$$

The sign of D is not known until $\gamma_0(x,y)$, $\phi_1(x,y)$, $\phi_2(x,y)$ and $\sigma'(x,y)$ are specified. But because A is negative, the sign of D determines the stability of the solution (f,0): if it is positive (negative), this state is unstable (stable).

Similar arguments obviously apply to the other single mode steady state (0, g), which becomes $(\delta_1,\ g+\delta_2)$ with perturbation. The equations are:

$$\left.\begin{aligned} \dot{\delta}_1 &= 2\left[\frac{c}{2nS}\int_S \frac{\gamma_0(x,y)\ |\phi_1(x,y)|^2\ dxdy}{1+\frac{g|\phi_2(x,y)|^2}{I_s}} - L_1\right]\delta_1 \\ \dot{\delta}_2 &\simeq -\frac{cg}{nI_sS}\int_S \gamma_0(x,y)\ |\phi_2(x,y)|^2\ \frac{\delta_2|\phi_2(x,y)|^2}{[\,1+\frac{g|\phi_2(x,y)|^2}{I_s}\,]^2}\ dxdy \end{aligned}\right\}. \qquad (36)$$

We define the self-saturated modal gain S_k and cross-saturated modal gain C_{kj}, both in unit of s^{-1}, as follows:

$$\left.\begin{aligned} S_k &\equiv \frac{c}{2nS}\int_S \frac{\gamma_0(x,y)\ |\phi_k(x,y)|^2\ dxdy}{1+\frac{\alpha_k|\phi_k(x,y)|^2}{I_s}} \\ C_{kj} &\equiv \frac{c}{2nS}\int_S \frac{\gamma_0(x,y)\ |\phi_j(x,y)|^2\ dxdy}{1+\frac{\alpha_k|\phi_k(x,y)|^2}{I_s}} \end{aligned}\right\} \ j,\ k=1,\ 2;\ j\neq k\ ;\quad \alpha_1\equiv f,\ \alpha_2\equiv g. \qquad (37)$$

These definitions are similar to those used by Tang et al.[4] Then we may summarize the conditions for the existence and stability of the j^{th} modes:

For the j^{th} mode to exist

$$S_j - L'_j - L_0 = 0. \tag{38a}$$

For the k^{th} mode to exist

$$S_k - L'_k - L_0 = 0. \tag{38b}$$

The stability of the j^{th} mode is determined by

$$C_{jk} - L'_k - L_0 \begin{cases} < 0 & \text{stable} \\ \\ > 0 & \text{unstable} \end{cases} \tag{38c}$$

The stability of the k^{th} mode is determined by

$$C_{kj} - L'_j - L_0 \begin{cases} < 0 & \text{stable} \\ \\ > 0 & \text{unstable} \end{cases} \tag{38d}$$

Thus, for a laser to have a single j^{th} mode, (38c) must be < 0 **and** (38d) must be > 0, and vice versa for a single j^{th} mode to exist.

§2.4 Numerical Examples

In this section we consider numerical examples using parameters typical of CO_2 waveguide lasers. The model chosen is an array of two channels coupled by a region with some loss, as shown in Figure 2a. The competition between the in-phase and out-of-phase coupled modes (or "super modes," as they are sometimes termed[6]) is considered, based on the stability of the (f,0) and (0,g) states.

The fields are assumed to vary only in the y-direction; they are assumed to be uniform in x-direction (Figure 2b). The small signal gain γ_0 is assumed to be a constant across the array. The loss distribution, which peaks in the coupling region, is also assumed to vary only with y, and its amplitude is changed to affect the mode competition (Figure 2c). The x-dimension is taken as 2 mm, and the y-direction as 6 mm. The small-signal gain γ_0 and loss coefficient that is equivalent to $2L_0/c$ are estimated for a CO_2 waveguide laser array to be 0.0012 mm^{-1} and 0.00034 mm^{-1}, respectively. The saturation intensity is taken from experimental data[8] as $I_s = 80$ [watt mm^{-2}] at pressures of around 110 torr. The following two functions are used to represent the general forms of the in-phase and out-of-phase coupled modes:

$$\left.\begin{aligned} \phi_1(y) &= c_1\{\exp[-(y-1.5)^2] + \exp[-(y+1.5)^2]\} \\ \phi_2(y) &= c_2\{\exp[-(y+1.5)^2] - \exp[-(y+1.5)^2]\} \end{aligned}\right\}, \qquad (39)$$

where $c_1 = 1.540$, $c_2 = 1.557$ are normalization constants. These modes are plotted in Figure 2b. Although they are not the actual modal solutions, these two functional forms resemble the general shapes of the in-phase and the out-of-phase modes, and the difference between them. When they are substituted into (16),

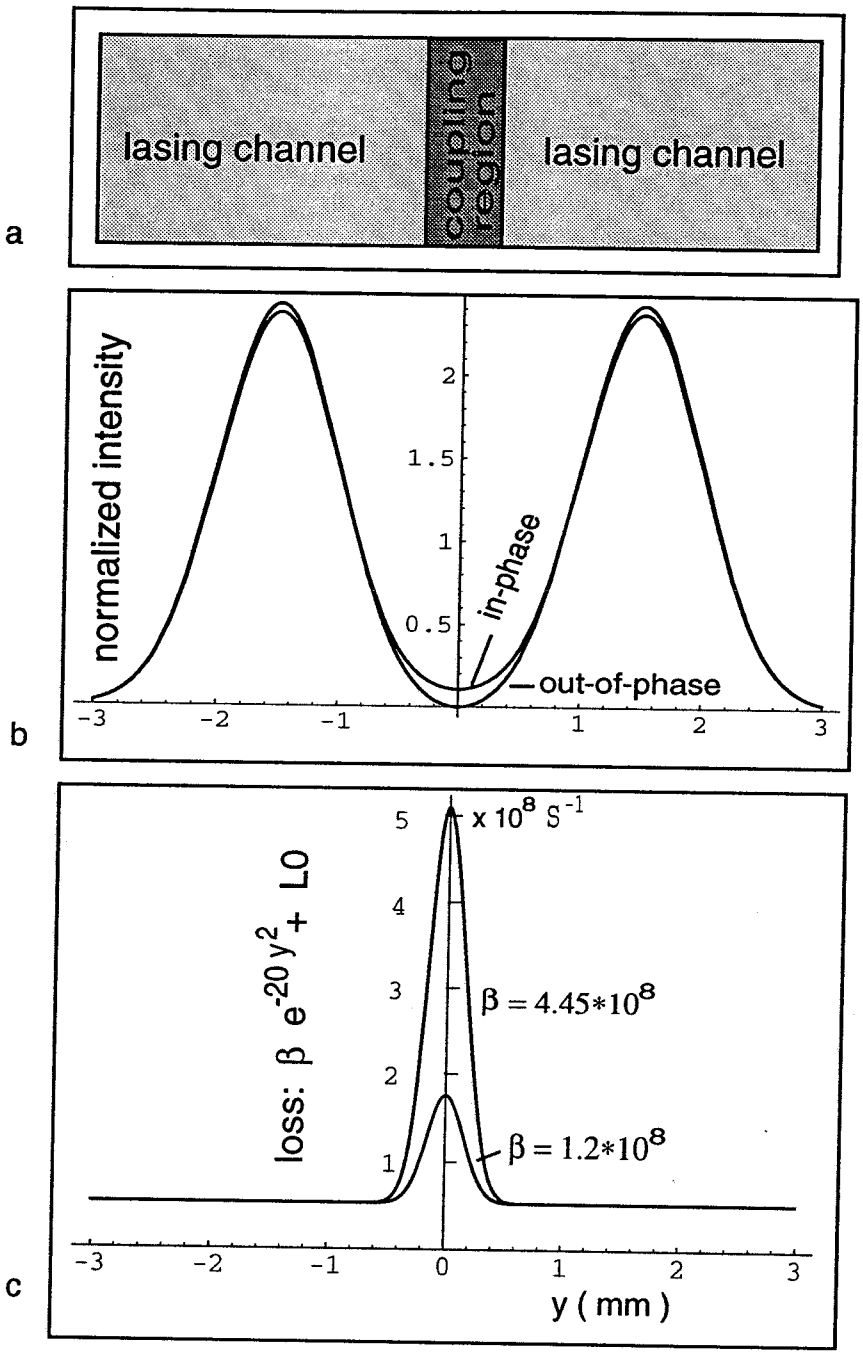

Figure 2. a) Schematic cross-section of the waveguide array; b) the assumed intensity distributions for the in-phase and out-of-phase coupled mode; c) the assumed loss function for two different values of β.

the left side yields zero. Thus the omission of the direct coupling terms in equation (15) is justified.

The spatially-varying loss is located at the center of the array where the two channels meet, and is assumed to be the following:

$$\frac{\sigma'(y)}{2\epsilon_0} = \beta \exp(-20y^2), \tag{40}$$

where β is a parameter with a unit of s^{-1}. We calculated the stability of the two array modes for two different values of β, 1.2×10^8 and 4.45×10^8. The total loss function for these two cases are plotted in Figure 2c. The results of the calculation are given in Table 1.

Table 1. Summary of Stability for the Two Array Modes

$\beta = 1.2\times10^8$	$\beta = 4.45\times10^8$
stable in-phase mode	**stable out-of-phase mode**
$S_1 - L_1 = 0$	$S_2 - L_2 = 0$
$C_{12} - L_2 = -7.6\times10^5[s^{-1}] < 0$	$C_{21} - L_2 = -1.1\times10^6[s^{-1}] < 0$
$f = 29.66\left[\frac{watt}{mm^2}\right]$	$g = 28.60\left[\frac{watt}{mm^2}\right]$
unstable out-of-phase mode	**unstable in-phase mode**
$S_2 - L_2 = 0$	$S_1 - L_1 = 0$
$C_{21} - L_1 = 2.7\times10^6[s^{-1}] > 0$	$C_{12} - L_2 = 6.9\times10^6[s^{-1}] > 0$
$f = 29.10\left[\frac{watt}{mm^2}\right]$	$g = 27.32\left[\frac{watt}{mm^2}\right]$

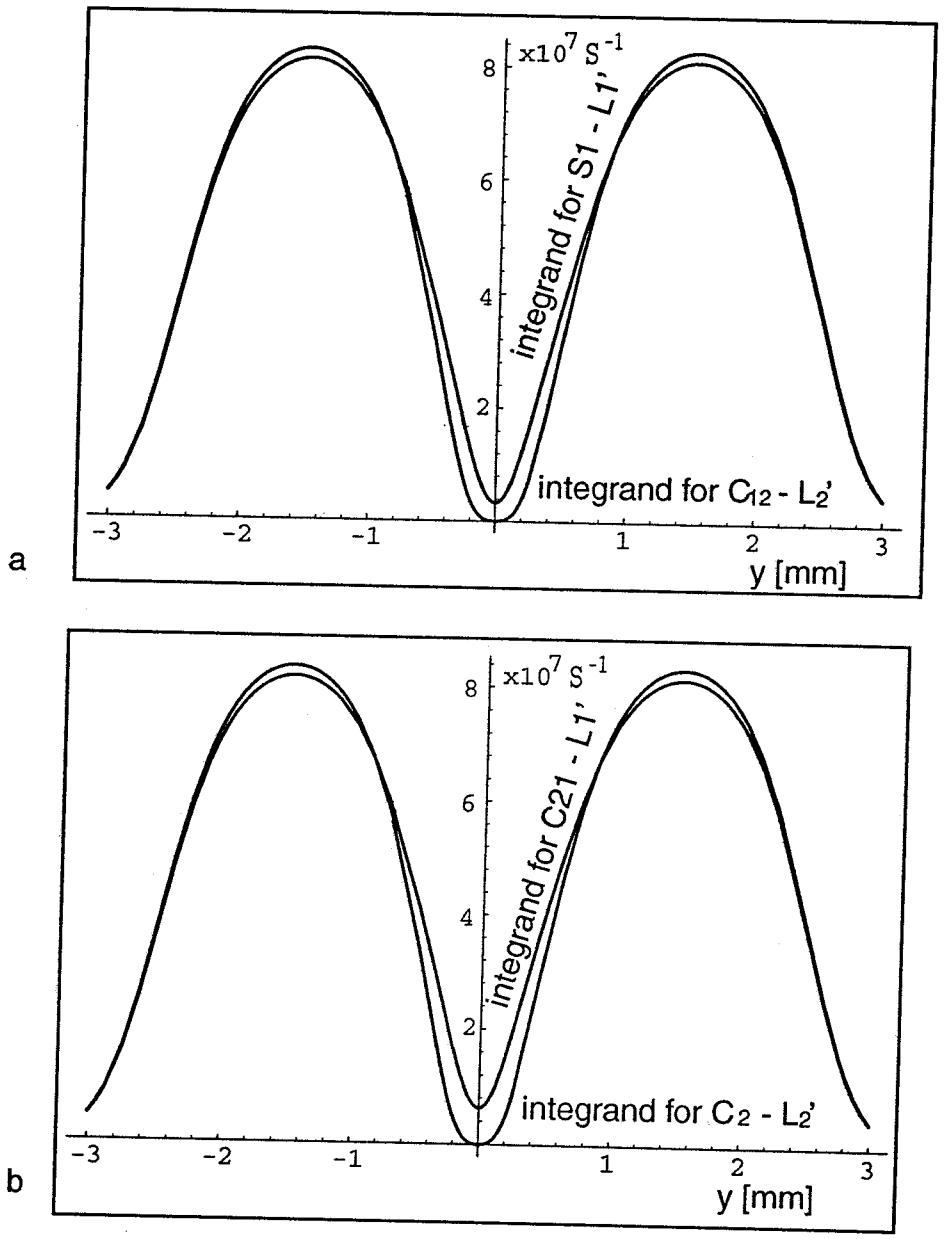

Figure 3. Integrand comparison for $\beta = 1.2 \times 10^8$, yielding stable in-phase coupled mode and unstable out-of-phase coupled mode. The larger areas for $S_1 - L'_1$ in (a) and $C_{21} - L'_1$ in (b) are due to contributions from gain in the center region.

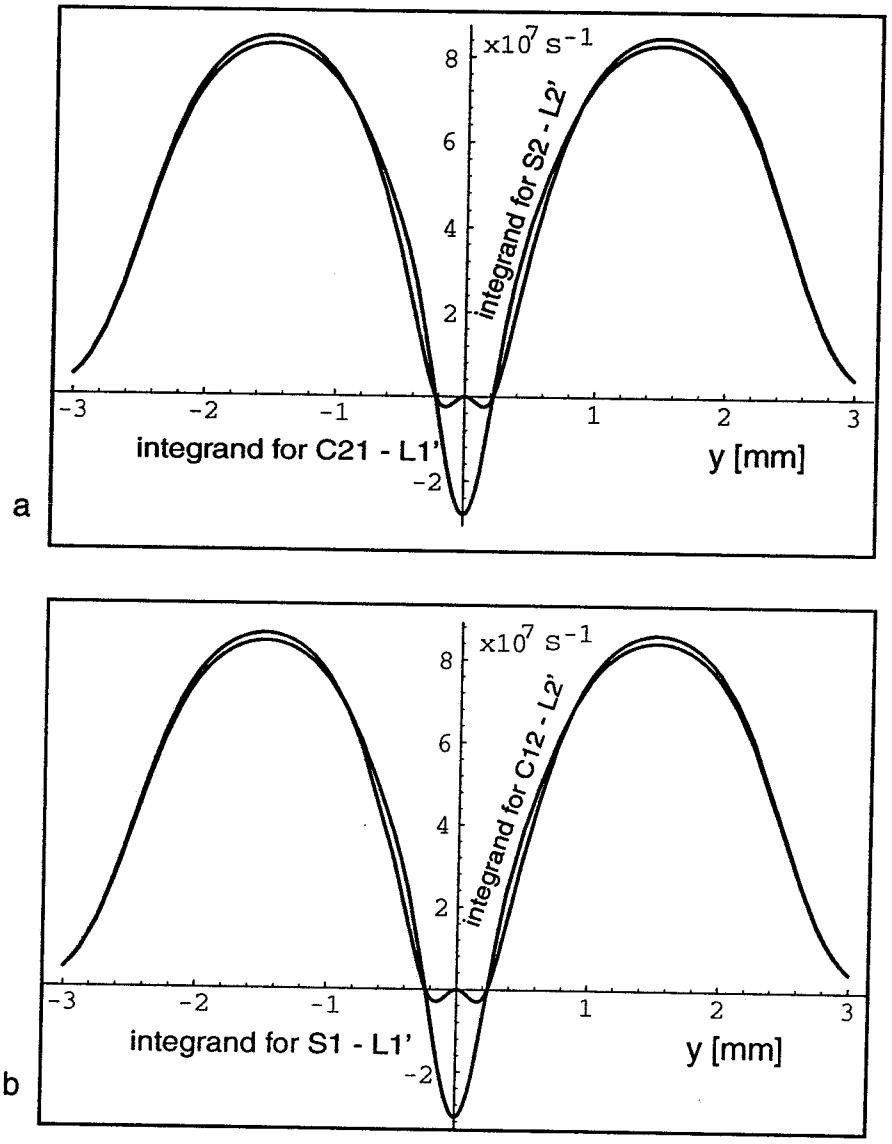

Figure 4. Integrand comparison for $\beta = 4.45 \times 10^8$, yielding stable out-of-phase coupled mode and unstable in-phase coupled mode. The larger areas for $S_2 - L'_2$ in (a) and $C_{12} - L'_2$ in (b) are due to contributions from gain in the center region.

The result in Table 1 clearly indicates that for the smaller loss ($\beta = 1.2\times10^8$) in the center, the in-phase coupled mode (with subscript 1) is stable and the out-of-phase coupled mode (with subscript 2) is unstable; and for the larger loss in the center ($\beta = 4.45\times10^8$), the out-of-phase coupled mode is stable and the in-phase coupled mode is unstable. Figures 3 and 4 are plots of the integrands for the two β values, showing that the difference in areas comes mainly from the center region where the loss varies most rapidly.

We can obtain the mode stability readily by a simple graphic method. From (37), S_1 and C_{12} are functions of f; and S_2 and C_{21} are functions of g. We plot these functions in Figure 5. These curves, combined with the horizontal lines representing the total modal losses, show the range of stability for both (f,0) and (0,g) states. In Figure 5a, the intersection A of L_1 and S_1 fixes the value of intracavity intensity f, which is 144 [w/mm^2]. This f value in turn determines C_{12} at point B. L_2 is always less than L_1 because there is less overlap of the out-of-phase mode with the central lossy region. Thus if L_2 lies between A and B, then $C_{12} < L_2$, and according to (38c), the in-phase mode will be stable. This same L_2 line also crosses the S_2 curve at point C, setting g = 140 [w/mm^2] for the out-of-phase coupled mode. This g value in turn yields C_{21} at point D, which satisfies $C_{21} > L_1$, and according to (38c), (0,g) state is unstable. Figure 5b shows a different case, where L_1 and L_2 are farther apart, corresponding to a larger β value. Here, the L_2 line is below point B, and the C_{12} value at B is larger than L_2. Thus the in-phase coupled mode is unstable. The same L_2 line crosses S_2 at point C, which also determines g. The C_{21} value for this g is given by intersection D, lying below the L_1 line. Thus the out-of-phase coupled mode is stable. The various values at the intersections on Figure 5a and 5b are the same as listed in Table 1.

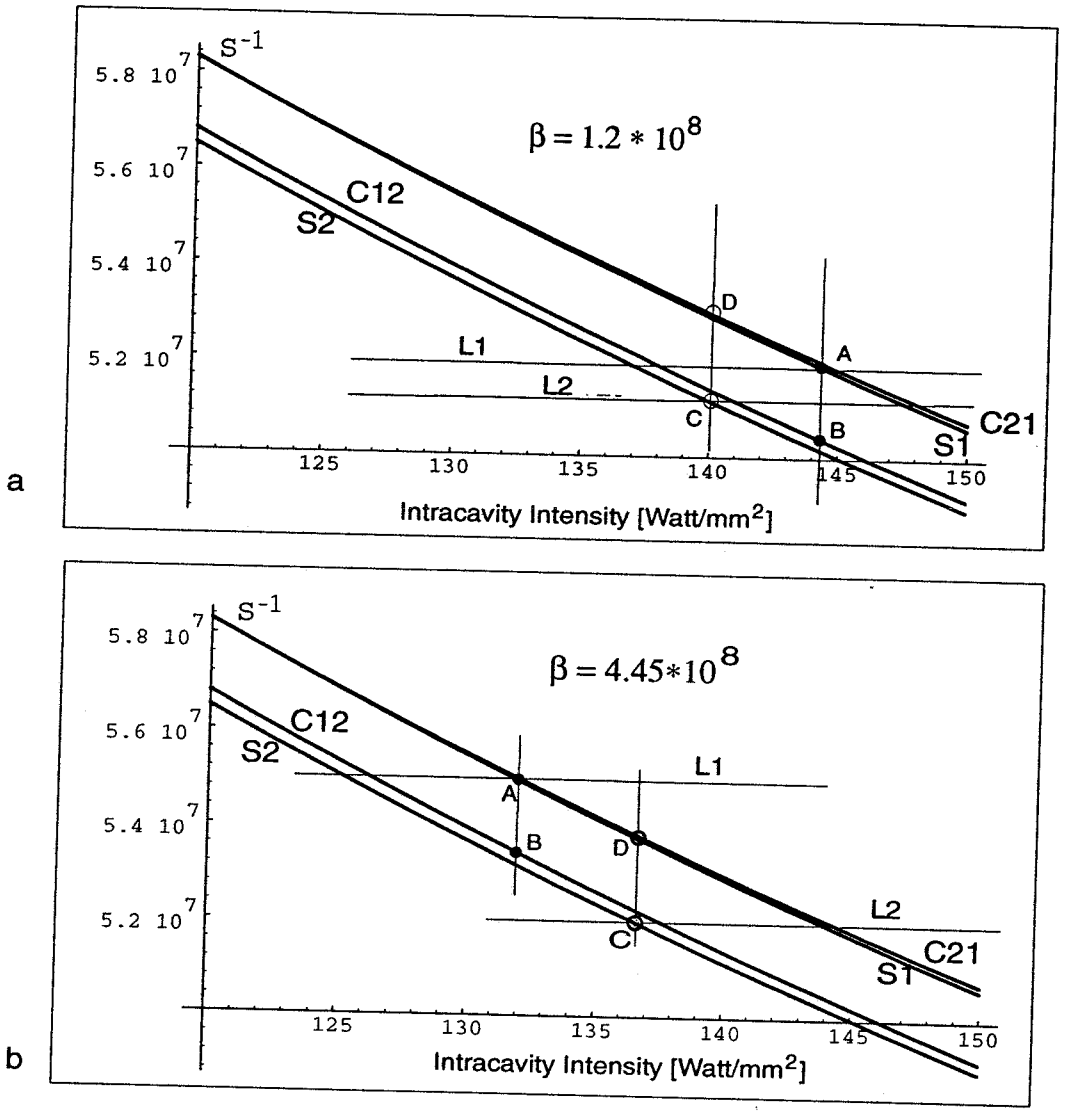

Figure 5. The stability diagrams. S_1, C_{12}, S_2 and C_{21} are plotted as functions of intensity. Intersection A of S_1 and L_1 determines the in-phase mode intensity. The position of the L_2 line lying above or below point B determines whether the in-phase mode is stable or not. Intersection C of S_2 and L_2 determines the out-of-phase mode intensity. The position of the L_1 line above or below point D determines whether the out-of-phase coupled mode is stable or unstable. Thus (a) represents a situation with a stable in-phase mode and an unstable out-of-phase mode, (b) *vice versa* and in (c) both modes are unstable.

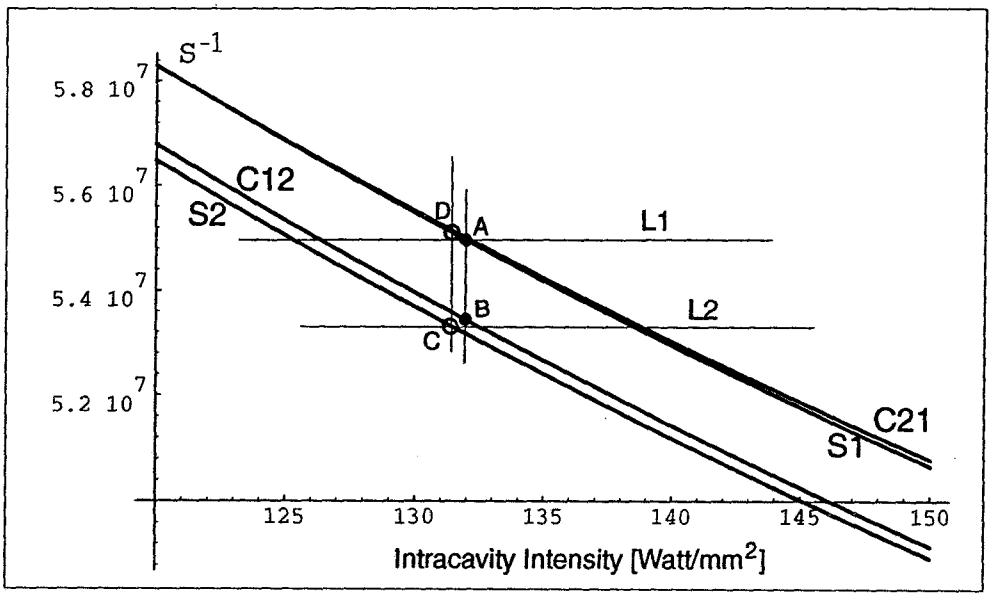

Figure 5c

This stability diagram reveals yet another possibility, i.e., a situation where neither mode is stable. In Figure 5c, the L_2 line is just slightly bellow point B so intersection C is to the left of B, and the intersection D is slighly higher than the L_1 line. Thus we have $C_{12} > L_2$ and $C_{21} > L_1$ and both modes are unstable. In our experiments we have observed the laser switching continuously between the two modes, not stable in either one. This may correspond to the situation described in Figure 5c.

In the above we used a constant small-signal gain that corresponds to a uniform excitation, and a loss in equation (40) that corresponds to a non-uniform and non-saturable loss in the laser array. It is also possible, even likely, that the excitation is actually not uniform, e.g., there is a smaller gain (or even no gain) in the central coupling region compared to the lasing channels. To reflect this situation, we made calculations with a saturable loss in the central region, with a

small signal gain:

$$\gamma_0(y) = \gamma'_0 - \beta \exp(-20y^2) \quad , \tag{41}$$

and $\sigma'(y)$ is taken as zero. The results for two different values of β showed the same qualitative trend as for the unsaturated loss case, i.e., for larger (smaller) β values within a certain range, the out-of-phase (in-phase) coupled mode is stable and the in-phase (out-of-phase) coupled mode unstable.

Another interesting observation to be made from these numerical calculations is that only about ten percent of the laser volume is involved to achieve the mode switching: for a total width of the intensity distribution of 5 mm (-2.5 to 2.5), the dimension over which the loss varies is only less than 0.5 mm. In our experiments with CO_2 lasers, we have no convenient way of changing the local gain or loss electronically. But if our calculations are applicable to semiconductor lasers, where there are ways of changing the local injection current, it should be possible to change the oscillation mode electronically. The small volume involved implies a small capacitance and hence a high switching speed. This might be useful in semiconductor optical logical devices.

§2.5 Numerical Examples of Two-dimensional Loss Distribution

We now proceed to apply the theory developed in the previous sections to a two-dimensional model, where the loss and the transverse distribution of the laser fields are functions of both x and y. It is our expectation that two-dimensional numerical calculations of the mode stability and mode competition will reveal more information on practical array structures. Two different wall-slot coupled gas laser array structures are treated, the transverse profiles of which are shown in Figure 6. One of them is the symmetric wall structure that is an approximation to the array reported by Bourdet et al.[9]; and the other, nonsymmetric wall structure, is an approximation to that reported by Newman et al[7]. Because gain and loss can be treated as the same parameter with different signs, we still assume gain to be a constant and assign all the spatial variation to the loss.

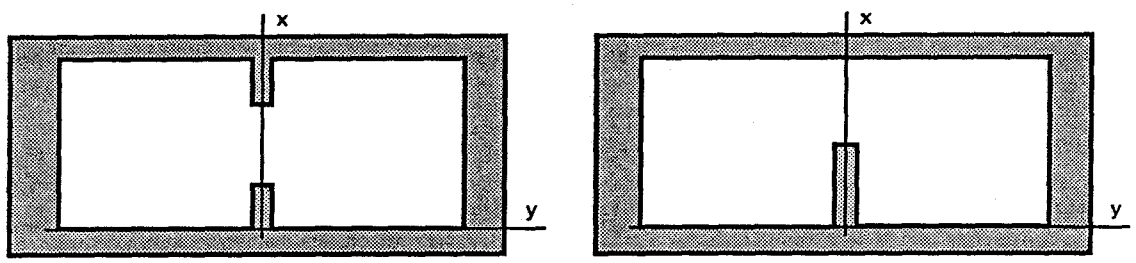

Figure 6 Illustration for the symmetric and non-symmetric array structures.

The laser modal fields for the in-phase and out-of-phase coupled modes are assumed to be approximated by the functions:

$$\left.\begin{aligned}\phi_1(x,y) &= c_1 \sin\left(\frac{\pi x}{2}\right)\left\{\exp[-(y-1.5)^2] + \exp[-(y+1.5)^2]\right\} \\ \phi_2(x,y) &= c_2 \sin\left(\frac{\pi x}{2}\right)\left\{\exp[-(y-1.5)^2] - \exp[-(y+1.5)^2]\right\}\end{aligned}\right\} \qquad (42)$$

respectively, where $c_1 = 2.177$ and $c_2 = 2.202$ are normalization constants. They are shown in Figure 7.

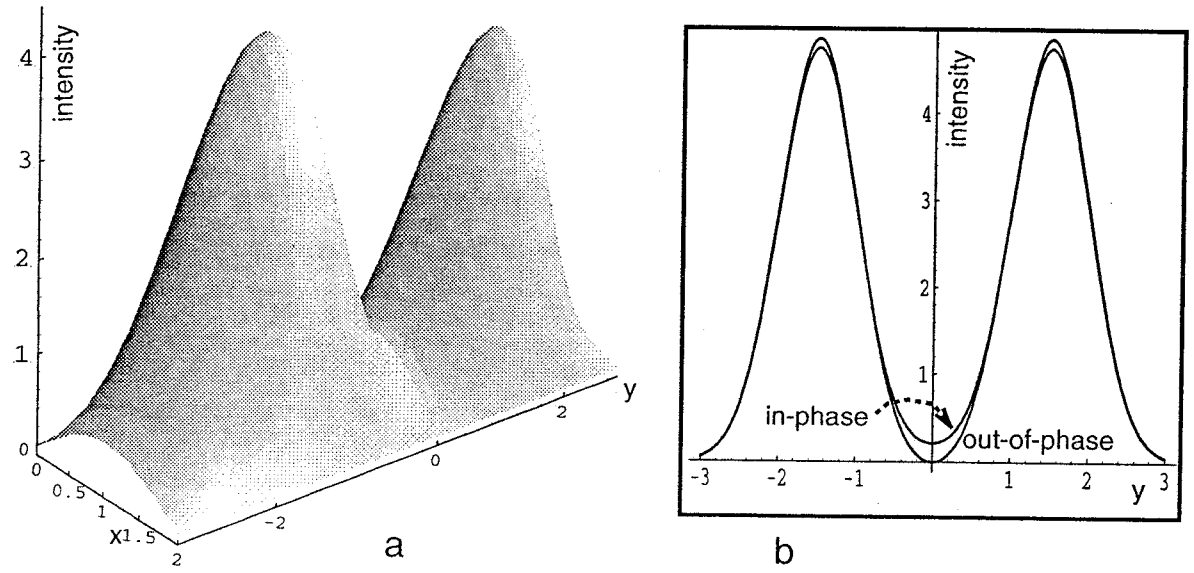

Figure 7. a) The 3-D intensity distribution for the in-phase coupled mode; b) center cross section of both in-phase and out-of-phase coupled modes.

We will calculate the stability for both coupled modes for the two structures with the same array dimension, 2 mm × 6 mm, and same slot width, 1 mm.

The loss function for the symmetric wall array can be expressed as:

$$\frac{\sigma'(x,y)}{2\epsilon} = \begin{cases} \beta\exp(-\alpha y^2), & 0 < x < 0.5, \quad 1.5 < x < 2 \\ 0, & 0.5 < x < 1.5 \end{cases} \tag{43a}$$

and for the single wall array:

$$\frac{\sigma'(x,y)}{2\epsilon} = \begin{cases} \beta\exp(-\alpha y^2), & 0 < x < 1 \\ 0, & 1 < x < 2 \end{cases} \tag{43b}$$

These two loss functions are shown graphically in Figure 8.

The localized modal loss as defined in equation (28b) becomes:

$$L_j = \frac{1}{2\epsilon S}\int_S \sigma'(x,y)\phi_j^2(x,y)\, dxdy \tag{44}$$

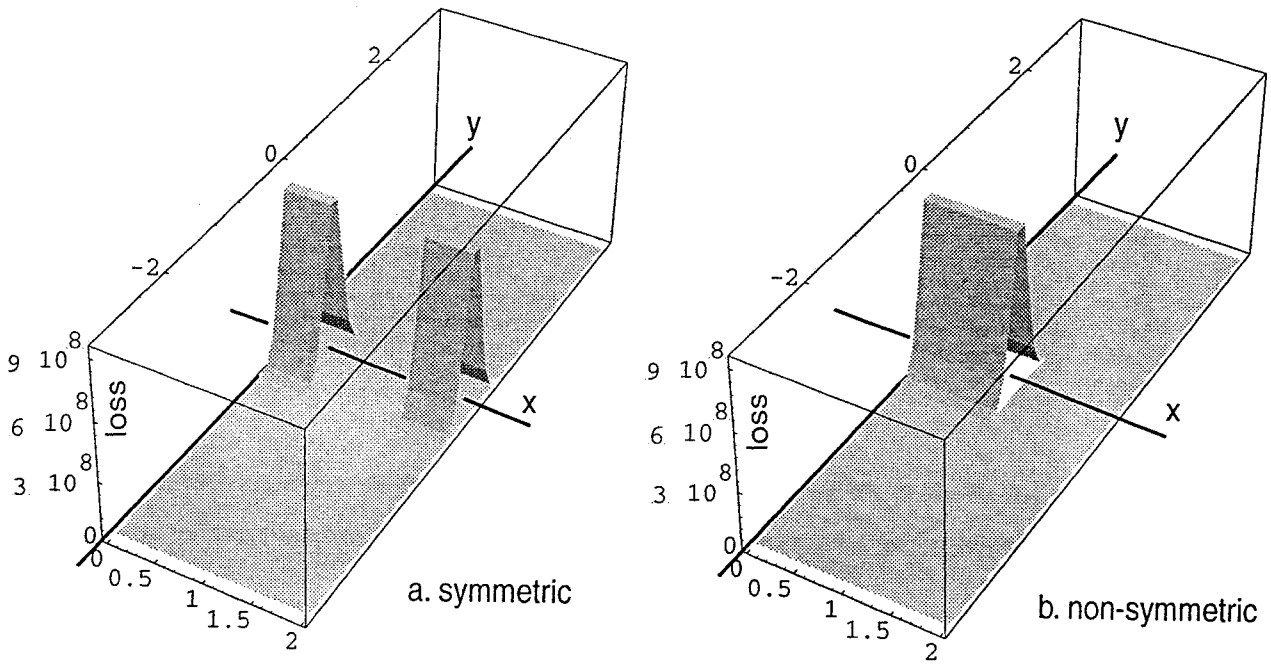

Figure 8. Spatial loss distributions for both the symmetric and the non-symmetric structures.

Substituting $\sigma'(x,y)/2\epsilon$ in (44) with (43a) and (43b), we obtain the spatially-dependent part of the modal loss for the two structures. In each structure we can

determine the stability of both the in-phase and out-of-phase coupled modes via the graphical method introduced in Section 4. The fixed modal loss that originated from the mirror absorption, transmission, etc., for both structures are assumed to be the same as in Section 4, $L_0 = 5.1 \times 10^7$. Thus for a β value of 8.9×10^8, twice as the high β value in Section 4, where the one-dimensional loss distribution should be the spatial average of the loss here, we obtain a stable (unstable) in-phase coupled mode and an unstable (stable) out-of-phase coupled mode in the symmetric (nonsymmetric) structure. These are depicted with the stability diagram of Figure 9. Such numerical results are reasonable because in the symmetric array structure, the lossy wall overlaps with the tail of the sine distribution of the intensity, while in the nonsymmetric structure, the wall overlaps partially with the peak of the intensity distribution, introducing more modal loss. We believe the above numerical results provides an explanation to the difference between the symmetric array structure that was reported in Reference 9 where in-phase coupling was obtained in arrays with five channels, and the nonsymmetric structure that was reported in Reference 7, where the out-of-phase coupled mode is dominant in the array.

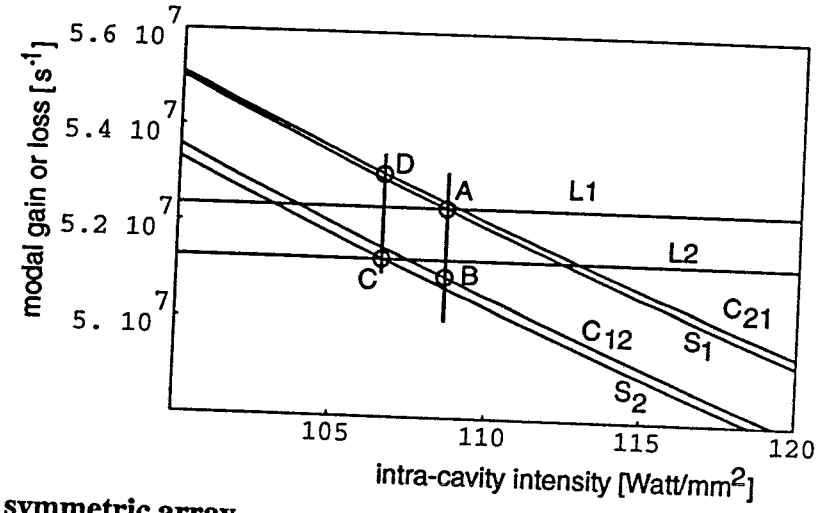

a. symmetric array

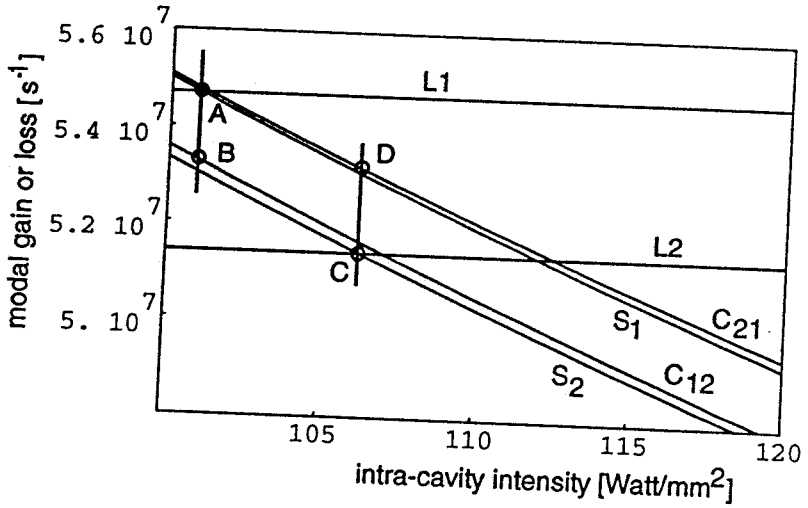

b. non-symmetric array

Figure 9. Stability diagrams for both the symmetric and the non-symmtric structures.

§2.6 Stability of Two-Mode Oscillation

From Section 3, we know that in a two element array, one of the steady state solutions for the differential equation is (p_1,p_2), which represents two modes oscillating simultaneously. Here we will investigate the stability of this solution. Under perturbations, this state will become $(p_1+\delta_1,\ p_2+\delta_2)$. From equation (25) in Section 2 and Appendix A, the differential equation are, for j=1, 2:

$$\dot{\delta}_j = 2\left[\frac{c}{2nS}\int_S \frac{\gamma_0(x,y)\ |\phi_j(x,y)|^2\ dxdy}{1+\dfrac{(p_1+\delta_1)|\phi_1(x,y)|^2+(p_2+\delta_2)|\phi_2(x,y)|^2}{I_s}} - L_j\right](p_j+\delta_j). \qquad (45)$$

Because the perturbations are small, we can ignore terms of second order or higher in δ_1 and δ_2. Using the binomial expansion, we obtain:

$$\dot{\delta}_j \simeq 2\left\{\frac{c}{2nS}\int_S \frac{\gamma_0(x,y)\ |\phi_j(x,y)|^2\ dxdy}{1+\dfrac{p_1|\phi_1|^2+p_2|\phi_2|^2}{I_s}}\left[1-\frac{\delta_1|\phi_1|^2+\delta_2|\phi_2|^2}{I_s\left(1+\dfrac{p_1|\phi_1|^2+p_2|\phi_2|^2}{I_s}\right)}\right] - L_j\right\}(p_j+\delta_j)\ . \qquad (46)$$

Because $(p_1,\ p_2)$ is assumed to be a steady state solution, we must have the saturated gain equal to the total loss for both $j = 1,\ 2$:

$$\frac{c}{2nS}\int_S \frac{\gamma_0(x,y)\ |\phi_j(x,y)|^2\ dxdy}{1+\dfrac{p_1|\phi_1(x,y)|^2+p_2|\phi_2(x,y)|^2}{I_s}} - L_j = 0. \qquad (47)$$

Then (46) becomes:

$$\dot{\delta}_j \simeq -\frac{cp_j}{nI_sS}\int_S \frac{\gamma_0(x,y)\ |\phi_j(x,y)|^2(\delta_1|\phi_1|^2+\delta_2|\phi_2|^2)\ dxdy}{\left(1+\dfrac{p_1|\phi_1|^2+p_2|\phi_2|^2}{I_s}\right)^2},\ j=1,\ 2\ . \qquad (48)$$

This equation can be written in a matrix form exactly as equation (34):

$$\dot{\delta} \equiv \begin{pmatrix} \dot{\delta}_1 \\ \dot{\delta}_2 \end{pmatrix} = \begin{pmatrix} A & B \\ C & D \end{pmatrix} \begin{pmatrix} \delta_1 \\ \delta_2 \end{pmatrix}. \tag{49}$$

We make the following definition for the integrals in (48):

$$a \equiv -\frac{c}{nI_s S}\int_S \frac{\gamma_0(x,y)\ |\phi_1|^4\ dxdy}{\left(1+\frac{p_1|\phi_1|^2+p_2|\phi_2|^2}{I_s}\right)^2}; \quad b \equiv -\frac{c}{nI_s S}\int_S \frac{\gamma_0(x,y)|\phi_1|^2|\phi_2|^2\ dxdy}{\left(1+\frac{p_1|\phi_1|^2+p_2|\phi_2|^2}{I_s}\right)^2};$$

$$d \equiv -\frac{c}{nI_s S}\int_S \frac{\gamma_0(x,y)\ |\phi_2|^4\ dxdy}{\left(1+\frac{p_1|\phi_1|^2+p_2|\phi_2|^2}{I_s}\right)^2}. \tag{50}$$

From (48) we can see:

$$A = p_1 a, \quad B = p_1 b, \quad C = p_2 b, \quad D = p_2 d\ . \tag{51}$$

The eigenvalues for the operating matrix in (49) are:

$$\lambda_{1,2} = \frac{1}{2}\left[A+D \pm \sqrt{(A+D)^2 - 4(AD-BC)}\right]$$

$$= \frac{1}{2}\left[A+D \pm \sqrt{(A+D)^2 - 4p_1p_2(ad-b^2)}\right]. \tag{52}$$

The Schwarz inequality tells us for two arbitrary real functions $f_1(x,y)$ and $f_2(x,y)$:

$$\left[\int f_1(x,y)f_2(x,y)dxdy\right]^2 \le \int {f_1}^2(x,y)dxdy \int {f_2}^2(x,y)dxdy\ , \tag{53}$$

in which the equality sign holds only when $f_1 = f_2$. Applying this to a, d, and b, as defined in (50), we obtain:

$$ad > b^2 . \tag{54}$$

It follows from this that both eigenvalues λ_1 and λ_2 take the sign of $A + D$, which is negative. Thus the two-mode steady state is always stable.

In most laser applications, multiple transverse mode operation is undesirable. And now there is only one way left to avoid it: Make equation (47) invalid. This can be realized by increasing the modal discrimination.

APPENDIX A

Saturated Population Inversion under Multi-mode Operation

Multi-mode laser oscillation has been treated by Sargent, Scully and Lamb[9], to whom we owe a great deal for their insight. However, their study was based on a small-signal approximation, which is not the case in our situation. We build our treatment from Yariv[5] and expand it to multi-mode cases with some assumptions and approximations.

Equations (17), (22), (23) and (25) are coupled mode equations. Mode coupling occurs in form of saturation of the population inversion saturation, hence the susceptibility $\chi(\mathbf{r},\omega)$, and is carried through to the modal susceptibility χ_j. The imaginary part χ'' is proportional to the difference of the diagonal density matrix elements $(\rho_{11}-\rho_{22})$ which represents the population difference between the upper and lower laser levels[5], and the differential equations for the density matrix elements are:

$$\left.\begin{aligned} \frac{d}{dt}\rho_{21} &= -i\omega_0\rho_{21} + i\frac{\mu}{\hbar}E(t)(\rho_{11}-\rho_{22}) - \frac{\rho_{21}}{T_2} \qquad \text{(A.1a)} \\ \frac{d}{dt}(\rho_{11}-\rho_{22}) &= i2\frac{\mu}{\hbar}E(t)(\rho_{21}-\rho^*{}_{21}) - \frac{(\rho_{11}-\rho_{22})-(\rho_{11}-\rho_{22})_0}{\tau} \qquad \text{(A.1b)} \end{aligned}\right\} .$$

We assume a single longitudinal mode with N transverse modes. The frequency differences among these modes are assumed to be very small compared to the line width. Using the expansion in (2) and (13) for the linearly polarized total electric field,

$$E(\mathbf{r},t) = \sum_j^N e_j(t)\,\phi_j(\mathbf{r}) = \sum_j^N \left[\frac{1}{2}\,e_{j0}(t)\,e^{-i\omega_j t} + c.c.\right]\phi_j(\mathbf{r}) \,. \qquad \text{(A.2)}$$

For convinience, we write the off-diagonal density matrix element ρ_{21} as follows:

$$\rho_{21}(t) \equiv \sigma_{21}(t)e^{-i\omega_a t}, \qquad \omega_a \equiv \frac{\sum_j^N \omega_j}{N}. \tag{A.3}$$

Thus from (A.1a) we have the differential equation for σ_{21}:

$$\dot{\sigma}_{21} = i(\omega_a - \omega_0)\sigma_{21} + i\frac{\mu}{2\hbar}(\rho_{11} - \rho_{22})\sum_j^N e_{j0}(t)\ \phi_j e^{i\Delta_{aj}t} - \frac{\sigma_{21}}{T_2}, \tag{A.4}$$

where Δ_{aj} is the frequency difference: $\Delta_{aj} \equiv \omega_a - \omega_j$. High-frequency terms in (A.4) are ignored, because their contributions to the integration average to zero over the time scale of change for σ_{21}. Multiplying both sides of (A.4) with the factor $\exp\{[i(\omega_a - \omega_j) + \frac{1}{T_2}]t\}$ and performing some manipulations, (A.4) becomes:

$$\frac{d}{dt}\left[\sigma_{21}e^{[i(\omega_0 - \omega_a)+\frac{1}{T_2}]t}\right] = i\frac{\mu}{2\hbar}(\rho_{11} - \rho_{22})\sum_j^N e_{j0}\ \phi_j e^{[i(\omega_0 - \omega_a)+\frac{1}{T_2}]t}. \tag{A.5}$$

Assuming the rates of change for $(\rho_{11} - \rho_{22})$ and e_{j0} are much lower than $1/T_2$, we can pull them out of the integration. Then we obtain by integrating (A.5):

$$\sigma_{21} = i\frac{\mu}{2\hbar}(\rho_{11} - \rho_{22})\sum_j^N e_{j0}\ \phi_j e^{i\Delta_{aj}t}\ D(T_2, \omega_0 - \omega_j), \tag{A.6}$$

where $D(T_2, \omega_0 - \omega_j)$ is defined as:

$$D(T_2, \omega_0 - \omega_j) \equiv \frac{1}{\frac{1}{T_2} + i(\omega_a - \omega_j)}. \tag{A.7}$$

The $(\rho_{21} - \rho^*{}_{21})$ term in (A.1b) becomes:

$$(\rho_{21} - \rho^*{}_{21}) = \sigma_{21} e^{-i\omega_a t} - \sigma^*{}_{21} e^{i\omega_a t}$$

$$= i\frac{\mu}{2\hbar}(\rho_{11} - \rho_{22}) \left(\sum_j^N e_{j0}\, \phi_j e^{i\omega_j t}\, D(T_2,\, \omega_0 - \omega_j) + \text{c.c.} \right). \qquad \text{(A.8)}$$

Thus we have:

$$\frac{d}{dt}(\rho_{11} - \rho_{22}) = i2\frac{\mu}{\hbar} E(t)(\rho_{21} - \rho^*{}_{21}) - \frac{(\rho_{11} - \rho_{22}) - (\rho_{11} - \rho_{22})_0}{\tau}$$

$$= -\frac{1}{2}\left(\frac{\mu}{\hbar}\right)^2 (\rho_{11} - \rho_{22}) \left(\sum_j^N e_{j0}\, e^{-i\omega_j t}\, \phi_j + \text{c.c.} \right) \left[\sum_j^N e_{j0}\, e^{i\omega_j t} \phi_j D(T_2,\, \omega_0 - \omega_j) + \text{c.c.} \right]$$

$$- \frac{(\rho_{11} - \rho_{22}) - (\rho_{11} - \rho_{22})_0}{\tau}\,. \qquad \text{(A.9)}$$

If the frequency spread of the transverse modes is small compared to the line width, we can approximate $D(T_2,\, \omega_0 - \omega_j)$ with $D(T_2,\, \omega_0 - \omega_a)$. One can see from (A.9) that there are beatings in the population inversion, and it does not have a steady state solution under multimode oscillation. But we realize that the spatial relaxation in the longitudinal direction can neutralize this beating. So it is possible that the rate of change of $(\rho_{11} - \rho_{22})$ is much slower than $e^{i(\omega_j - \omega_k)t}$ for any $k \neq j$. Thus we need keep only the terms with no exponential time dependence on the right side of (A.9):

$$\frac{d}{dt}(\rho_{11} - \rho_{22}) = -\frac{1}{2}\left(\frac{\mu}{\hbar}\right)^2 (\rho_{11} - \rho_{22}) [D(T_2,\, \omega_0 - \omega_a) + \text{c.c.}] \sum_j^N e_{j0} e_{j0}{}^* |\phi_j|^2$$

$$-\frac{(\rho_{11}-\rho_{22})-(\rho_{11}-\rho_{22})_0}{\tau} \quad . \tag{A.10}$$

We follow the majority in the literature in making the definitions below: Normalized line shape function:

$$g(\omega)=\frac{2T_2}{1+T_2{}^2(\omega_0-\omega_a)^2}\,; \tag{A.11}$$

saturation intensity:

$$I_s \equiv cn\epsilon_0\frac{\hbar^2}{\mu^2\tau g(\omega)}=\frac{1}{\eta}\frac{\hbar^2}{\mu^2\tau g(\omega)}\,; \tag{A.12}$$

and the laser intensity:

$$I=\sum_j^N I_j \equiv \frac{1}{2\eta}\sum_j^N e_{j0}e_{j0}{}^*|\phi_j|^2 \quad . \tag{A.13}$$

By requiring the left side of (A.10) to be zero, we obtain the steady-state solution for $(\rho_{11}-\rho_{22})$:

$$(\rho_{11}-\rho_{22})=\frac{(\rho_{11}-\rho_{22})_0}{1+\dfrac{\frac{1}{2\eta}\sum_j^N e_{j0}e_{j0}{}^*|\phi_j|^2}{I_s}}=\frac{(\rho_{11}-\rho_{22})_0}{1+\frac{I}{I_s}} \quad . \tag{A.14}$$

From Yariv[5], we know the susceptibility satisfies the following:

$$\chi'' \propto \rho_{11}-\rho_{22}\,, \tag{A.15}$$

and

$$\chi'' = -\frac{n^2 c}{\omega}\gamma \,, \tag{A.16}$$

where γ is the gain coefficient of lasing medium in unit of meter^{-1}.

REFERENCES

1. L.J. Mawst, D. Botez, M. Jansen, T.J. Roth and J.J. Yang, "Highly Coherent In-Phase-Mode Operation of 20-Element Resonant Arrays of Antiguides," IEEE Photonics Tech. Lett., Vol. 2, No. 4, pp. 249-252, April 1990.

2. Y. Zhang and W.B. Bridges, "Stable In-phase Locked Array of CO_2 Waveguide Lasers," THJ5, Optical Society of America 1991 Annual Meeting, November 3-8, 1991, San Jose, California.

3. C.L. Tang, A. Schremer and T. Fujita, "Bistability in Two-mode Semiconductor Lasers via Gain Saturation," Appl. Phys. Lett. **51** (18), November 2, 1987.

4. D.F.G. Gallagher, "Gain-coupled Optical Logic in Semiconductor Lasers, Applied Optics," Vol. 29, No. 29, pp. 4359-4371, October 10, 1990.

5. M. Sargent III, M.O. Scully and W.E. Lamb, Jr., Laser Physics, Addison-Wesley, 1974.

6. A. Yariv, Quantum Electronics, 3rd Edition, John Wiley & Sons, 1989.

7. L.A. Newman, A.J. Cantor, R.A. Hart, J.T. Kennedy and A.J. DeMaria, "Coupled High Power Waveguide Laser Research," Final Report on Contract F49620-84-C-0062, July 30, 1985.

8. R.L. Abrams and W.B. Bridges, "Characteristics of Sealed-Off Waveguide CO_2 Lasers," IEEE J. Quantum Electronics, Vol. QE-9, pp. 940-946, September 1973.

9. G.L. Bourdet, G.M. Mullot and J.Y. Vint, "Linear Array of Self-Focusing CO_2 Waveguide Lasers," IEEE J. Quantum Electronics, Vol. 26, No. 4, pp. 701-710, April 1990.

CHAPTER 3. EXPERIMENTAL STUDIES OF CO_2 LASER ARRAYS OF HOLLOW BORE WAVEGUIDES

§3.1 Introduction

There had been several reports of phase-coupled CO_2 laser arrays before the beginning of our project. The first was by Youmans[1] and Schlossberg[2] (Figure 1a), where the waveguides are separated by walls of an IR transparent material, for example, ZnSe, through which the wave in one element leaks to the neighboring elements. Although it proved the concept of phase coupling in CO_2 laser arrays, this structure has the disadvantage that the optical quality of the expensive ZnSe material could deteriorate when exposed to the ion bombardment in the gas discharge. It was not a practical structure.

Another way of achieving mode coupling in a linear array was reported by Colley et al.[3] (Figure 1b), where the length of the array is considerably less than that of the laser optical cavity, so that the wave exiting one of the elements can leak into other elements after it reflects off the cavity mirrors. This method tends to have a very weak coupling, and thus a small coupling range. In addition, the geometry of the individual waveguides must be controlled very accurately in order to achieve the coupling. The temperature gradient in the array is capable of producing enough frequency displacement to perturb the coupling in this structure.

DeMaria and Bridges suggested another CO_2 waveguide laser array structure[4] (Figure 1c), where the coupling is facilitated by a partial opening in the waveguide walls, through which the wave from one element can leak into the neighboring element. Because the coupling occurs within the laser active region, this type of coupling tends to be strong. This structure was successfully demonstrated by Newman et al.[5]

Bourdet et al.[6] (Figure 1d) reported yet another type of coupled array CO_2 laser. But we can categorize their structure as a variation from that of DeMaria and Bridges, in the sense that it also has open slots between lasing channels that allow coupling; the "slots" are just much larger.

We chose to start from the structure suggested by DeMaria and Bridges not only because professor Bridges is my thesis adviser, but also because we could obtain samples of waveguide array ceramics from researchers at United Technologies, with whom professor Bridges has been a collaborator working on the array lasers. All the array structures mentioned above are shown in Figure 1.

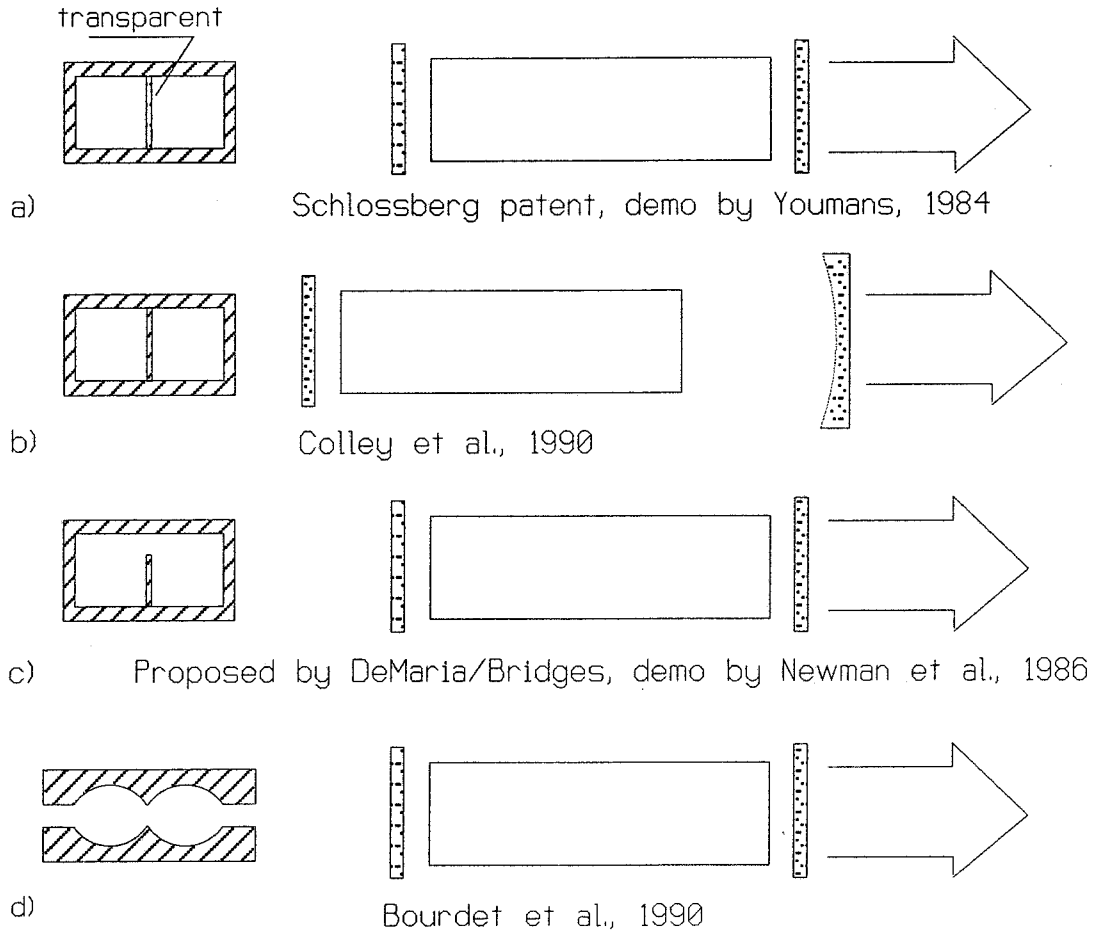

Figure 1. Various schemes for coupled CO_2 waveguide laser arrays.

§3.2 Modes of a Single-Bore Waveguide CO_2 Laser

Marcatili and Schmeltzer[7] were the first to suggest using hollow metallic or dielectric waveguides for lasers. They found that the attenuation for each of the hollow waveguide modes was proportional to the square of the free-space wavelength and inversely proportional to the cube of the diameter of the waveguide tube. Their modal analysis was applied to circular waveguide only, but all the important physical phenomena were described. Laakman and Steier[8] studied the modes of hollow rectangular dielectric waveguides (Figure 2) obtaining the same dependence of modal loss on wavelength and guide aperture, and derived the field components for $EH^x{}_{nm}$ modes as follows :

$$E_x = \sqrt{\frac{\mu}{\epsilon_0}}\, H_y =$$

$$= \left\{ \begin{array}{ll} \sin(\frac{m\pi x}{a})\sin(\frac{n\pi y}{b}), & \text{m, even; n, even,} \\ \cos(\frac{m\pi x}{a})\cos(\frac{n\pi y}{b}), & \text{m, odd; n, odd,} \\ \cos(\frac{m\pi x}{a})\sin(\frac{n\pi y}{b}), & \text{m, odd; n, even,} \\ \sin(\frac{m\pi x}{a})\cos(\frac{n\pi y}{b}), & \text{m, even; n, odd.} \end{array} \right\} \text{, inside material } \epsilon_0, \quad (3.1a)$$

and for $EH^y{}_{nm}$ modes as follows :

$$E_y = \sqrt{\frac{\mu}{\epsilon_0}}\, H_x =$$

$$= \left\{ \begin{array}{ll} \sin(\frac{m\pi x}{a})\sin(\frac{n\pi y}{b}), & \text{m, even; n, even,} \\ \cos(\frac{m\pi x}{a})\cos(\frac{n\pi y}{b}), & \text{m, odd; n, odd,} \\ \cos(\frac{m\pi x}{a})\sin(\frac{n\pi y}{b}), & \text{m, odd; n, even,} \\ \sin(\frac{m\pi x}{a})\cos(\frac{n\pi y}{b}), & \text{m, even; n, odd.} \end{array} \right\} \text{, inside material } \epsilon_0, \quad (3.1b)$$

and the fields vanish everywhere else. In (3.1) E_x and E_y represent x and y-direction polarized electric fields for two group of modes, respectively. Metal materials such as aluminum are not perfect conductors in the optical frequency range, so they need to be treated as lossy dielectric materials.

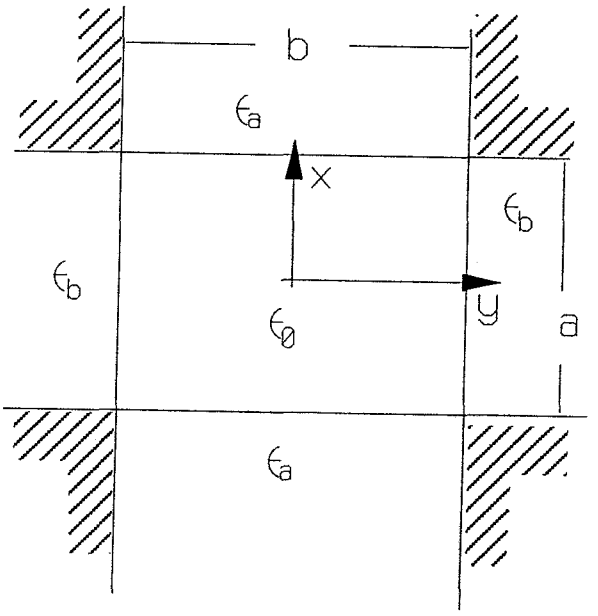

Figure 2. Hollow rectangular leaky waveguide studied by Laakman and Steier. The four corners are omitted to simplify the treatment.

For a "regular" or index-guided waveguide, where the core material has a higher dielectric constant than the surroundings, there is evanescent field in the surrounding material outside the waveguide region. This evanescent field can serve as means of coupling between several index-guided waveguides if they are parallel and placed in close proximity. A good example of this was given by Somekh et al.[9] However, if the dielectric constant of the core is lower than that of

the enclosure, this type of waveguide is termed an anti-waveguide or "leaky" waveguide, since the fields inside can "leak" through the boundary and radiate off to leak into infinity[10]. But if the wall material is also lossy, then the waves that "leak" out are also exponentially attenuated, and thus appear much like the evanescent waves in the regular index-guided waveguides. But the waveguide losses are finite for the "leaky" waveguide case. In fact, if the dielectric losses are very high, very little field exists in the wall material. Equations (3.1) assume that there is actually no field in the wall of our leaky waveguide, nor is there field outside it. Thus it is impossible to couple a group of hollow bore waveguide gas lasers by simply putting them in a closely spaced group. For these lasers, various methods of leaking waves from one element to another were shown in Figure 1.

§3.3 Arrays of Two-Bore Waveguide Lasers

At the outset of the project we elected to make a "test bed laser" in which the laser active region could be easily interchanged without disturbing the mirror alignment, so that different waveguide arrays could be checked one against the other easily without changing the other laser parameters. This test bed has allowed us to try new arrangements very quickly.

A photograph of the test bed laser is shown in Figure 3. The vacuum box for the test bed laser also serves as the optical bench for the laser cavity mirrors, and thus required more structural strength than it would just to withstand one atmosphere pressure. The inside dimensions to the box are $6'' \times 6'' \times 18''$ and the wall thickness is 3/4″. The box was fabricated of stainless steel by MDC Corp. The cross section of the electrode assembly inside the vacuum box is shown in Figure 4. Water-cooled aluminum anvils are used to hold the waveguide laser array, and keep it cool. The mirror adjustment micrometers installed is shown in Figure 3. The aluminum box on top houses the RF matching network.

The power source for the laser was in an oscillator-amplifier configuration at 146.505 MHz. The oscillator was a Kenwood TS-711 radio transceiver, continuously adjustable in power 0–25 Watt, and the amplifier was a Henry Radio 3002 vacuum-tube linear amplifier with a 1.5 kW maximum CW output. A Bird Thruline Model 43 power meter was used to monitor the input power and an Electro Impulse Laboratory TS-3499/URM power meter used to monitor the reflected power simultaneously. We built our own adjustable matching network to match the laser plasma impedance to the 50 Ω value desired by the linear amplifier. The electrode assembly including the waveguide array behaved as a capacitor, so a shunt inductance were added across it to resonate at 146 MHz. The circuit diagram for the power supply is drawn in Figure 5

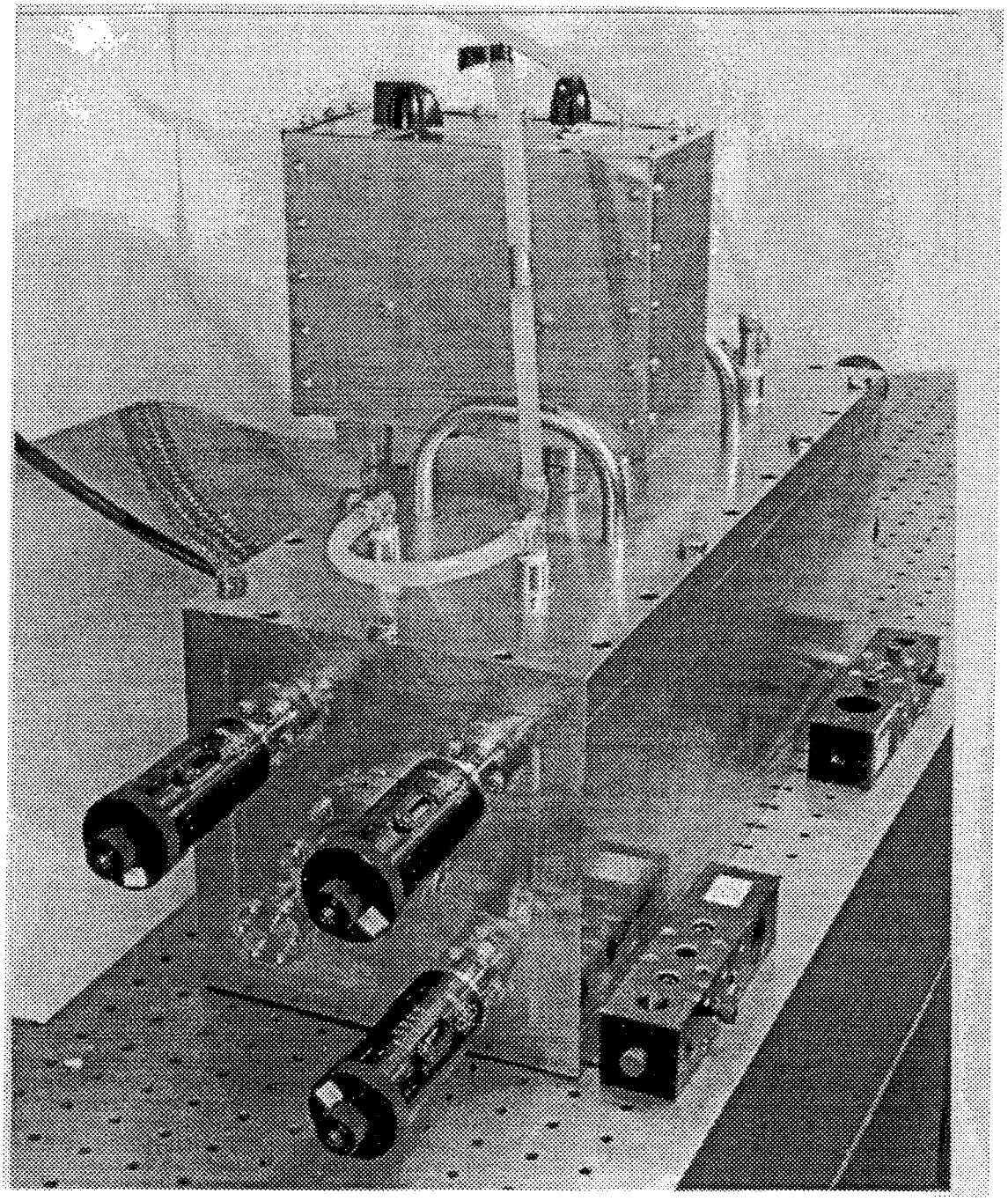

Figure 3. Photograph of the test bed laser. The aluminum box on top of the vacuum box contains the RF matching network.

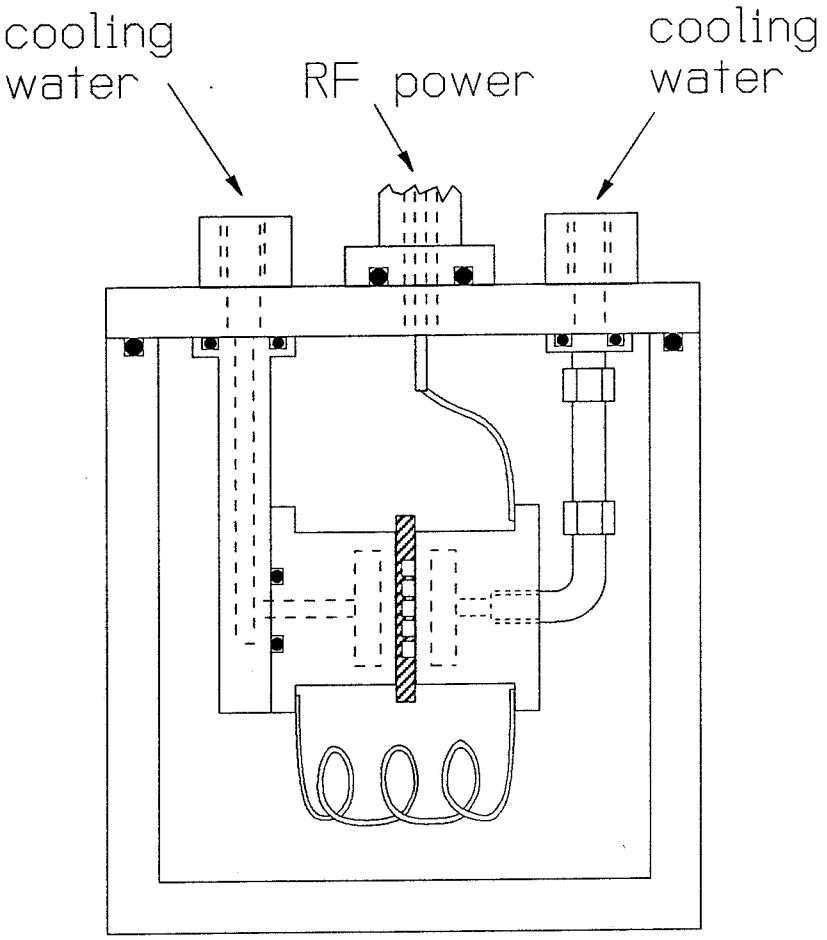

Figure 4. Cross section of the inside of the test bed laser

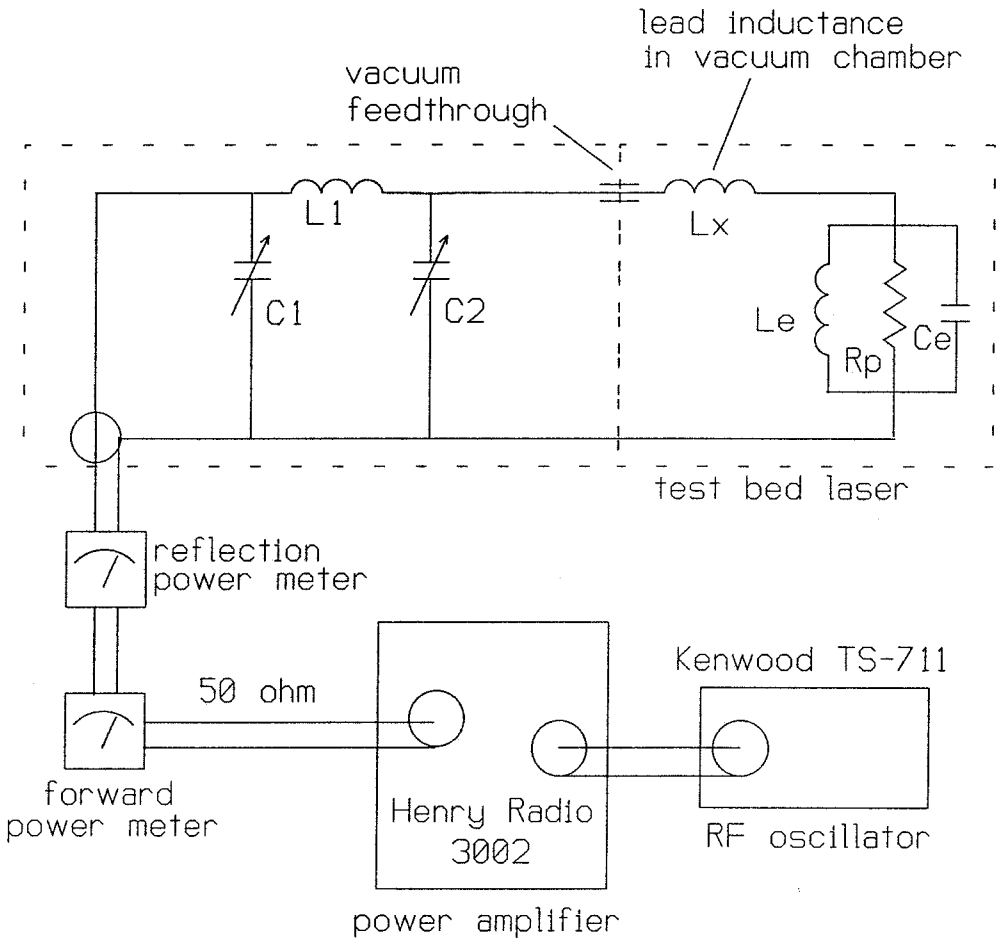

Figure 5. The 246.505 MHz driving circuit for the waveguide laser experiments.

The first array we tested was the type shown on Figure 6. Both coupled (Figure 6a) and uncoupled (Figure 6b) arrays were tested. The coupling is realized by the leakage across the opening in the walls. The gas mixture used was N_2:CO_2:He:Xe = 1:1:6:0.25. The output mirror transmission was 10%. The high reflectance mirror had 99.5% reflection. The highest laser power obtained from this coupled array was 41 watt at 432 watt of RF input and a gas pressure of 113 torr, for an efficiency of 9.4%. Figure 7 gives the laser output power as functions of the input RF power, with gas pressure as the parameter. The power was measured with a Coherent 201 power meter. The diagnostic setup for these measurements is shown in Figure 8. A diffraction grating was used to split the laser output into two beams. An Optical Engineering model 16-A spectrometer was used to monitor the rotational transition. A Boston Electronics model R004-0 fast HgCdTe photodetector was used with a Hewlett-Packard hp 8554B spectrum analyzer to detect beat notes; this detector has about a 1 nsec response time. The near-field spatial mode patterns were monitored with Optical Engineering quenched-fluorescence image plates inserted into the optical path and photographed with a 35mm camera. A pair of ZnSe lenses could be inserted ahead of the image plates to obtain the far field pattern as well. Total power was measured by inserting the Coherent 201 power meter into the laser output.

Figure 9 shows a typical behavior of the beat spectra and mode patterns for the coupled two-bore array. In these patterns the "0 Hz" is the large spike artifact at the left edge of the photograph, and the rightmost spike is leakage of the RF power source at 146.505 MHz, which served as a convenient frequency marker. The mode patterns in the upper right corner of each figure are corresponding far field intensity distributions. The beat spectra contained more than one component, indicating multimode operation for <u>each</u> bore. When the

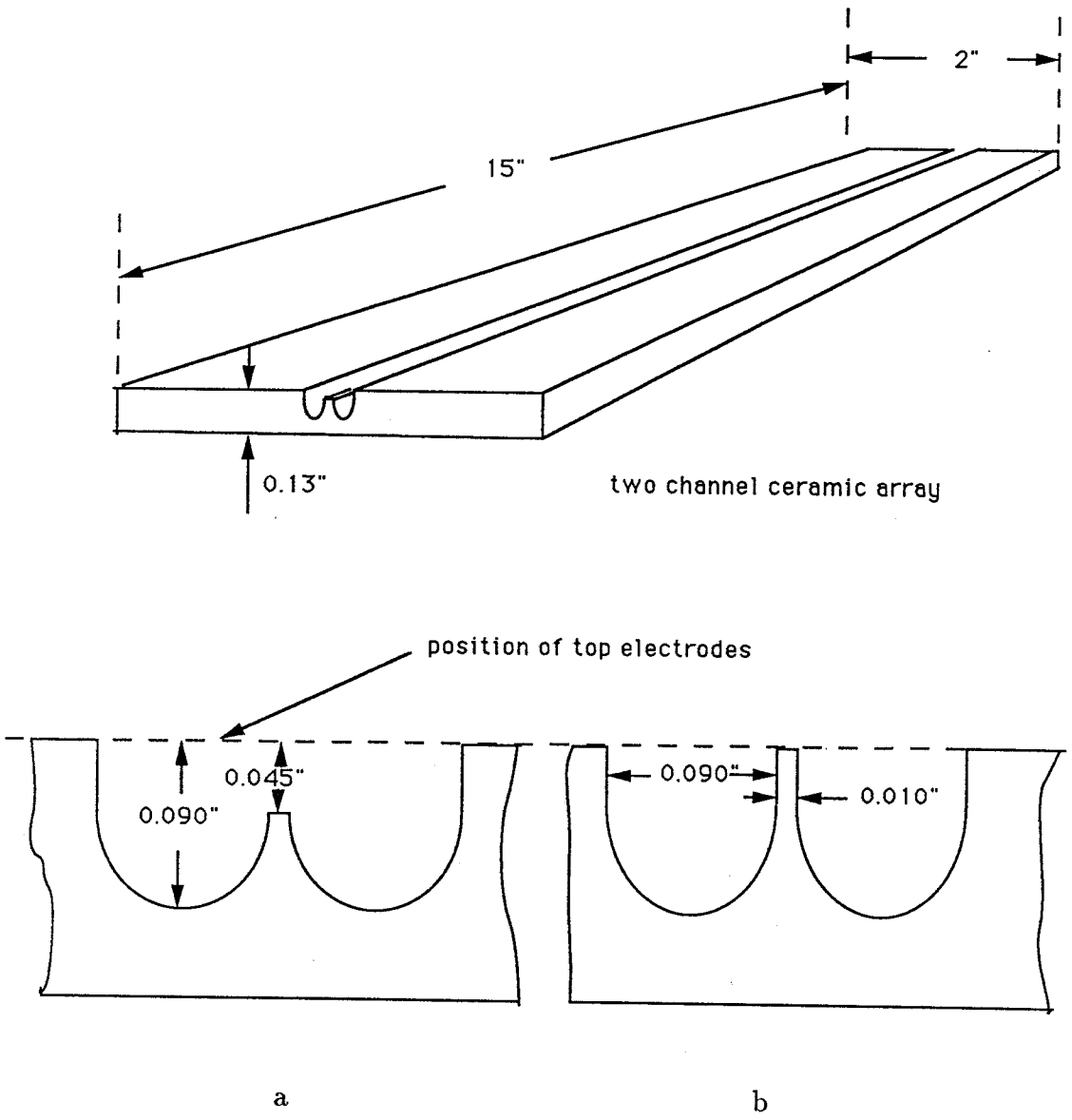

Figure 6. Sketch of UTRC ceramic two-channel waveguide showing dimensions. Details of the coupled and uncoupled arrays are shown in the blow-ups a) and b). They differ only by the gap. The material is high purity Al_2O_3, precision ground.

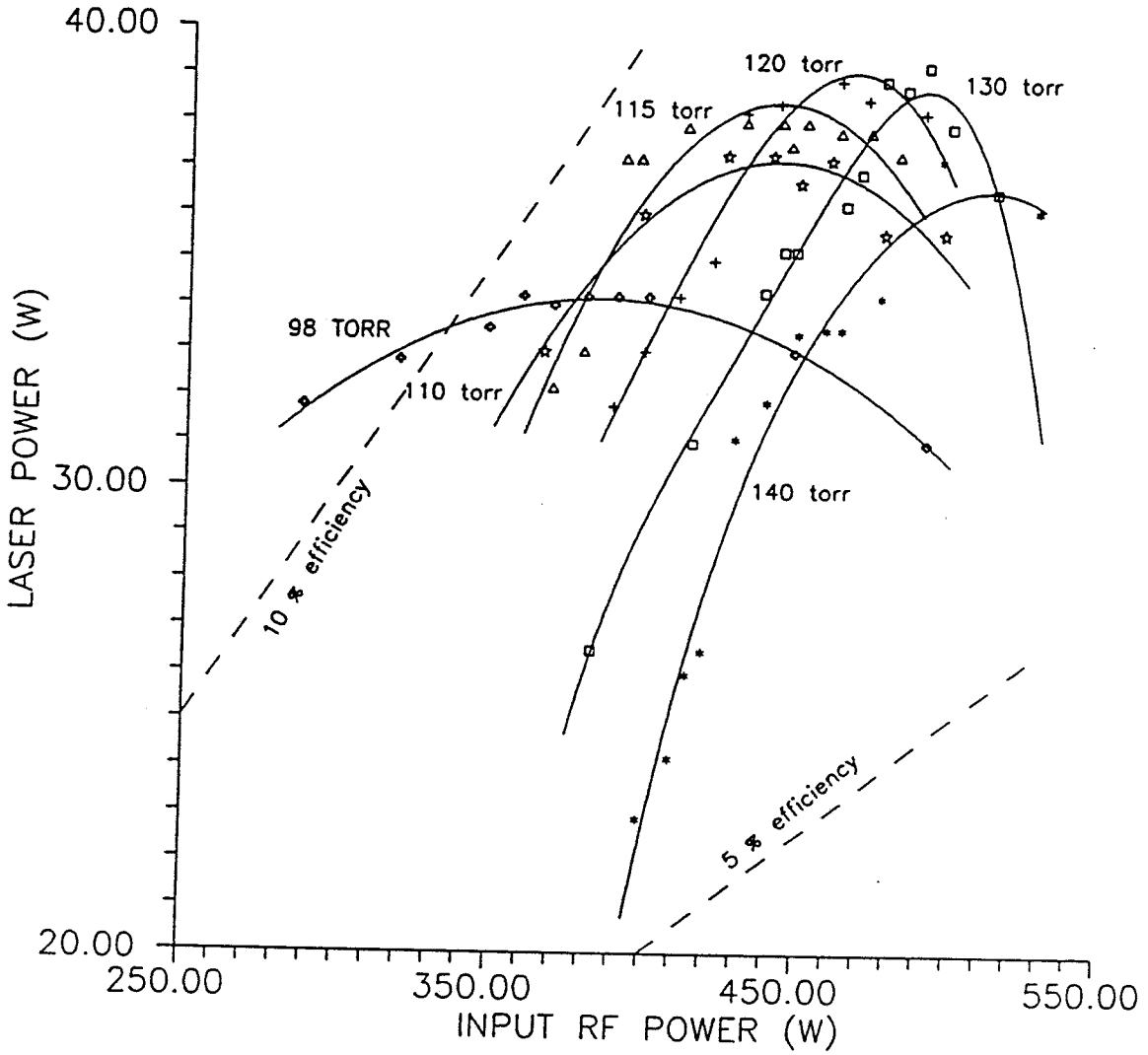

Figure 7. Measured laser power v.s. RF drive power at 146 MHz for the two-channel waveguide shown in Fig.6a with pressure as a parameter. Lines of constant efficiency are also shown at 5% and 10%.

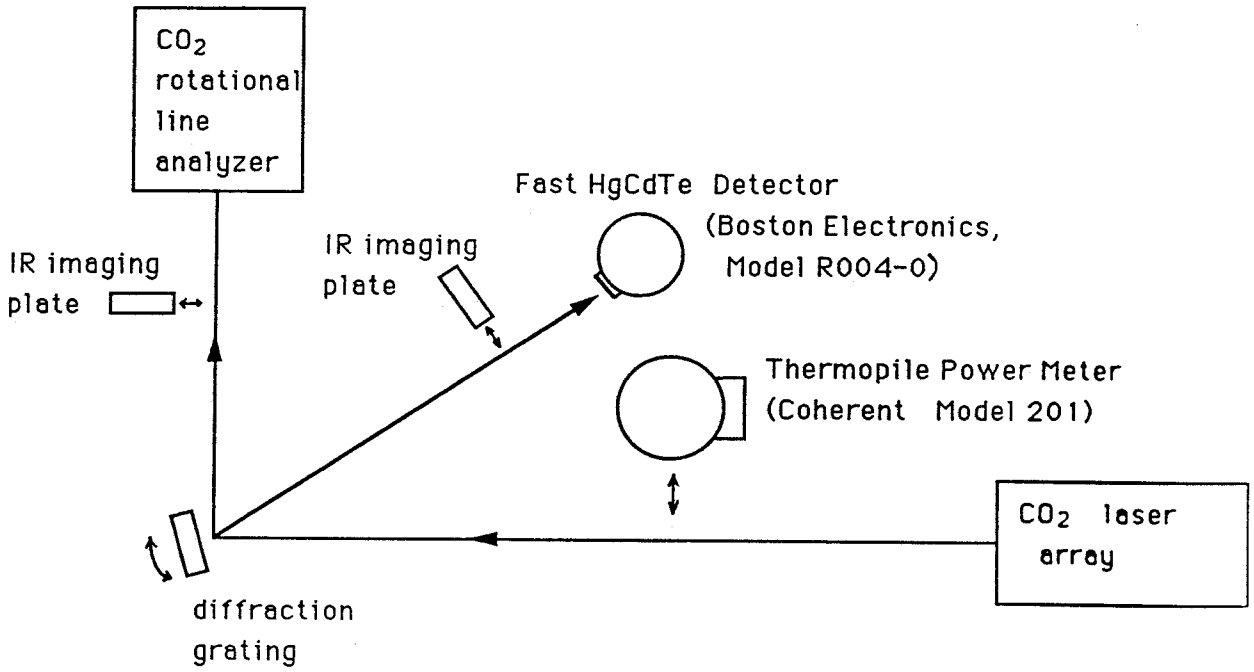

Figure 8. Experimental arrangement for mode coupling measurements.

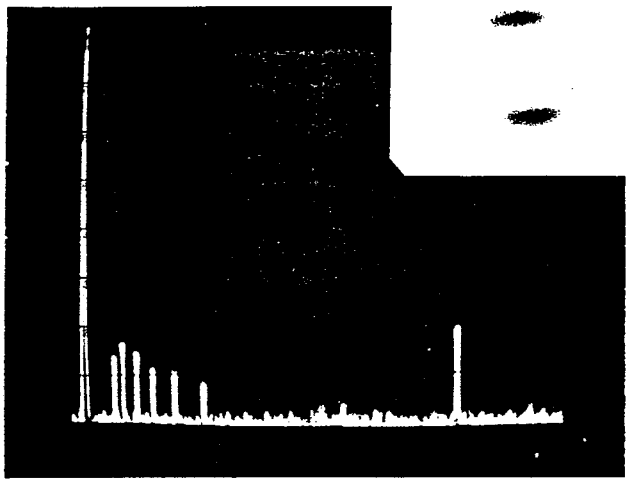

Figure 9. Typical beat spectra for the two-channel waveguide array.

a. A multimode structure

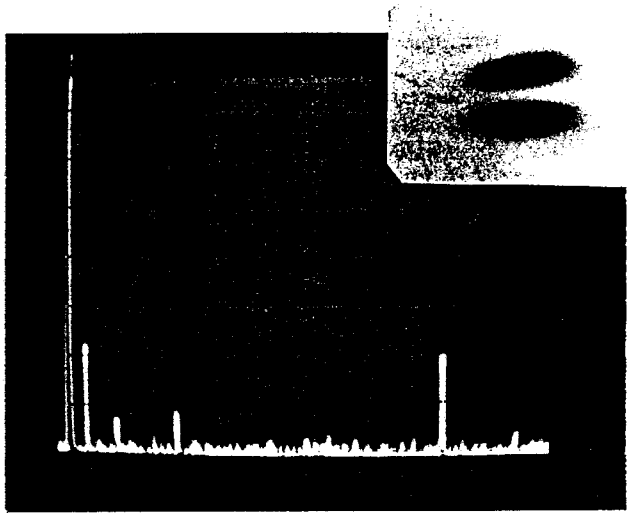

b. Relatively simple coupled mode structure, but still multimode.

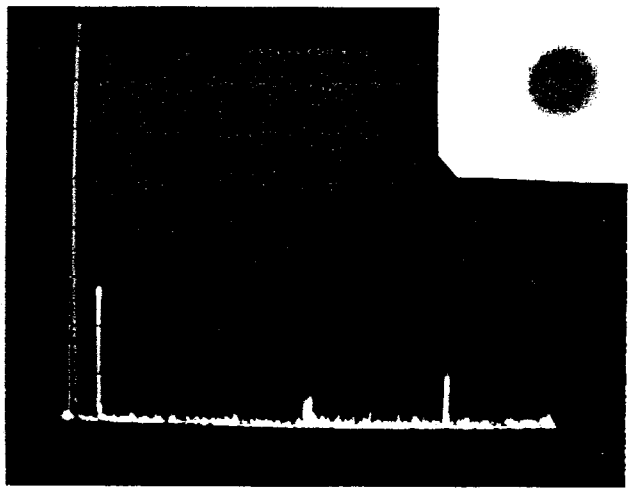

c. Mode from the uncoupled array. Only a single beat note is seen.

uncoupled array in Figure 6b was used, there was only single beat frequency. This frequency could be varied by tilting one of the cavity mirrors, all the way from zero to a maximum value of around 30 MHz. This indicated that the individual bores supported only one mode each. We concluded that the multimode behavior mentioned above arises from the opening in the wall, and we speculate that it is due to the additional gain in the opening, which could support higher-order modes.

Even with this multimode operation, we can still see from the far-field distributions that with proper cavity adjustment, the dominant mode of the two-bore coupled array is either the in-phase or the out-of-phase coupled mode. These two states of operation can both be stable for hours at a time. Figure 10 shows the spatial far-field patterns obtained with the coupled array: (a) in-phase locking, (b) out-of-phase locking, and with the uncoupled array: (c) unlocked operation. Shifting between the in-phase locked mode and the out-of-phase locked mode required only a slight mirror adjustment. However, we noticed that the out-of-phase state would persist over a wider range of mirror tilt and translation adjustments than the in-phase state. This suggested, from the point of view we developed in Chapter 2, that the loss introduced by the intervening wall in the inter-element region is relatively large, so the array favors the out-of-phase coupled mode more than the in-phase coupled mode.

To further confirm this picture, we ran a test with a small additional loss in the inter-element region, introduced by gluing a tiny glass chip to the dividing septum on one end of the guide, as shown in Figure 11. Radiation is still able to couple from one guide to the other over the major portion of the guide length, so phase locked operation could be maintained. We were able to obtain pure out-of-phase locking as indicated by the far field pattern and the lack of beats on the

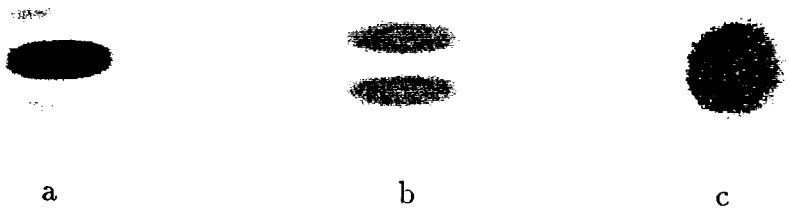

Figure 10. Far-field spatial mode patterns for different locking conditions: a. locked in the in-phase coupled mode, b. locked in the out-of-phase coupled mode, and c. not phase locked.

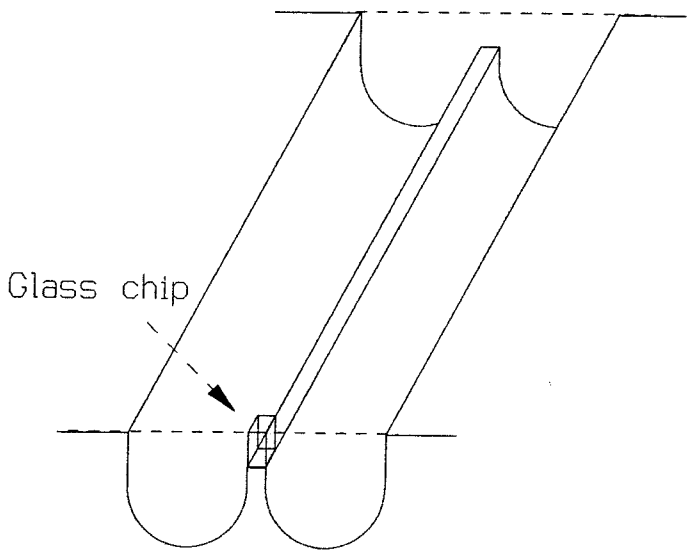

Figure 11. Skech of the coupled two-channel UTRC guide with a small glass tab added that suppressed the in-phase coupled mode while keeping the out-of-phase coupled mode.

spectrum analyzer, but we were unable to obtain the in-phase locking. This is consistent with our analysis in Chapter 2, where we concluded that a large inter-element loss would support the out-of-phase coupled mode only.

The second coupled array we tested was one with the same geometry as in Figure 6a, but the material was aluminum rather than Al_2O_3. This choice was motivated by trying to find a less expensive way to make the coupled array structure; the precision-ground Al_2O_3 arrays from UTRC costed on the order of $1000 apiece. The first question to ask was where would the discharge strike: on top of the wall or within the bore? Paschen's law[11] states that the gas breakdown voltage is a function only of the product of pressure p and the separation between the electrodes, d, and there is a minimum in the curve of the breakdown voltage v.s. pd. The discharge would strike at a location with a characteristic dimension d given by $(pd)_{min}/p$. So with a proper choice of gas pressure, it was possible to obtain discharge inside the bore region instead of at the top of the partial walls. We tested the feasibility of using a total metal structure to strike a discharge in this geometry before we actually made the laser array. The discharge was confined to the bores and looked very uniform within the pressure range that allows laser action, as shown in Figure 12.

We then fabricated a two-bore laser array identical to Figure 5, but made of aluminum. The surface finish was approximately 5 μm rms. A flat ceramic top plate was used as shown in Figure 13. In this two-bore aluminum array test, although the discharge was uniform, we were only able to obtain the out-of-phase coupled mode. No in-phase coupled mode could oscillated no matter how the cavity alignment was adjusted. This was in contrast with the result of the ceramic two-bore array, where we did obtain in-phase coupled mode.

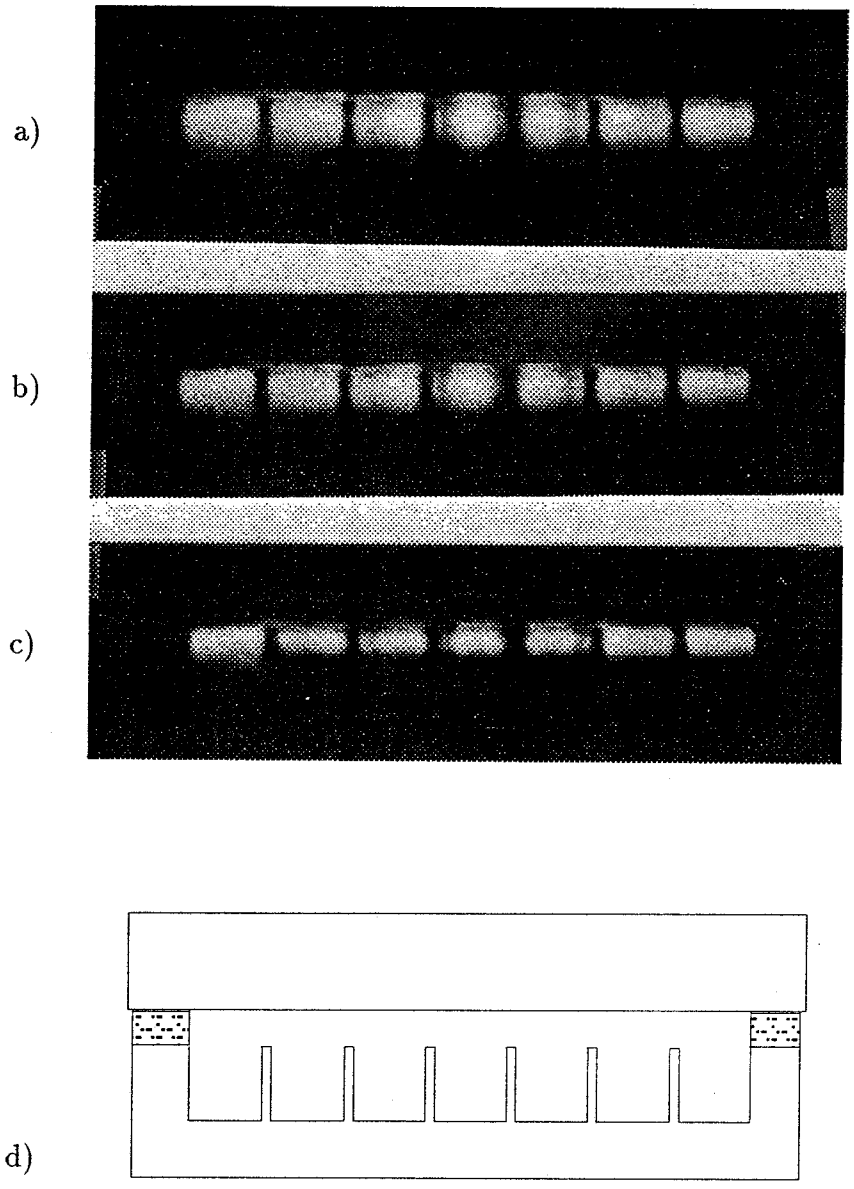

Figure 12. End view of the seven-channel aluminum test section at three different operating pressures: a) 10.7 torr, b) 18.1 torr, c) 32.4 torr. The schematic end-view is shown in d).

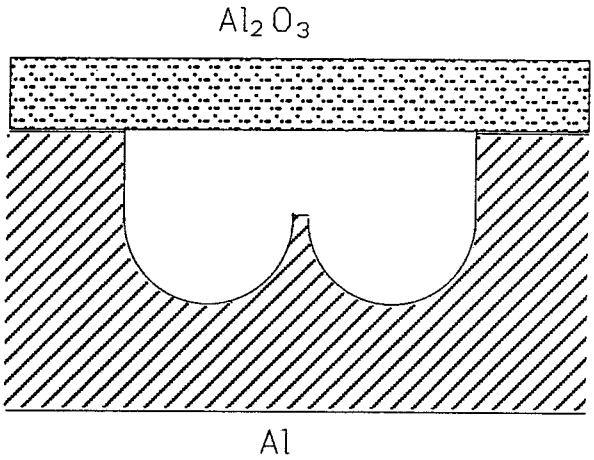

Figure 13. The waveguide array with aluminum body and ceramic top.

An analysis of the loss in the inter-element region of the two arrays reveals the reason for the different behavior of these two arrays. As indicated in Fig.14, we measured the polarization of the laser from the ceramic array to be in the y-direction, i.e., parallel with the electrode surfaces, while the polarization from the aluminum array was observed to be in the x-direction, i.e., perpendicular to the electrode surfaces. These two modes can be approximated with equation (3.1) as EH^{y}_{11} and EH^{x}_{11}, in each guides, respectively. The array materials, ceramic alumina and metal aluminum, are both considered dielectric with some loss. To the first-order approximation, the electric field at the wall top in the ceramic array would also be polarized in the y-direction. Thus the magnetic field is in the x-direction, this yields no surface current at the top of the wall because the surface current is expressed as:

$$\mathbf{J} = \mathbf{n} \times \mathbf{H}, \tag{3.2}$$

where $\mathbf{n}$ stands for the normal direction of the surface at the top of the wall, which is also in x-direction. For the aluminum array, the electric field at the wall top is in the x-direction, so the magnetic field in y-direction. Thus (3.2) tells us

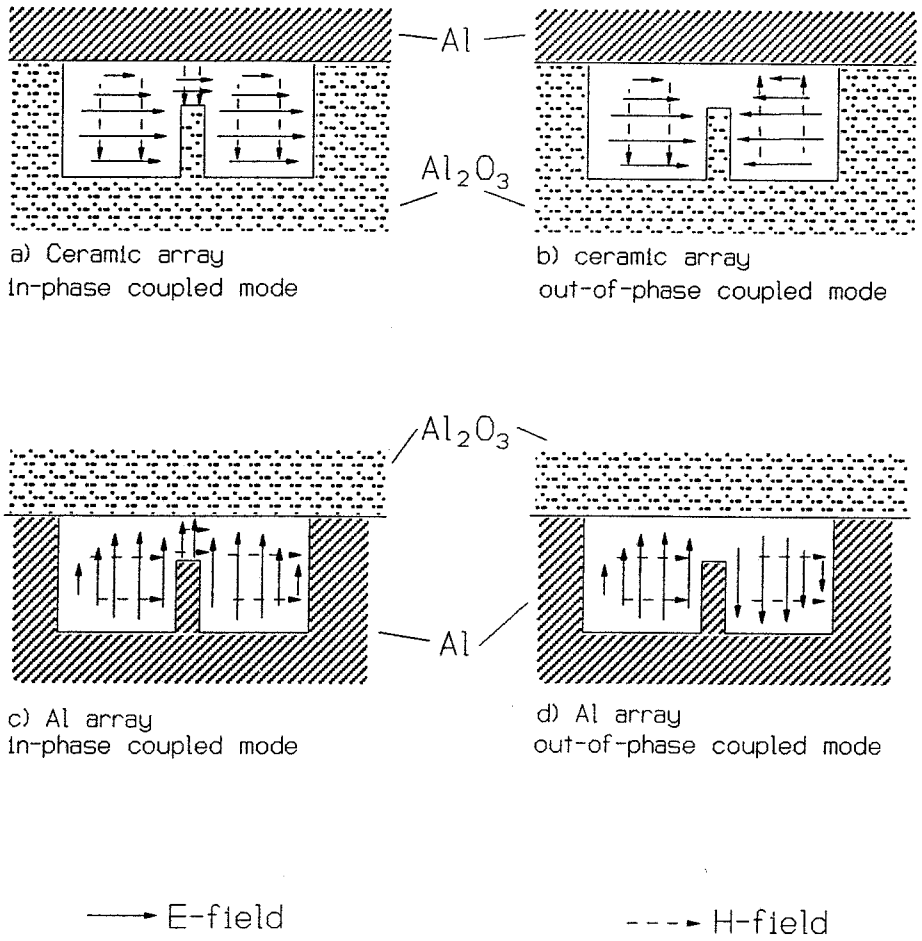

Figure 14. Schematics showing the loss mechanism in the two-channel aluminum array (a and b) and the ceramic array (c and d).

that there is surface current on top of the aluminum wall. This is presumed to be the source of the additional loss. Putting these two cases into the picture we developed in Chapter 2, we see that because it has less loss in the inter-element region, the ceramic-bore array is more suitable for the in-phase coupled mode than the aluminum-bore array.

REFERENCES

1. D.G. Youmans, "Phase Locking of Adjacent Channel Leaky Waveguide CO_2 Lasers," Applied Phys. Lett., Vol. 44, No. 4, pp. 365-367, February 15, 1984.

2. H.R. Schlossberg, U.S. Patent 4,367,554, January 4, 1983.

3. A.D. Colley, K.M. Abramski, H.J. Baker and D.R. Hall, "Power and Frequency Balance in Large Waveguide CO_2 Laser Arrays," CLEO 1990, Anaheim, CA, May 21-25, 1990.

4. A. J. DeMaria and W.B. Bridges, U.S. Patent 4,813,052, March 14, 1989.

5. L.A. Newman, R.A. Hart, J.T. Kennedy, A.J. Cantor, A.J. DeMaria and W.B. Bridges, "High Power Coupled CO_2 Waveguide Laser Array," Applied Physics Letters, Vol. 48, No. 25, pp. 1701–1703, June 1986.

6. G.L. Bourdet, G.M. Mullot and J.Y. Vint, "Linear Array of Self-Focusing CO_2 Waveguide Lasers," IEEE J. Quantum Electronics, Vol. 26, No. 4, pp. 701-710, April 1990.

7. Marcatili and Schmeltzer, "Hollow Metallic and Dielectric Waveguides for Long Distance Optical Transmission and Lasers," The Bell System Technical Journal, July 1964, pp. 1783-1809.

8. K.D. Laakman and W.H. Steier, "Waveguides: Characteristic Modes of Hollow Rectangular Dielectric Waveguides," Applied Optics, 15(5), May 1976; *and* K.D. Laakman, "Hollow Dielectric Waveguides: errata," Applied Optics 15(9), September, 1976.

9. S.E. Somekh, E. Garmire, A. Yariv, H.L. Garvin and R.G. Hunsperger, "Channel Optical Waveguide Directional Couplers," Applied Physics Letters, Vol. 22, p. 46, 1973.

10. A. Yariv and P. Yeh, Optical Waves in Crystals, John Wiley and Sons, 1984.

11. F. Llewellyn-Jones, Ionization growth and breakdown, in Handbuch der Physik, 22, pp. 1–52 (Edited by S. Flugge,) Julius Spriger-Verlag, Berlin, 1956.

CHAPTER 4. SLAB WAVEGUIDE CO_2 LASERS

§4.1 Introduction

At the very beginning of the program, it became apparent through discussions with the UTOS personnel and with ceramic venders that the cost of precision-ground, multiple-waveguide ceramic pieces was going to be very high. In order to be able to pursue our own ideas without the extreme cost of precision grinding, we explored the possibility of making the complicated multiple waveguide pieces out of aluminum and then anodizing it to make the surface look like aluminum oxide, the same as ceramic, and we were successful, as described in Chapter 3 as far as the RF discharge was concerned. However, we were not sure whether the material thus processed would actually behave optically like ceramic, nor what type of anodization was best for a waveguide laser. So we decided to make simple structures first, just to investigate the material side of the problem, and then, if it turned out to be successful, we would proceed to more complex shapes. This simple structure was a pair of slabs, which serve both as electrodes and guiding surfaces for the waveguide (Figure 1). We tested slabs of bare aluminum, and aluminum coated by different anodizing procedures. We also tested different mechanical surface finishes for both the bare aluminum and anodized aluminum. At the beginning, we were not concerned with the multimode operation allowed by the broad cross-sectional area of the slab; our intention was to use it only as a test vehicle for materials, not as a final laser structure.

At the mean time, we became aware of the research work performed by Hall's group on ceramic slab waveguide CO_2 lasers.[1] They used the slab structure as the primary candidate for waveguide lasers, and used small-hole output coupling to avoid high-order-mode oscillation and multi-moding. It turns out that

slab lasers have a lot to offer in their own right.

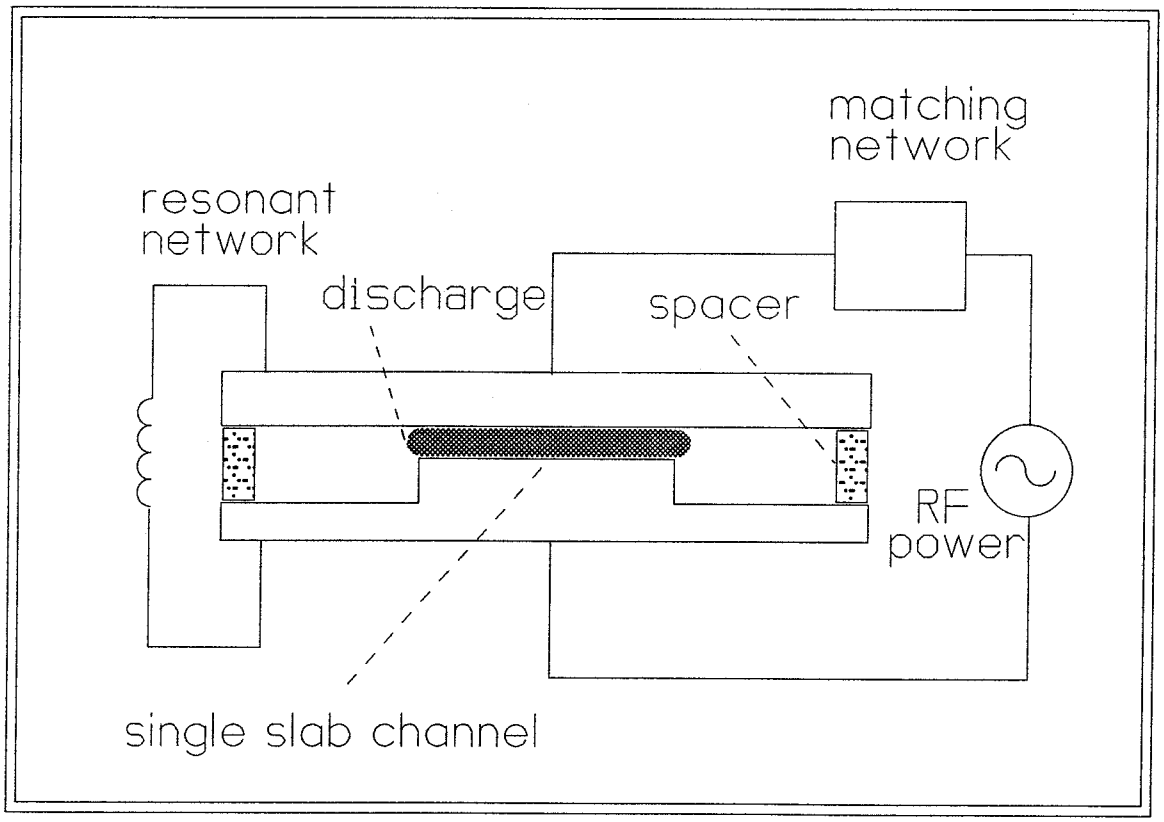

Figure 1. Illustration of a wide area slab waveguide laser.

§4.2 Modes of Slab Waveguide Laser

The mode of a slab waveguide laser shown in Figure 1 can be approximated with a hybrid mode structure: the modes of infinite parallel plates in the x-direction (narrow), and the free-space Hermite-Gaussian mode in the y-direction (wide). The polished slab electrodes provide the wave-guiding in the narrow dimension. In the wide dimension, however, there are no guiding surfaces, so the modes are controlled by the extend of the gain, diffraction losses and the mirror curvature, just as in ordinary (non-waveguide) gas lasers and the field distribution can be described by the free space Hermite-Gaussian modes. A detailed derivation of the modes is given in Appendix A.

A picture of a 3rd order cosine-Gaussian mode is shown in Figure 2. The theoretical transverse intensity distribution is shown at the top, the measured image on a quenched fluorescence screen is shown in the middle, and, for comparison a cosine-cosine mode that would result in a 4-wall waveguide is shown at the bottom. It is clear that the experimental result matches the cosine-Gaussian pattern, with its characteristic non-uniform zero spacing and the higher intensity outer lobes.

In the course of experiments with slab waveguide lasers, we made a deformable mirror and used it as the total reflector in the laser cavity. The deformable mirror utilized polished brass shim stock as the reflecting surface, it could be bent into a cylindrical surface with a variable radius of curvature as shown in Figure 3a. The mirror assembly is made so that its radius of curvature can be changed while the laser is operating. With the normal ***concave*** curvature, the resonator is stable and a high-order Gaussian mode results. As the concave radius increased to infinity (a flat mirror), the laser had a Fabry-Perot cavity and the oscillating mode decreased to the third-order Hermite-Gaussian with four

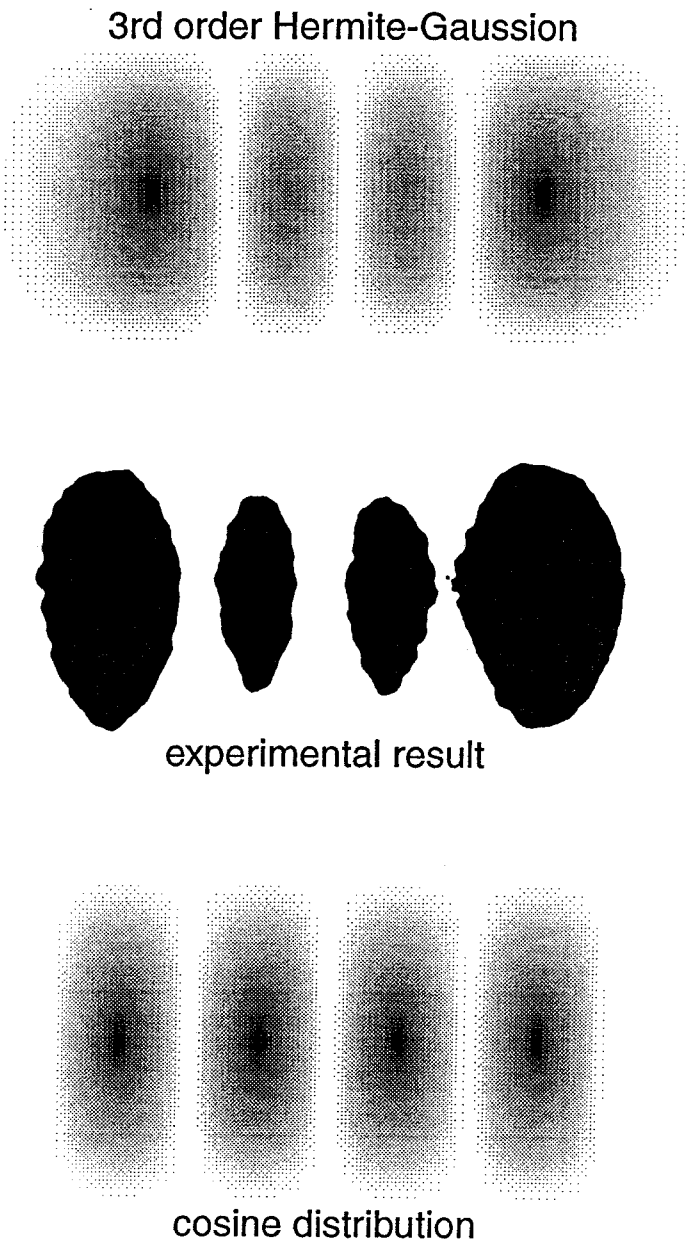

Figure 2. Comparison of the intensity distribution of the experimental measurement(middle) with the theoretical calculation of the 3rd order cosine-Hermite-Gaussian mode(upper) and the a cosine-cosine mode(lower) with the same number of zeros. Resemblance is clearly seen between the experimental distribution and the Hermite-Gaussian mode.

lobes as shown in Figure 3b-d. (These figures were obtained from thermal sensitive paper irradiated by the laser.) When the curvature is adjusted so that this mirror becomes ***convex***, the resonator becomes unstable but the laser continues to oscillate. When the magnification of this unstable resonator is gradually increased (radius of curvature decreased) the order of the lasing mode decreases, as shown in Figure 3b, from d to b, until at last the fundamental Gaussian mode appears, Figure 3b-a. At this point, the radius of curvature is 3.2 meters convex. Because the brass shim was hand polished and hence very lossy, we obtained very low power from this cavity, 1.5 Watts with the third-order mode and 1.1 Watts with the zeroth order mode at 131 Watt RF input. However, these tests allowed us to compare the power from the fundamental (zero-th order) Gaussian mode using the unstable resonator with that of the 3rd Hermite-Gaussian mode which corresponds to a Fabry-Perot resonator when the brass shim mirror is flat: the fundamental mode had 73% of the power of the 3rd order mode. We believe this kind of unstable resonator is a good alternative to the hybrid resonator used by Hall et al.[1], where the edge coupled output would invariably introduce scattering loss. A similar unstable resonator consisting of two convex reflectors were reported by Salzman et al.[2] for broad area semiconductor lasers.

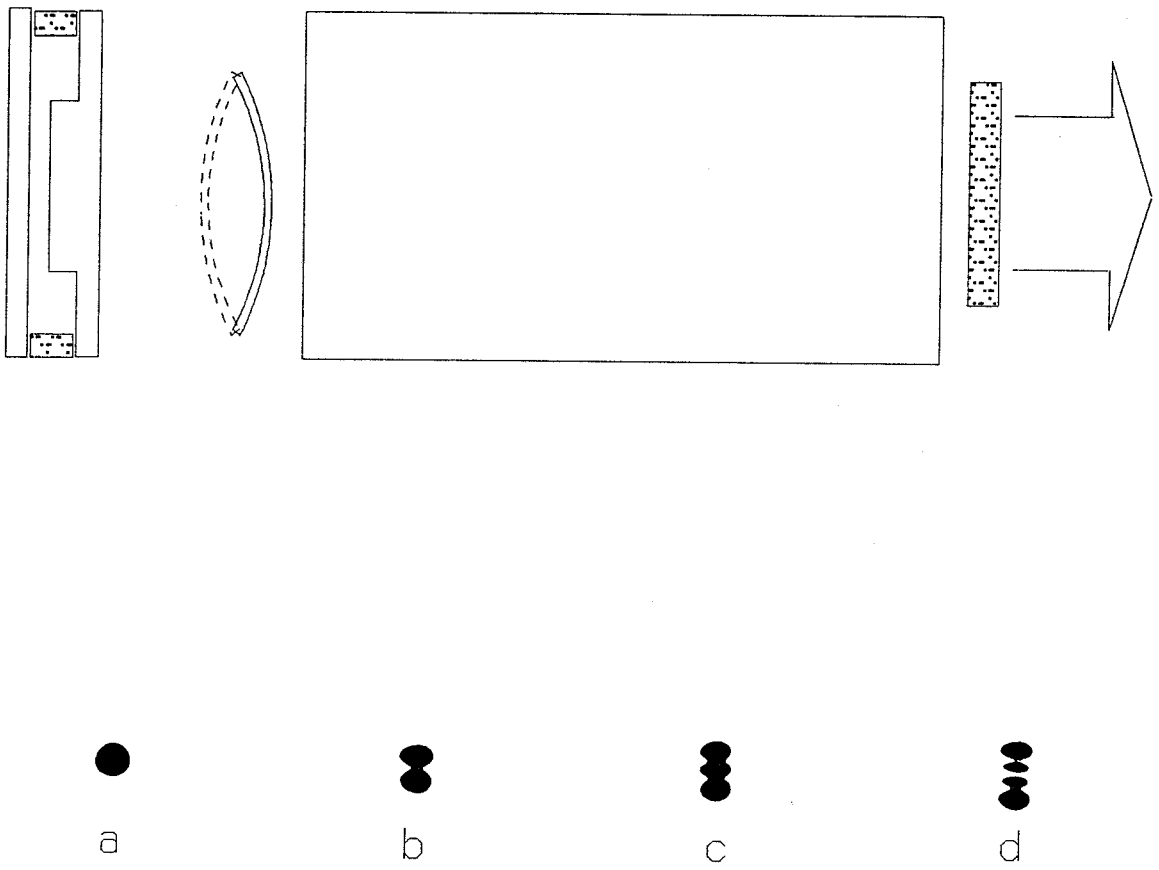

Figure 3. The unstable resonator with a variable convex total reflector, and the different modal intensity patterns corresponding to decreasing radius of curvature of the convex mirror in the order of d to a.

§4.3 Optical Attenuation of Dielectric-Coated Metal Waveguides—Calculation

Yariv and Yeh[3] derived the attenuation coefficient α of leaky slab waveguides of the type shown in Figure 4a by a ray-optics approach:

$$\alpha = -\frac{\ln(R_{12}R_{23})}{2a\tan\theta_2}\,, \tag{1}$$

where R_{12} and R_{23} represent the reflectivity at the interfaces 1-2 and 2-3, respectively. From this equation we see that the loss is related only to the reflectivity of the interface. If the slab waveguide in question is made of lossy material, instead of the lossless material as in Ref. 3, the wave leaking from the interface will be absorbed by the waveguide wall, instead of radiating outwards. The reflected wave is not affected by the loss mechanism, so the loss coefficient should have the same form as in Equation (1), which for symmetric waveguide structure becomes:

$$\alpha_m = -\frac{\ln(R_{12}R_{23})}{2a\tan\theta_2} = -\frac{\ln(R)}{a\,k_z/k_x} = -\frac{m\pi}{a^2 k_z}\ln(R)\,, \tag{2}$$

where $R = R_{12} = R_{23}$, k_x and k_z are the projections of the propagation constant in the x and z-directions, respectively, and m is the order of the waveguide mode.

The reflectivities as a function of the complex refractive index n for both TE and TM modes are derived in Appendix B. The loss coefficient α_m for the m-th mode as a function of gap size a and complex index of refraction n is given as:

$$\alpha_m = \begin{cases} 2m^2\dfrac{\lambda^2}{a^3}\,\mathrm{Re}\left[\dfrac{1}{\sqrt{n^2-1}}\right], & \mathrm{TE}_m \text{ modes} \\ \\ 2m^2\dfrac{\lambda^2}{a^3}\,\mathrm{Re}\left[\dfrac{n^2}{\sqrt{n^2-1}}\right], & \mathrm{TM}_m \text{ modes} \end{cases} \tag{3}$$

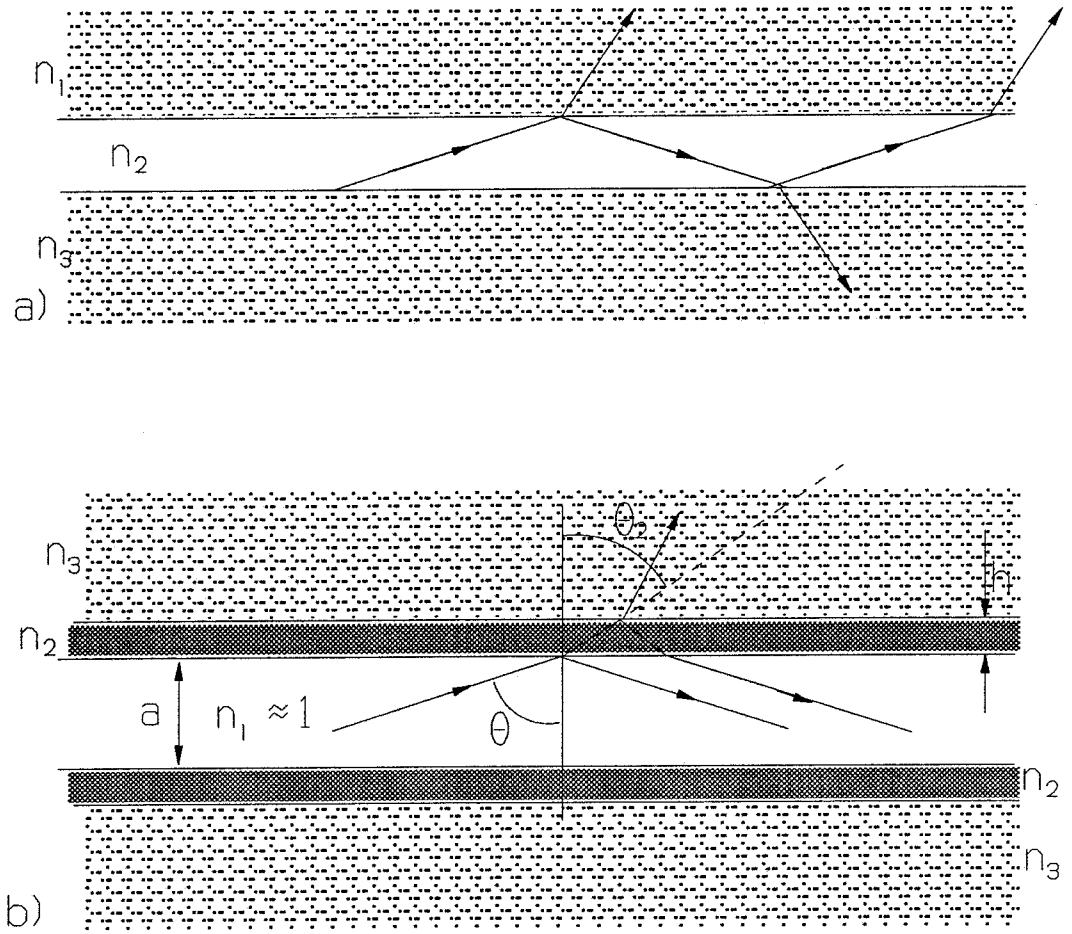

Figure 4. Illustration of (a) a simple parallel plate waveguide, and (b) a parallel waveguide coated with a single layer of dielectric material for a CO_2 slab waveguide laser.

We note that the expressions for α have the same form as those obtained by Marcatili and Schmeltzer[4] for TE and TM modes in the circular guide, obtained by solving Maxwell's equations, apart from the numerical factor out front that arises from the difference in geometry.

Equation (2) should also be true for coated waveguides, shown in Figure 4b, provided the reflection coefficient R includes the effect of the coating, since the reflected wave intensity does not carry any information about the interface that is not already contained in R. We have calculated the wall reflectivities for both TE and TM modes for sample dielectric coatings on aluminum substrates as a function of coating thickness. The equations are derived in Appendix C. In all the calculations we assume a wavelength of 10.6 microns and guide dimensions a = 1.5 mm. The lowest order modes in TE and TM are assumed, hence the incident angle is 89.80°. Values of the optical constants at 10.6 μm are given in Table I:

Table I. Refractive Index at 10.6 μm for Several Materials

material	complex index	reference
aluminum	$27.7 - i94$	5
aluminum oxide	$0.82 - i0.0656$	6, 7
germanium	$4.004 - i1.35 \times 10^{-5}$	6
glass (SiO_2)	$2.24 - i0.102$	6

Figure 5 shows the value of $-\ln(R)$ for the TE mode (electric field parallel to the surface) as a function of coating thickness for Al_2O_3, Ge and SiO_2 coatings on an aluminum substrate. Three different ranges of thickness are shown in Figure 5a, 5b, and 5c. At zero thickness, the value is 4.1×10^{-5}, the value for a bare aluminum surface at an incident angle of $\theta = 89.80°$. All three coating materials initially cause the attenuation to increase from the bare metal value, with Ge causing the fastest increasing and Al_2O_3 the slowest (Figure 5a).

At a thickness somewhat greater than 0.6 microns, the attenuation with the Ge film peaks sharply, a resonance in the coating layer. We can see from Figure 5c that this peaked loss function occurs periodically with the Ge coating, and also with the SiO_2 coating, but not with the Al_2O_3 coating. Figure 6 gives the variation of $-\ln(R)$ for Al_2O_3 layers out to 10 microns thickness, where it approaches the value for an infinite thickness of the coating material, 0.00373. The lack of resonant peaks occurs because the real part of the refractive index is less than unity, and the total internal reflection occurs at the vacuum–Al_2O_3 interface (modified slightly by the finite imaginary part of the refractive index). It is impossible for the wave to resonate in the coating layer, as in Ge and SiO_2.

Figure 7 shows similar calculations for the TM mode (electric field in the plane of incidence, which means nearly normal to the surface for $\theta = 89.80°$). For this mode, the bare aluminum losses are much higher, $-\ln(R) = 0.353$. Germanium and SiO_2 coatings initially decrease the attenuation (Figure 7a) from 0.353, but exhibit attenuation peaks at larger thicknesses (Figure 7c). Aluminum oxide, on the other hand, initially increases the attenuation for very thin layers, with an broad peak at about 0.03 microns (Figure 7a), then decreases smoothly to the infinite-thickness value of 0.0050 beyond 5 microns thickness (Figure 7b).

(a)

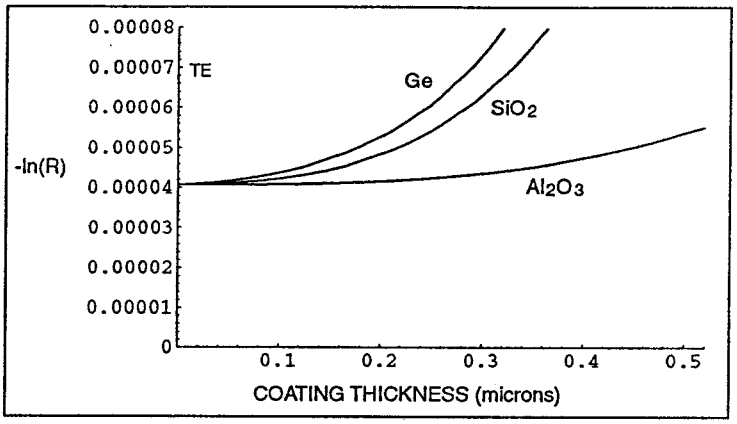

(b)

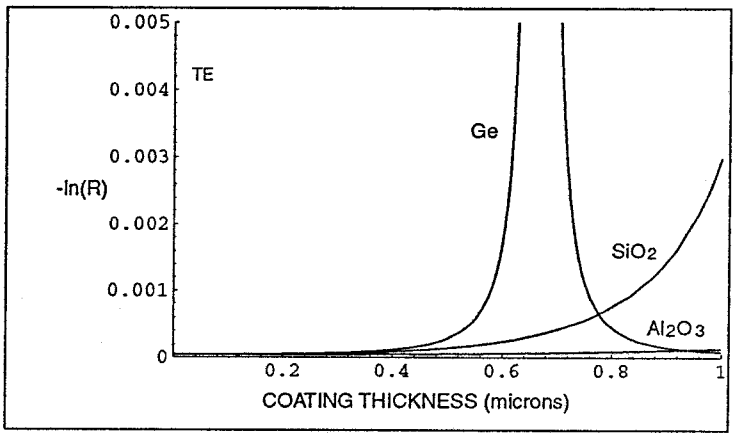

(c)

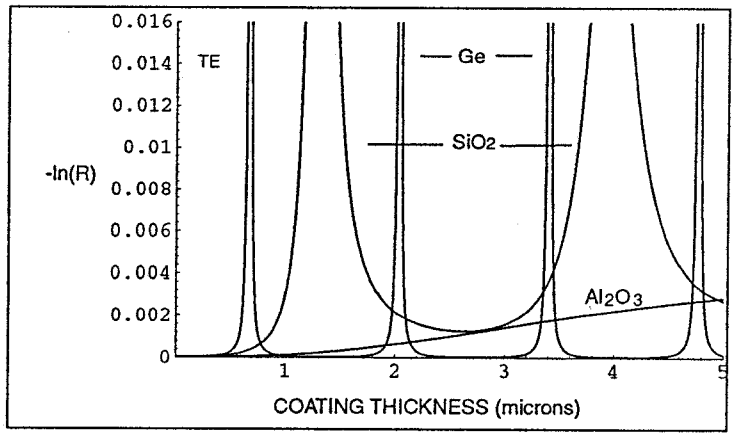

Figure 5. Values of -ln(R) for Al_2O_3, Ge, and SiO_2 coatings on aluminum as functions of coating thickness for TE modes and for various ranges: (a) 0 to 0.5 μm; (b) 0 to 1 μm; and (c) 0 to 5 μm.

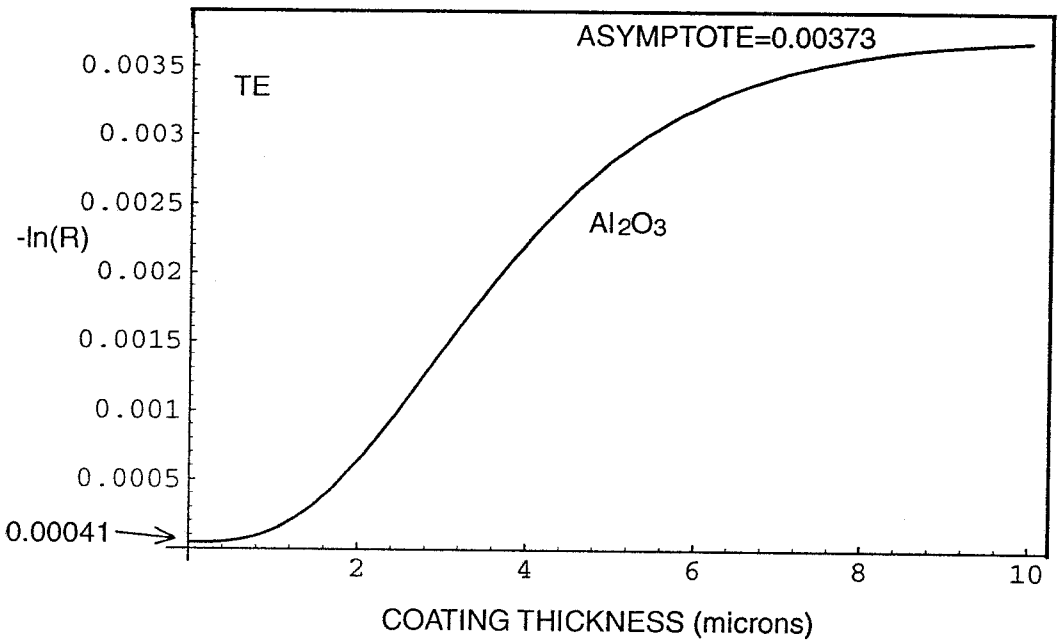

Figure 6. Value of -ln(R) as a function of thichness for an Al_2O_3 coating on aluminum for TE modes.

(a)

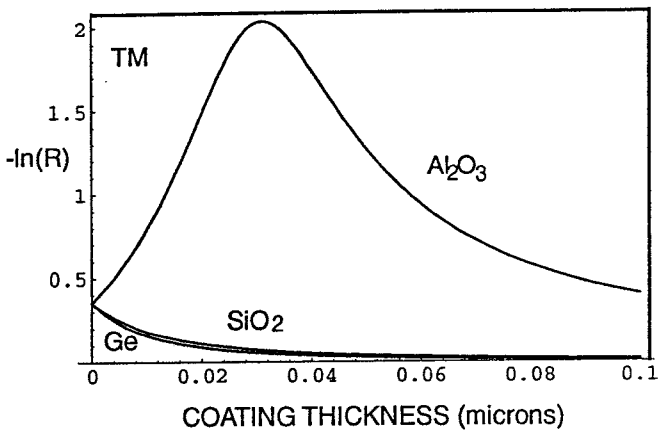

(b)

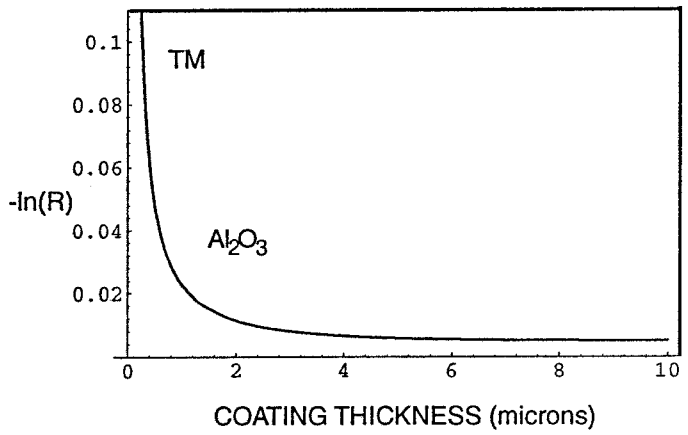

(c)

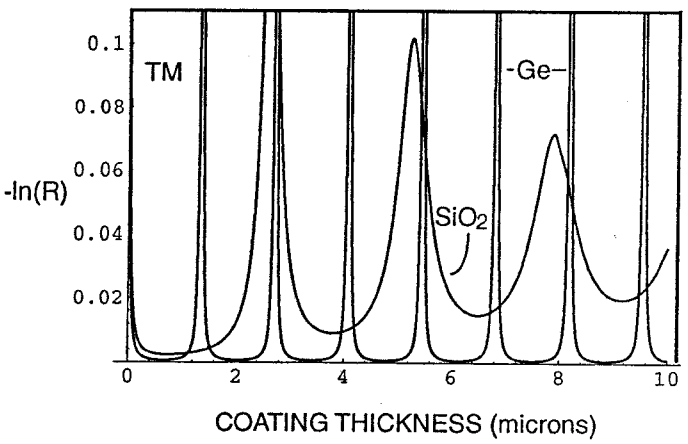

Figure 7. Values of Al_2O_3, Ge and SiO_2 coatings on aluminum as functions of coating thickness for TM modes at various ranges: (a) 0 to 0.1 μm; (b) Al_2O_3 0 to 10 μm; and (c) Ge and SiO_2 0 to 10 μm.

In order to apply these analyses to a two-dimensional rectangular waveguide, the intrinsic modes of which are the EH–modes, we can use the technique proposed by Laakman and Steier[8]. In this technique the loss suffered by the EH_{11} mode is approximated by the loss suffered by TE_{01} mode on two parallel walls and the loss by TM_{01} mode on the other two walls.

From the data presented above we can draw several conclusions about the design of waveguides for CO_2 lasers:

(1) It is possible to use aluminum for two of the four walls and dielectric for the other two walls. This was already suggested by Laakman and Steier[8] and Adam and Kneubühl[9]. The mode of oscillation will have its electric field vector parallel to the metal walls.

(2) Coatings over aluminum of a lossy dielectric such as Al_2O_3 only a few microns thick will look just like a wall of infinite thickness. Thus the dielectric walls described in (1) can also be metal underneath. Such coatings are easily obtained by anodization.

(3) Coatings over aluminum of low or intermediate loss material such as Ge and SiO_2 can also be used to good advantage provided they are made the proper thickness (about 0.5 to 1 μm), and might be superior in optical loss to thick coatings of Al_2O_3. However, they are quite likely to be more difficult to apply and may be less durable in the discharge environment.

§4.4 Comparison of Experimental Results with Different Surface Finishes

Having discovered that we could obtain a uniform, non-filamenting discharge in the region between two parallel aluminum plates, that the laser output power was only a little lower than what we could obtain with the channel waveguides, and that we could obtain single mode operation with relative ease, we decided to make a parametric study of this geometry in addition to simply comparing surface finishes.

We observed in §4.3 that the optical attenuation coefficient (in 1/meter) should increase as the inverse cube of the separation between the parallel plates. The small-signal gain in our pressure range, on the other hand, should remain about constant provided the pressure is changed to make pd constant[10]. Eventually the waveguide loss will become significant and finally overcome the gain as the plate separation is decreased, and the performance should suffer. The fixed losses (mirror absorption, output coupling fraction) do not change with the plate separation (to first order; there are second order effects caused by diffraction in the short space separating the mirrors from the ends of the guide). Just where the waveguide loss becomes the dominating factor was not known initially, since we had only theoretical estimates for that loss.

We undertook a series of experiments with metal plates 20 mm wide by 370 mm long, a considerably wider laser than the two-channel laser, which had an overall size of about 5 mm by 370 mm. The mirrors used for these experiments had 99.5% reflectivity for the feedback mirror, and 90% reflectivity for the output coupler. Both mirrors were flat. The first set of metal plates were evaluated just as they came from a standard milling machine. We estimate the surface roughness for those plates as 2 micrometers rms. The results are shown in Figure 8, with the power output plotted v.s. gas fill pressure (using our standard mix of

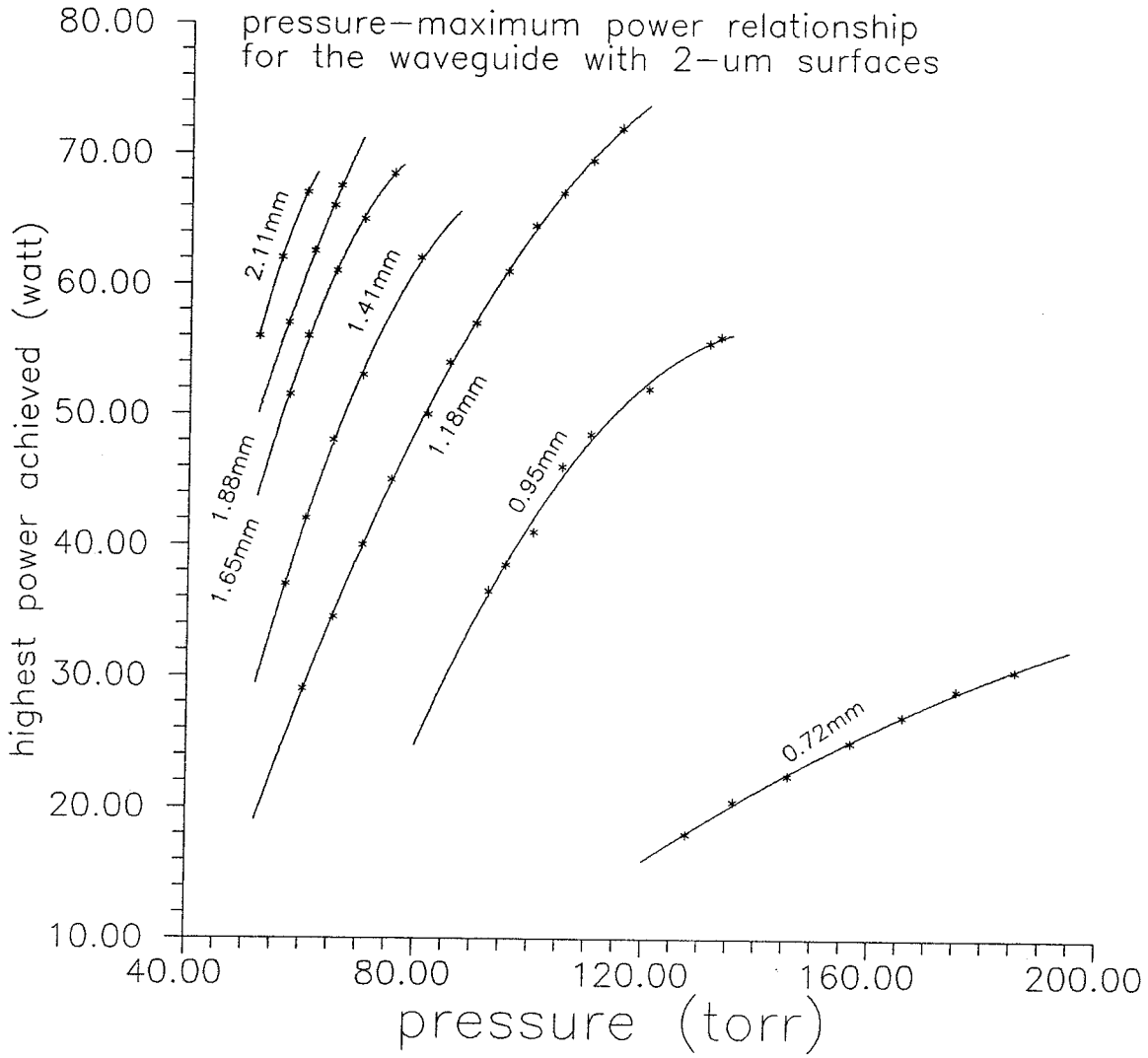

Figure 8. Pressure-maximum power relationship for the milling-machine surface finish, with an rms roughness of about 2 μm. An apparent power drop occurs at a plate-spacing between 1.18mm to 0.95mm.

CO_2:N_2:He of 1:1:6) with the plate separation as a parameter. We were not able to reach the optimum pressure point, limited by our r-f measurement power to about 1 kw at 146 MHz. Clearly, the smaller separations prefer higher pressures, as we would expect from pd=constant scaling laws for glow discharges. And we see that down to separations of about 1 mm, we were able to maintain the same maximum output power, indicating that the waveguide losses aren't increasing too rapidly. Below about 1 mm separation, there is a serious fall-off in power. We think this is evidence that the waveguide losses are comparable to the mirror and end-diffraction losses at about that spacing, and then increase rapidly as the inverse cube at smaller spacings.

Figure 9 shows a similar set of curves taken with a pair of aluminum plates that were roughened with sandpaper after being machined. We estimate the surface roughness for these as 9 micrometers rms. We note that these curves are not much different from those of Figure 10, maybe just a little worse. Figure 10 shows another similar set of curves, taken with aluminum plates polished by an outside firm, Jancur Gauge Co., that claimed a finish with 0.1 micrometers rms roughness. Figure 11 shows another set taken with as-milled plates that had been anodized with a coating thickness of 5 micrometers Al_2O_3. From Figure 6 we can estimate that this coating would increase the loss by a factor of 50 from bare aluminum for the TE modes, assuming, or course, that our "bare aluminum" samples had little or no natural oxide layers. However, the curves with the anodized coatings are not significantly different from the others. All these curves are surprisingly similar in performance, indicating that neither surface finish nor material finish is of first-order performance in determining the operating parameters, in our range of roughness. We have plotted samples of all four finishes in Figure 12 for comparison. Unfortunately, we were unable to reproduce

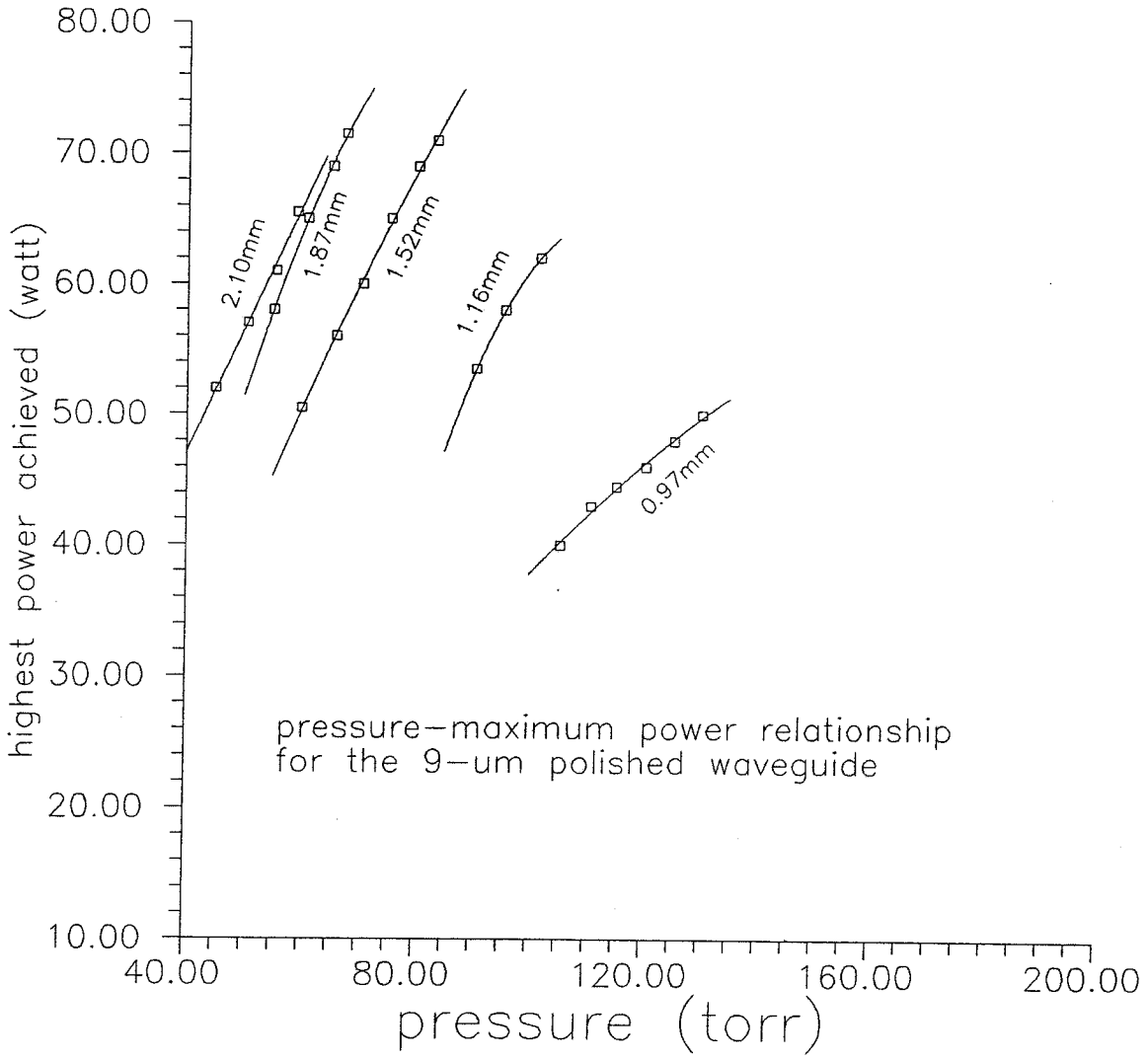

Figure 9. Pressure-maximum power relationship for the 9 μm surface finish. The power drop occurs at a spacing of around 1.16 mm.

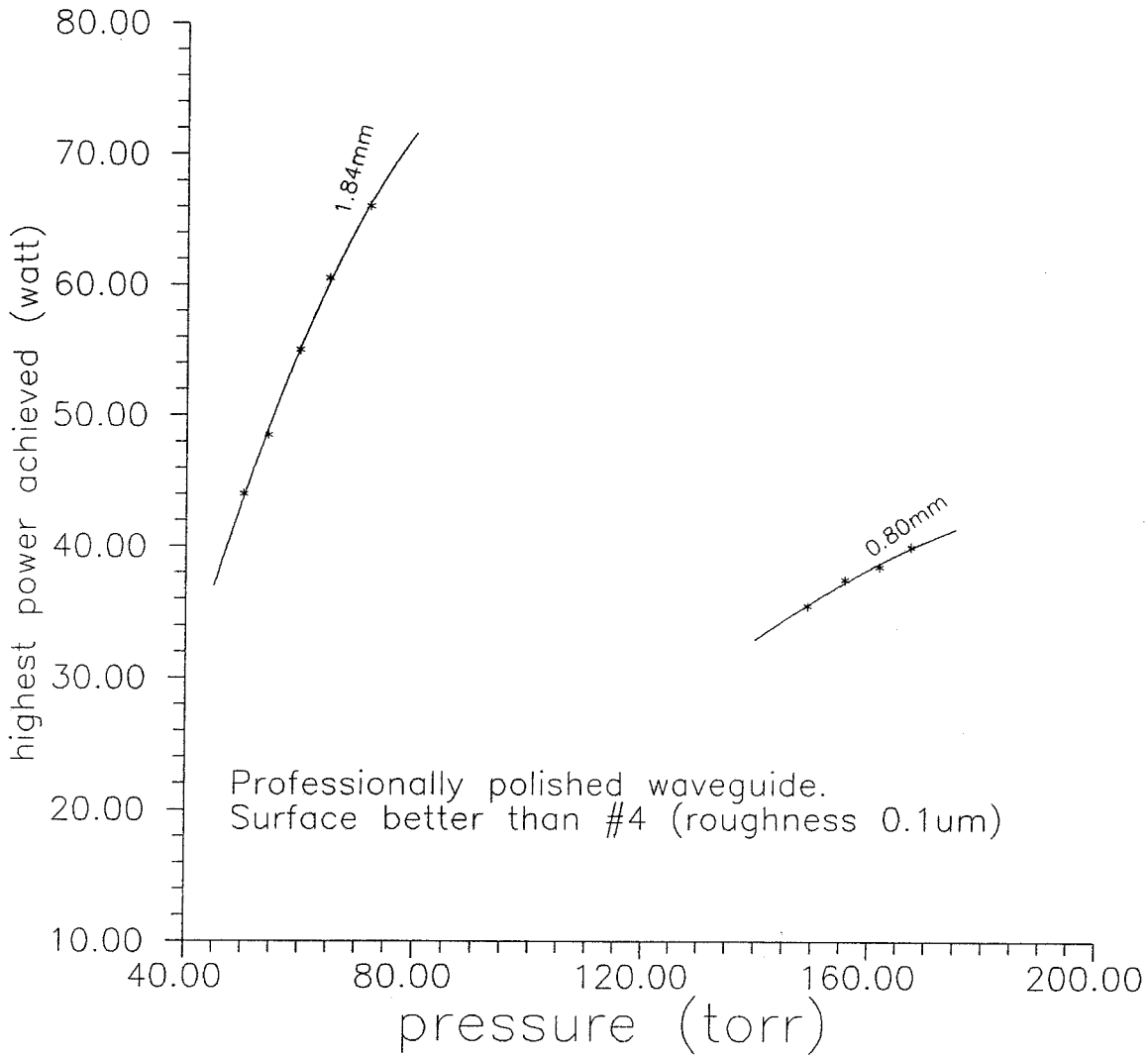

Figure 10. Pressure-maximum power relationship for a pair of professionally-polished surfaces with a rms roughness around 0.1 μm. Power drop similar to that in Figure 8 and Figure 9 is seen.

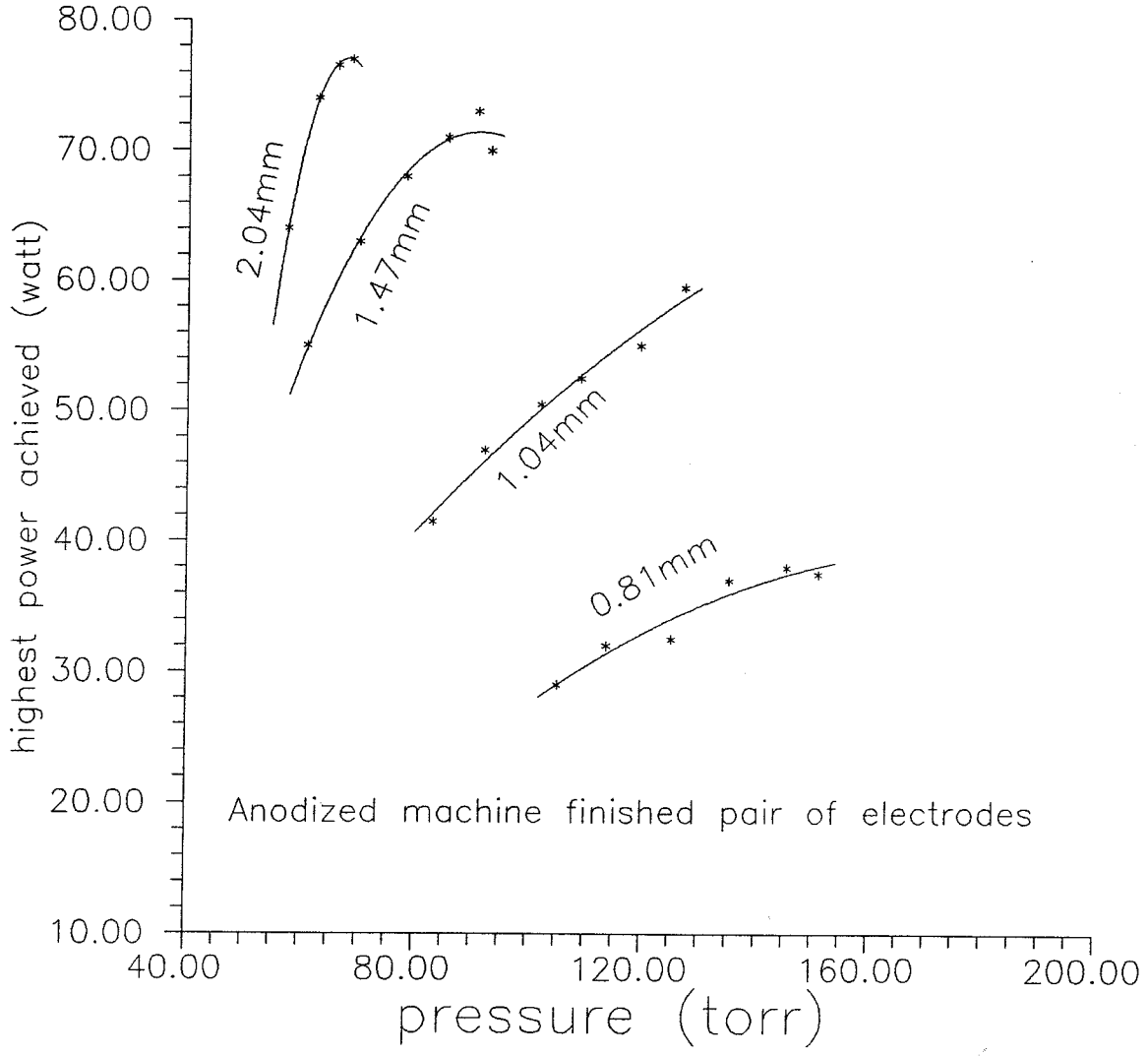

Figure 11. Pressure-maximum power relationship for the anodized milling-machine surface finish, rms roughness is about 2μm. Power drop is again similar to the previous cases in Fig.s 8 through 10 as the plate spacing is reduced from 1.04 mm.

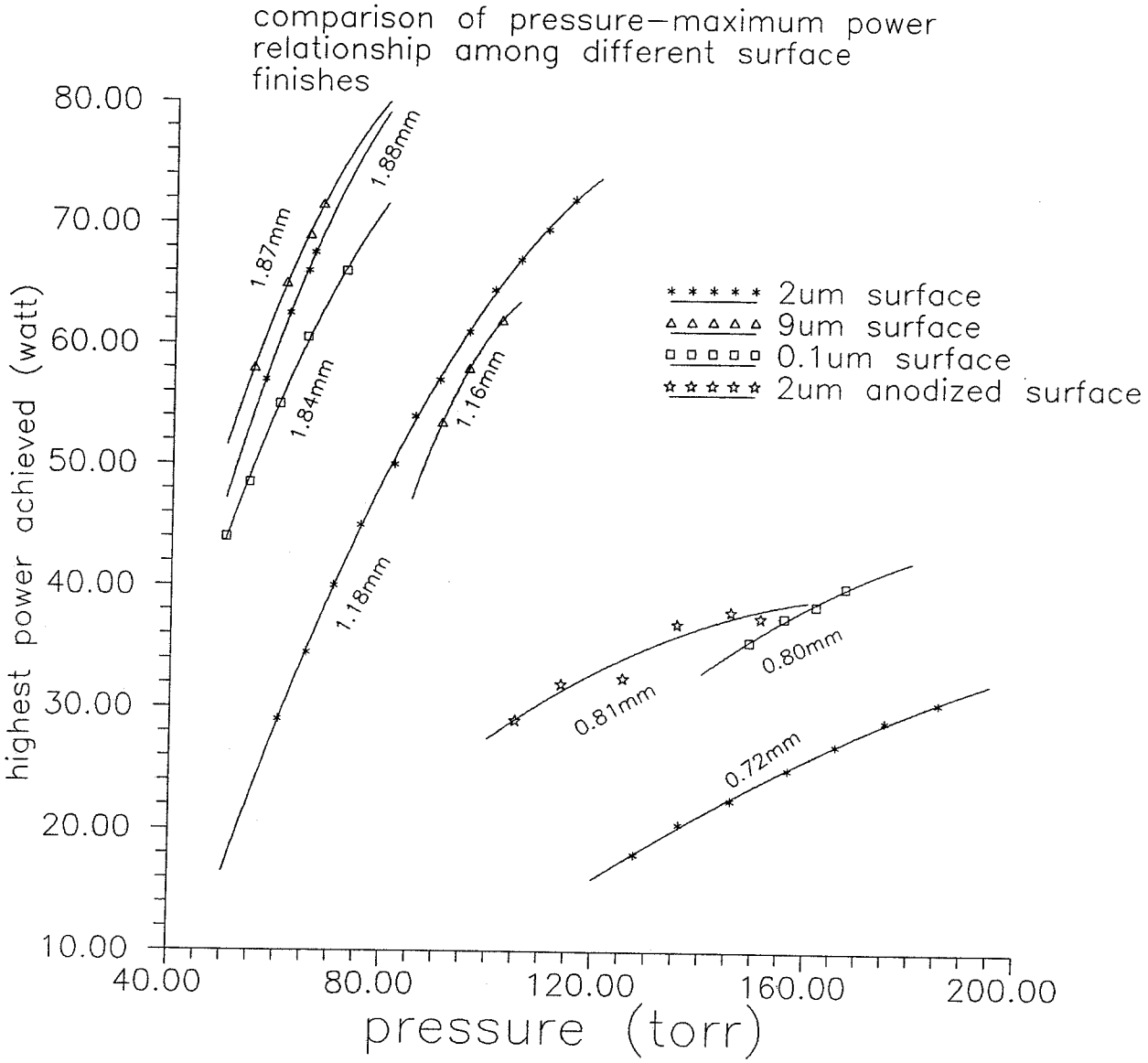

Figure 12. A comparison of the pressure-maximum power relationship among different surface finishes. Although there are some differences, it is seen that the general trend is the same for all of them.

the glass spacer thickness accurately from one set of plates to another, so the plate spacings are not exactly the same within each group; nevertheless, no clear advantage of one finish over the other is evident from Figure 12. We should note that the laser output was polarized parallel to the waveguide plates (TE) in all cases. Since there seems little choice between the finishes studied, it would seem that we would be able to recommend the cheapest (as-milled) and an anodized finish to reduce discharge erosion of the plates (since they are also the discharge electrodes and suffer ion bombardment) and reduce chemical clean up of the discharge oxygen (from dissociated CO_2) by oxidizing a bare metal surface.

§4.5 Calculation of Laser Power at Different Gap Sizes

All the above measurements indicate that the loss related to the gap size of the slab waveguide plays a major roll only when the gap is small. We applied the laser oscillation theory and confirmed such a trend. For steady state oscillation of the laser, the gain of a homogeneously broadened medium must be equal to the loss:

$$e^{2\gamma \mathcal{L}} - 1 = L, \tag{4}$$

where γ is the loss coefficient, $\mathcal{L}$ is the length of the gain medium, and L is the total loss. The gain is usually very small, so the right hand side of this equation is approximately $2\gamma\mathcal{L}$. If we define the distributed loss as

$$\alpha \equiv \frac{L}{2\mathcal{L}}, \tag{5}$$

then

$$\gamma = \frac{\gamma_0}{1 + \frac{I}{I_s}} = \alpha, \tag{6}$$

where γ_0 is the small signal gain coefficient, and I_s is the saturation intensity, which increases quadratically with the pressure[11]. α can be partitioned into waveguide loss, diffraction loss and cavity mirror loss (see Figure 13a):

$$\alpha = \alpha_g + \alpha_d + \alpha_m \ . \tag{7}$$

The waveguide loss coefficient from Equation (4.3) can be written as:

$$\alpha_g = c_g \frac{2\lambda^2}{a^3} \mathrm{Re}\left[\frac{1}{\sqrt{n^2 - 1}}\right], \tag{8}$$

where λ is the laser wavelength, a is the gap size, n is the complex index of refraction for the waveguide material, and c_g is a dimensionless coefficient we introduced to include the enhancement of the loss by the surface roughness.

The diffraction loss α_d occurs when the light exits the waveguide and is reflected back by the mirrors. We use the Fraunhofer diffraction as an approximation to estimate the diffraction angle:

$$\theta = 2.44\frac{\lambda}{a}\ , \tag{9}$$

and the area that the light misses when it comes back from the mirror. The lost power should be proportional to the relative area missed by light. Because of the

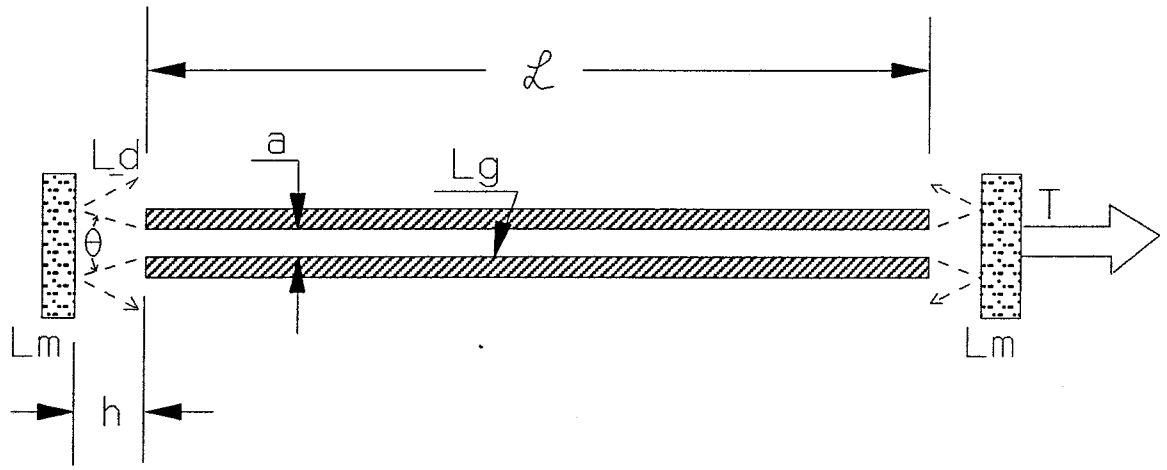

(a)

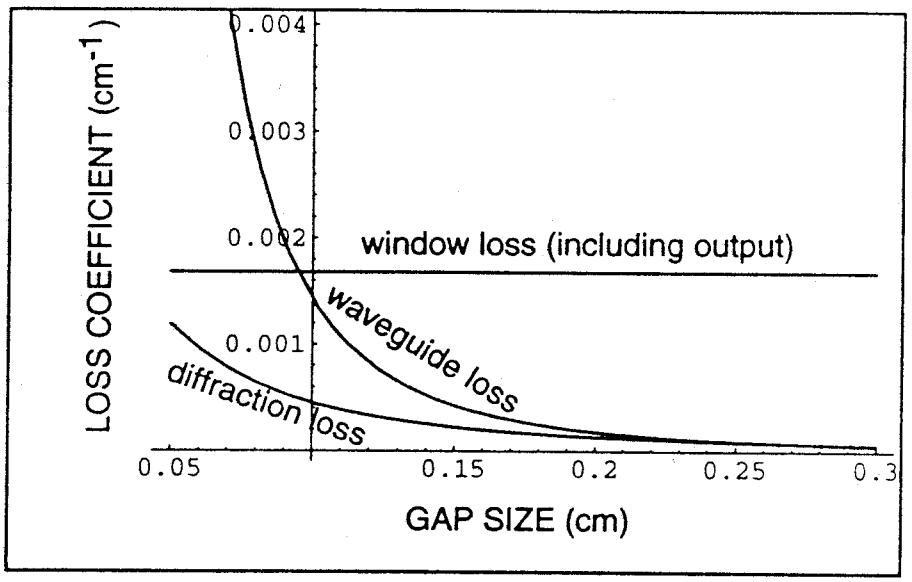

(b)

Figure 13. (a) Schematics showing various loss mechanisms; (b) Comparison of the losses over a range of plate-spacings. The sum of the waveguide loss and the diffraction loss becomes comparable to the output loss at around 1 mm.

sinusoidal distribution of the field across the gap, there is less diffraction at the exit. Thus the power lost should be less than case of uniform distribution and α_d is written as:

$$\alpha_d = c_d \frac{h\theta}{a + h\theta} \frac{1}{\ell} , \tag{10}$$

where c_d is the correction factor that is less than 1 to account for the fact that the laser distribution is not uniform, h is the distance from the end of the waveguide to the mirror, ℓ is the cavity length.

α_m is the mirror loss, including both that due to the output (T) and that due to the absorption (A_b) at the mirror surfaces:

$$\alpha_m = -\ln[1 - T - A_b] \frac{1}{2\ell} . \tag{11}$$

The intensity inside the cavity is considered to be the sum of the intensities of the two traveling waves in opposite directions, so the output laser power P is related to the average intra-cavity intensity I by:

$$P = 0.5 \, ATI , \tag{12}$$

where A is the area of the laser beam cross-section, which we take as $a \times 2$ cm^2. This equation in combination with the laser gain equation yields:

$$P(a,p) = a s p^2 T \left[\frac{\gamma_0}{\alpha(a)} - 1 \right] , \tag{13}$$

where a stands for the gap size and p for the pressure, and the saturation intensity

is written as $I_s \equiv sp^2$, and s is a coefficient[Watt/cm^2-torr^2]. From our measurements, it was found that pa $= 12 \sim 13$[cm $\cdot$ torr], so we take p=12.5/a in our calculation. Thus (11) becomes:

$$P(a) = 12.5^2 \frac{s}{a} T \left\{ \frac{\gamma_0}{c_g \frac{2\lambda^2}{a^3} \mathrm{Re}\left[\frac{1}{\sqrt{n^2-1}}\right] + \frac{c_d}{\ell} \frac{2.44h\lambda}{a^2 + 2.44h\lambda} + \frac{1}{2\ell} \ln\left[\frac{1}{1\text{-}T\text{-}A_b}\right]} \right\}. \quad (14)$$

Table II lists the numbers used for the calculation. Figure 13b shows the various loss mechanism plotted as functions of gap spacing. The surface roughness parameter c_g was varied to fit the data. It is seen that as the gap decreases, the loss due to waveguide absorption and diffraction at the ends of the waveguide increase, while the loss due to mirror loss is a constant. Figure 14 shows the calculated laser power as a function of the gap size for two different surface finishes. It agrees with the general trend of the experiment results.

Table II. Parameters for Power Calculation

parameter	value	unit	reference
ℓ	38.1	cm	actual value
γ_0	0.08	cm^{-1}	mid-range Ref. 11
T	0.1		actual value
A_b	0.02		estimate
n	27.7-i94		Ref. 6
c_g	varies		taken as parameter
c_d	0.1		estimate
λ	0.00106	cm	actual value
s	0.3	$W/(cm\,torr)^2$	chosen to fit curve[1*]
h	0.5	cm	actual value

[1*] In Ref. 10, this value was measured to be about 0.42.

(a)

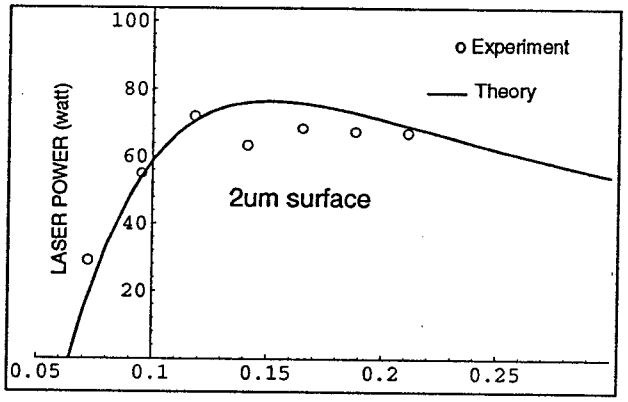

(b)

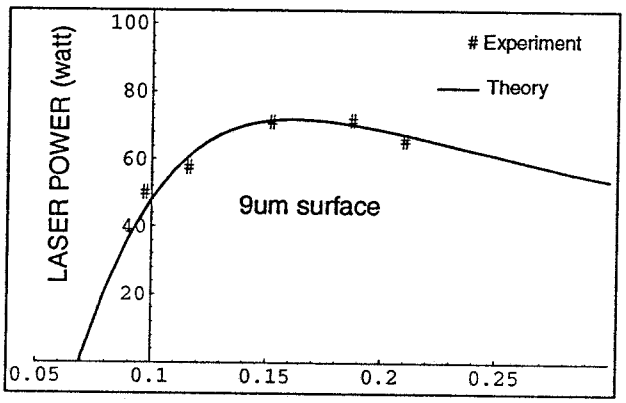

(c)

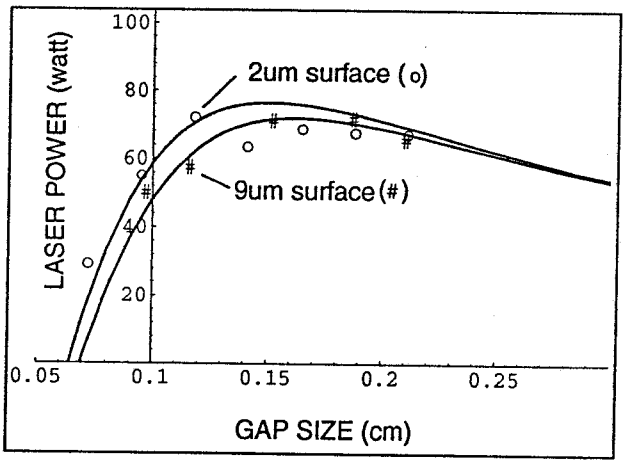

Figure 14. The optimum power output as a function of the waveguide plate spacing. Good agreement between the calculation and experimental results with two different surface finishes is seen. (a) $c_g = 220$; (b) $c_g = 280$; (c) a comparison between the two surface finishes.

Appendix A. Modes of the Slab Waveguide Laser

Using a pair of infinite plates and assuming a TE-like mode:

$$\mathbf{E} = E_y e^{i\omega t}\mathbf{j}\,, \quad \mathbf{H} = \sqrt{\frac{\epsilon}{\mu}} E_y e^{i\omega t}(-\mathbf{i}); \tag{A.1}$$

where **i** and **j** are unit vectors in the x and y direction respectively. The electric field satisfies the Helmholtz equation:

$$\nabla^2 E_y + k^2 E_y = 0, \quad k = \omega\sqrt{\mu\epsilon}\,. \tag{A.2}$$

Assuming the solution for E_y is separable in spatial dimensions:

$$E_y(x,y,z) = E_0 X(x)\psi(y,z)e^{-ikz}. \tag{A.3}$$

Substituting (A.3) into (A.2) and applying the boundary conditions for a perfect conductor to the electric field at the surfaces of the two conductors, we have:

$$X(x) = \sin(\frac{m\pi x}{a}), \quad m = 1, 2, 3, \cdots; \tag{A.4}$$

the differential equation for $\psi(y,z)$ is obtained after suitable approximations:

$$\frac{\partial^2\psi}{\partial y^2} - 2ik\frac{\partial\psi}{\partial z} - (\frac{m\pi}{a})^2\psi = 0, \tag{A.5}$$

where we assumed

$$\frac{\partial^2\psi}{\partial z^2} \ll k\frac{\partial\psi}{\partial z}\,. \tag{A.6}$$

This equation is then solved by the conventional method[11] by assuming the form of ψ to be

$$\psi(y,z) = \exp\left\{-i\left[P(z) + \frac{k}{2q(z)}y^2\right]\right\}. \tag{A.7}$$

Substituting ψ in (A.5) according to this equation, we obtain the equations for P and q:

$$\frac{-ik}{q(z)} - 2kP'(z) + \frac{k^2y^2}{q^2(z)}[q'(z) - 1] - (\frac{m\pi}{a})^2 = 0. \tag{A.8}$$

By comparing terms of equal powers in y, we have $q' = 1$. Then

$$q(z) = z + q_0\,. \tag{A.9}$$

And the differential equation for P is:

$$P'(z) = \frac{-i}{2}\frac{1}{q_0 + z} - \frac{1}{2k}(\frac{m\pi}{a})^2\,. \tag{A.10}$$

Then P can be solved as:

$$P(z) = \frac{-i}{2}\ln(q_0 + z) - \frac{z}{2k}(\frac{m\pi}{a})^2 + \text{constant}. \tag{A.11}$$

Requiring $P(0) = 0$, then the constant becomes $\frac{i}{2}\ln(q_0)$, and P becomes

$$P(z) = -\frac{1}{2}(\frac{m\pi}{a})^2 \frac{z}{k} - i\frac{1}{2}\ln(1+\frac{z}{q_0}) \ . \tag{A.12}$$

If q_0 is imaginary, as in the case of two-dimensional Gaussian beams,

$$-\frac{1}{2}\ln(1+\frac{z}{q_0}) = \ln\frac{1}{(1+|\frac{z}{q_0}|^2)^{1/4}} - \frac{i}{2}\arctan(\frac{z}{q_0}) \ . \tag{A.13}$$

Express q_0 the same way as in the two-dimensional case:

$$q_0 = i\frac{\pi {w_0}^2}{\lambda}, \tag{A.14}$$

where w_0 is the radius of the Gaussian beam waist.

Finally, the linearly polarized field becomes:

$$E_y(x,y,z) = E_0 \sin(\frac{m\pi x}{a}) \frac{1}{\left[1+\left(\frac{\lambda z}{\pi {w_0}^2}\right)^2\right]^{1/4}} \exp\left\{\frac{-y^2}{{w_0}^2[1+(\lambda z/\pi {w_0}^2)]}\right\} \times$$

$$\times \exp\left\{-i\left[\left(1+\frac{1}{2}(\frac{m\pi}{ka})^2\right)kz + \frac{1}{2}\arg\tan(\frac{\lambda z}{\pi {w_0}^2}) + \frac{ky^2}{2R(z)}\right]\right\} \tag{A.15}$$

For higher order modes in the wider direction, we assume ψ in equation (A.3) in the form

$$\psi(y,z) = h(\frac{y}{w}) \exp\left\{-i\left[P + \frac{k}{2q}y^2\right]\right\}, \tag{A.16}$$

where w is a function of z. After inserting this into equation (A.5), we arrive at a

differential equation for h:

$$h'' + i2k(\frac{dw}{dz} - \frac{w}{q})yh' - w^2[i\frac{k}{q} + 2kP' + (\frac{m\pi}{a})^2]h = 0 \ . \qquad (A.17)$$

Now instead of requesting the square bracket term in the above equation to be zero as in the lowest order mode case, we require it to satisfy

$$[i\frac{k}{q} + 2kP' + (\frac{m\pi}{a})^2] = -\frac{4n}{w^2} \ , \qquad (A.18)$$

where n is an integer.

If we define w the same way as in the two-dimensional Gaussian beams:

$$w = w_0\sqrt{1+\left(\frac{z}{|q_0|}\right)^2} \qquad (A.19)$$

at the beam waist ($z = 0$) we have:

$$h'' - \frac{4y}{w_0}h' + 4n\,h = 0 \ . \qquad (A.20)$$

We now change the variable for h to $\sqrt{2}y/w$, and rename

$$h(\frac{y}{w}) \equiv g(\sqrt{2}\frac{y}{w}) \ . \qquad (A.21)$$

Thus the equation for g becomes:

$$g'' - 2\frac{\sqrt{2}y}{w_0}g' + 2n\,g = 0 \ . \qquad (A.22)$$

This is the differential equation for the n^{th} order Hermite polynomial. Thus the laser field at $z = 0$ becomes:

$$E_y(x,y,z) = E_0 \sin(\frac{m\pi x}{a}) H_n\left(\sqrt{2}\frac{y}{w_0}\right) \exp\left(\frac{-y^2}{{w_0}^2}\right). \qquad (A.23)$$

Now we see the high order modes in the wide dimension for the slab waveguide structure are still Hermite-Gaussian, as in the case of two-dimensional free-space laser resonators.

Appendix B. ln(R) for Lossy Waveguides

The intensity reflection coefficient R is given by:

$$R = r\,r^{*}, \tag{B.1}$$

where r is the electric field reflection coefficient given by the complex Fresnel equations. For TE-like modes, i.e., the E-vector perpendicular to the plane of incidence:

$$r = \frac{\cos\theta - \sqrt{n^2 - \sin^2\theta}}{\cos\theta + \sqrt{n^2 - \sin^2\theta}}, \tag{B.2}$$

where n is the complex refractive index and θ is the angle of incidence.

When $\frac{\cos\theta}{\sqrt{n^2 - \sin^2\theta}} \ll 1$, we can use $\ln(1+x) \simeq x$. So

$$\ln(R) = \ln(r) + \text{c.c.} \simeq -\frac{2\cos\theta}{\sqrt{n^2 - \sin^2\theta}} + \text{c.c.} = -4\cos\theta\ \mathrm{Re}\left[\frac{1}{\sqrt{n^2 - \sin^2\theta}}\right] \simeq$$

$$\simeq -\frac{2m\lambda}{a}\ \mathrm{Re}\left[\frac{1}{\sqrt{n^2 - 1}}\right]. \tag{B.3}$$

For TM-like modes, i.e., with the E-vector parallel to the plane of incidence,

$$r = \frac{n^2\cos\theta - \sqrt{n^2 - \sin^2\theta}}{n^2\cos\theta + \sqrt{n^2 - \sin^2\theta}} = -\frac{1 - \frac{n^2\cos\theta}{\sqrt{n^2 - \sin^2\theta}}}{1 + \frac{n^2\cos\theta}{\sqrt{n^2 - \sin^2\theta}}}. \tag{B.4}$$

Note that ln(R) can be written

$$\ln(R) = \ln(rr^*) = \ln[(-r)\ (-r^*)]\ . \tag{B.5}$$

As long as $\frac{n^2\cos\theta}{\sqrt{n^2-\sin^2\theta}} \ll 1$, then

$$\ln(R) = \ln\left[\frac{1-\frac{n^2\cos\theta}{\sqrt{n^2-\sin^2\theta}}}{1+\frac{n^2\cos\theta}{\sqrt{n^2-\sin^2\theta}}}\right] + \text{c.c.} = -2\cos\theta\frac{n^2}{\sqrt{n^2-\sin^2\theta}} + \text{c.c.}$$

$$= -4\cos\theta\ \mathrm{Re}\left[\frac{n^2}{\sqrt{n^2-\sin^2\theta}}\right]$$

$$= \frac{2m\lambda}{a}\ \mathrm{Re}\left[\frac{n^2}{\sqrt{n^2-\sin^2\theta}}\right]. \tag{B.6}$$

Appendix C. ln(R) for Lossy Waveguides with Lossy Coatings

The field reflection coefficient r for a lossy layer with complex refractive index n_2 and of thickness h on a lossy substrate of complex refractive index n_3 can be written as:

$$r = r_{12} + \frac{t_{12}t_{21}\, r_{23}\, e^{-i2\delta_2}}{1 + r_{12}\, r_{23}\, e^{-i2\delta_2}}, \tag{C.1}$$

where r_{ij} are reflection coefficients and t_{ij} are transmission coefficients of interface i-j; δ_2 is the phase shift through medium 2. These can be found in textbooks on optics, for example, reference 12. The reflection coefficient r includes loss when n_2 is complex through a complex δ_2:

$$\delta_2 = \frac{2\pi}{\lambda} h\sqrt{n_2^2 - \sin^2\theta}\,. \tag{C.2}$$

For TE-like modes:

$$\left.\begin{aligned} r_{12} &= \frac{\cos\theta - \sqrt{n_2^2 - \sin^2\theta}}{\cos\theta + \sqrt{n_2^2 - \sin^2\theta}} \\ r_{23} &= \frac{\sqrt{n_2^2 - \sin^2\theta} - \sqrt{n_3^2 - \sin^2\theta}}{\sqrt{n_2^2 - \sin^2\theta} + \sqrt{n_3^2 - \sin^2\theta}} \\ t_{12}t_{21} &= \frac{4\cos\theta\sqrt{n_2^2 - \sin^2\theta}}{\left(\cos\theta + \sqrt{n_2^2 - \sin^2\theta}\right)^2} \end{aligned}\right\}. \tag{C.3}$$

For TM-like modes:

$$\left.\begin{aligned} r_{12} &= \frac{n_2^{\,2}\cos\theta - \sqrt{n_2^{\,2} - \sin^2\theta}}{n_2^{\,2}\cos\theta + \sqrt{n_2^{\,2} - \sin^2\theta}} \\ r_{23} &= \frac{n_3^{\,2}\sqrt{n_2^{\,2} - \sin^2\theta} - n_2^{\,2}\sqrt{n_3^{\,2} - \sin^2\theta}}{n_3^{\,2}\sqrt{n_2^{\,2} - \sin^2\theta} + n_2^{\,2}\sqrt{n_3^{\,2} - \sin^2\theta}} \\ t_{12}t_{21} &= \frac{4\, n_2^{\,2}\cos\theta\sqrt{n_2^{\,2} - \sin^2\theta}}{\left(n_2^{\,2}\cos\theta + \sqrt{n_2^{\,2} - \sin^2\theta}\right)^2} \end{aligned}\right\} . \qquad \text{(C.4)}$$

Substituting r_{12}, r_{23}, $t_{12}t_{21}$ in equations (C.3) and (C.4) into (C.1), we should obtain the field reflection coefficients. Then using (B.5):

$$\ln(R) = \ln(-r) + \ln(-r^*) \, , \qquad \text{(C.5)}$$

we can plot $-\ln(R)$ as given in Figures 5 to 7.

REFERENCES

1. D.R. Hall and H.J. Baker, "Area Scaling Boosts CO_2-Laser Performance," Laser Focus World, Vol. 25, No. 10, pp. 77–80, October 1989.

2. J. Salzman, T. Venkatesan, R. Lang, M. Mittelstein and A. Yariv, "Unstable Resonator Cavity Semiconductor Lasers," Appl. Phys. Lett. Vol. 46, No. 3, pp. 218–220, February 1985.

3. A. Yariv and P. Yeh, Optical Waves in Crystals, John Wiley and Sons, 1984.

4. Marcatili and Schmeltzer, "Hollow Metallic and Dielectric Waveguides for Long Distance Optical Transmission and Lasers," The Bell System Technical Journal, pp. 1783-1809, July 1964.

5. E.D. Palik, editor, Handbook of Optical Constants of Solid State Materials, Academic Press, 1985.

6. C.A. Worrel, "Infrared Optical Constants for CO_2 laser waveguide Materials," Journal of Material Science, Vol. 21, pp. 781–787, March 1986.

7. H.G. Häfele, "Das Infrarostspectrum des Rubins," Z. Naturforsch. A, Vol. 18, pp. 331–335, March 1963.

8. K.D. Laakman and W.H. Steier, "Waveguides: Characteristic Modes of Hollow Rectangular Dielectric Waveguides," Applied Optics, 15(5), May 1976; *and* K.D. Laakman, "Hollow Dielectric Waveguides: errata," Applied Optics 15(9), September 1976.

9. B. Adam and F. Kneubühl, "Transversely Excited 337 μm HCN Waveguide Laser," Applied Physics, Vol. 8, pp. 281–291, December 1975.

10. R.L. Abrams and W.B. Bridges, "Characteristics of Sealed-off Waveguide CO_2 Lasers," IEEE Journal of Quantum Electronics, Vol. QE-9(9), pp. 940–946, September 1973.

11. H. Kolgelnik and T. Li, "Laser beams and Resonators," Proceedings IEEE, Vol. 54, pp. 1312–1329, 1966.

12. M. Born and E. Wolf, Principles of Optics, 3rd ed., Pergman Press, New York, 1965.

CHAPTER 5. A NEW STRUCTURE — THE GROOVE-COUPLED STRIP WAVEGUIDE ARRAY

§5.1 Introduction

In Chapter 2, we found that the spatial loss distribution within a laser cavity played an important role in determining the transverse mode of oscillation. Numerical calculations were carried out for two-element arrays of both one-dimensional and two-dimensional models. The results of the calculation suggested that the smaller the loss in the inter-element region (a small β, see Table 1 in §2.4), the more likely the in-phase coupled mode will oscillate, and *vice versa.*

In Chapter 3 we found that the wall-slot coupled array favored the out-of-phase coupled mode over the in-phase coupled mode. The reason for this was found to be the high loss in the inter-element regions. If there were a way of coupling the waveguides without going through such a lossy region, we would be more likely to have an in-phase coupled array mode. Yet some kind of separating region must exist between the elements to preserve the individual channels, otherwise we would simply have a slab waveguide, as described in Chapter 4.

In Chapter 4, we found that the mode of a slab waveguide is a combination of a sinusoid from the waveguiding dimension and a free-space Gaussian mode in the direction where there is no guiding. A wide slab will inevitably yield high-order Gaussian mode oscillation, which is undesirable in most laser applications, while a narrow slab can provide only limited laser power.

Combining the knowledge we gained from earlier experiments, we proposed[1] an array structure that has less loss in the inter-element region and hence would favor the in-phase coupled mode. Depicted in Figure 1, it is named the groove coupled strip waveguide array, because it has several strip waveguide laser channels positioned side by side, separated by grooves. A strip waveguide can be

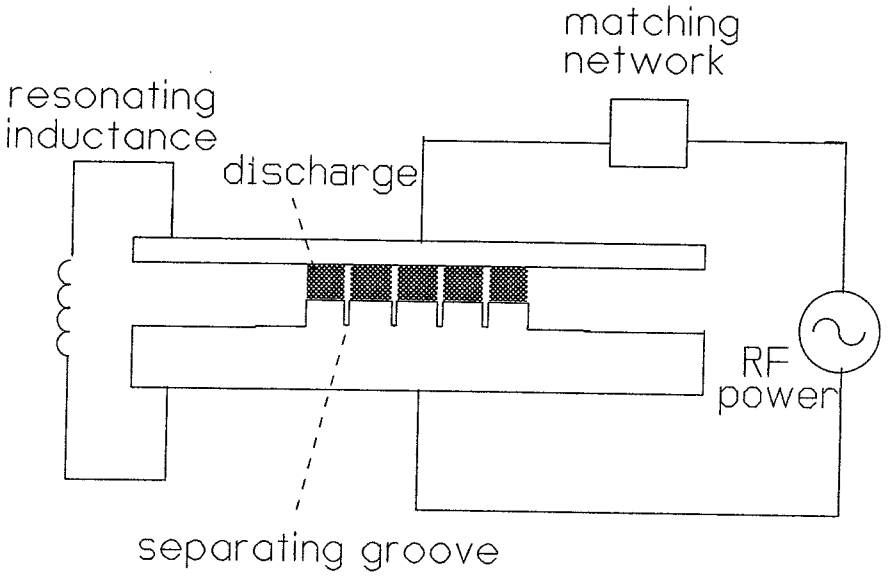

(a)

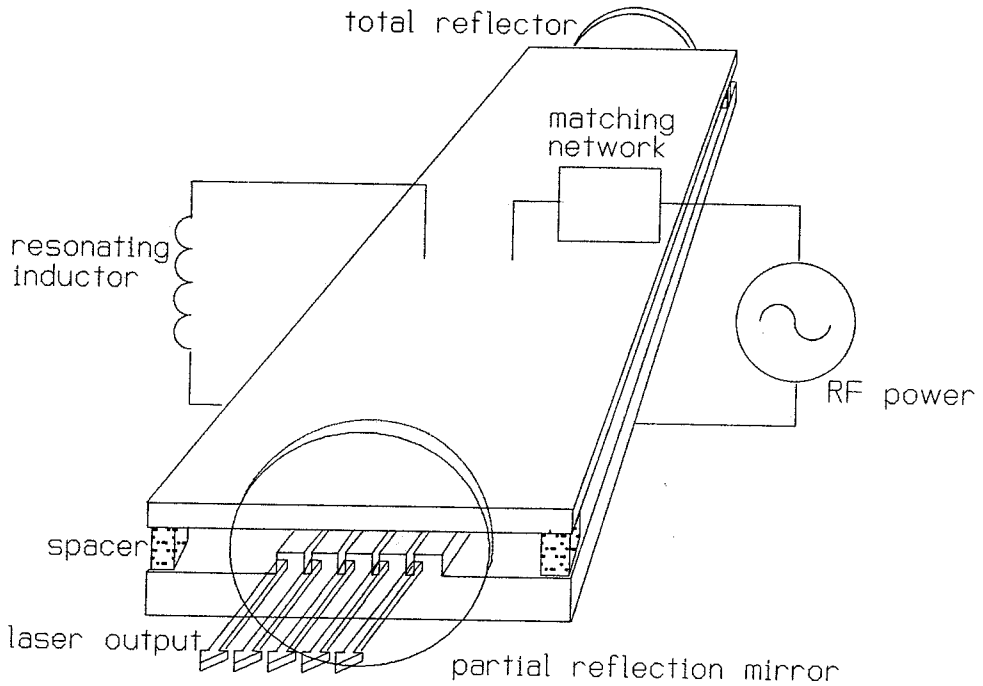

(b)

Figure 1. Schematics showing the new groove coupled strip waveguide laser array: (a) Transverse cross section; (b) three-dimensional illustration.

considered as a narrow slab waveguide, in which the gain width supports only the fundamental Gaussian mode. The high order Gaussian modes are not only less favored by the narrow gain, but also suppressed by the scattering at the straight edge of the waveguide element. (Recall that the caustic curves of the Gaussian modes in the y-z plane are hyperbolas, not straight lines, and thus the locus of Gaussian zeros in the y-z plane cannot match the straight grooves. Also, the grooves are equally spaced, while the Gaussian zeros are not.) When these strips are put together as in Figure 1, they can couple with their Gaussian tails leaking into each other's channels and suffer much less loss in the inter-element region, compared to the wall-slot coupled arrays, because there is no lossy material in this region. Another advantage of this array structure is that it can be made completely of flat pieces except for the spacers shown in Figure 1. This yields considerable savings by replacing expensive ceramic material and ceramic precision grinding with economical flat metal material (we used aluminum) and simple milled slots, whose surface finish is unimportant. We tested arrays of two, three, and five elements and obtained in-phase coupling in all of them. A U.S. patent was issued for this structure[2].

§5.2 RF Field Distribution for a Single Strip and Mode Coupling Between the Strip Waveguides

A finite-difference calculation was carried out to simulate the RF driving field with a static electric field and to yield the electric field distribution in the all-metal slab (or strip) waveguide. Solutions were obtained for different electrode gap sizes and groove depths. Because of the symmetry of the structure, only half of it is involved in the calculation. Figure 2 is the equipotential line plot for a structure with the ratio of *strip width: groove width: waveguide spacing* being 5:1:1, similar to the actual structure to be described later in this chapter. The electric field lines are perpendicular to the equipotential lines, and the field strength is higher where the equipotential lines are closer together. We can see that the electric field within the strip away from the edges is perpendicular to the waveguide/electrode surfaces and is quite uniform; and at the edge of the strip the field starts to bend outwards and there is a higher field strength around the corner. This is typical for the static electric field.

The fact that the field is strong at the corner and bending outward suggests that the discharge, and thus the laser gain, will extend beyond the width of the strip. This has been confirmed by our observation of the discharge and by Hall et al.[3] in their photograph of the discharge of the slab geometry. Thus the Gaussian distribution of the laser field also extends considerably outside the strip geometry. This extended Gaussian distribution increases the coupling between the channels in the array over what is implied by the geometric shape of the channels alone. In an index-guided waveguide, the evanescent field distribution outside the core varies exponentially, e^{-ay}. When two or more of these waveguides are put together, this exponential portion of their field distributions overlap with each other. This is the source of coupling. If the Gaussian field of our structure does

not extend considerably into the inter-element region, the coupling between the elements would be very weak because the Gaussian tail fall off is much faster than the exponential fall off, e^{-by^2}. From Fig.2, we see that there may still be some small gain in the inter-element regions above the slots because the presence of the non-zero RF driving field. This would help enhance the preference for the in-phase coupled mode over the out-of-phase coupled mode, as long as it is not enough to encourage the high-order Gaussian modes suppressed by the groove loss.

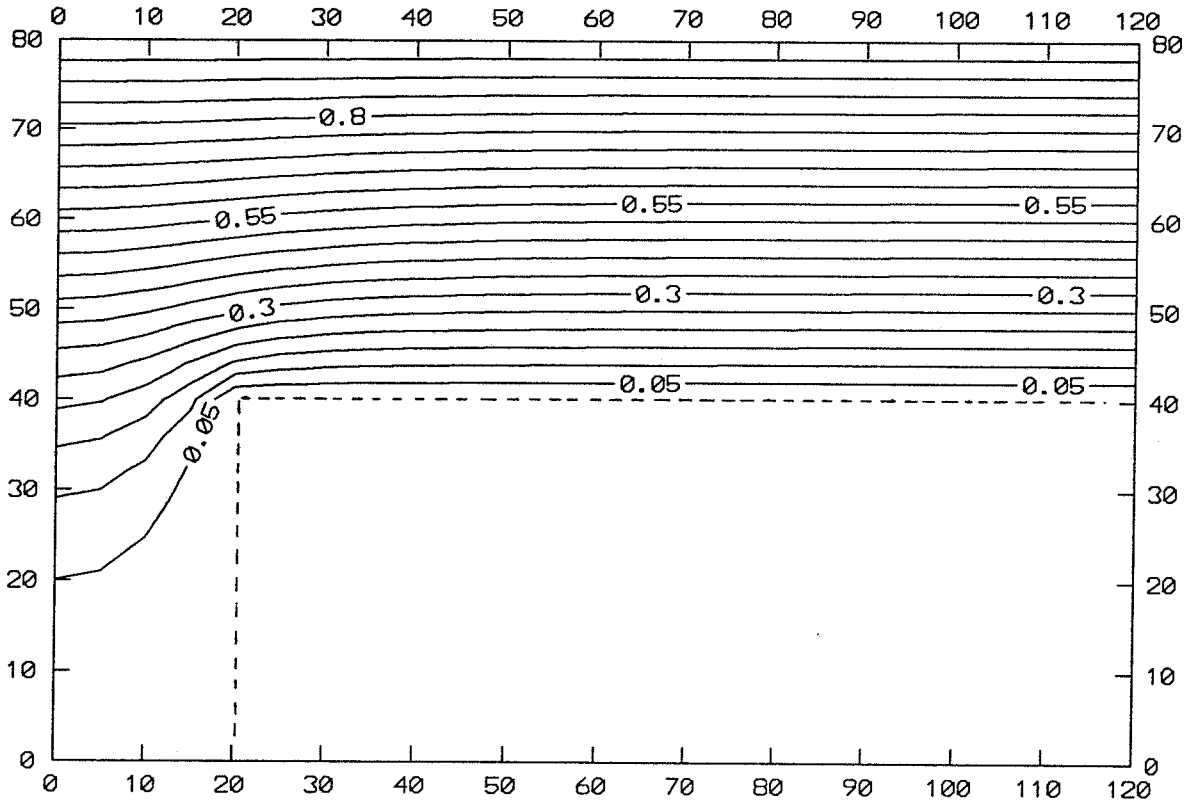

Figure 2. The equipotential lines in the laser waveguide and the groove regions for the RF excitation field. It is clearly seen that the field is strongest around the corner of the strip. Because of symmetry, only half of the wide-direction is plotted. The ratio of *strip width: groove width: waveguide spacing* is 5:1:1.

§5.3 Coupling Between the Cosine-Gaussian Modes in Active Media

In a regular index-guided waveguide, the modes are well defined by the waveguide structure, which has a given distribution of the index of refraction. When two waveguides of this type are parallel and are brought into close proximity, it is inevitable that the polarization of one waveguide will perturb that of the other, and coupling occurs between two or more similarly-polarized guided modes as a result of this perturbation. Yariv[4] gave the equations that describe this coupled set of m modes:

$$\sum_{m} -i\beta_m \frac{dA_m(z)}{dz} \mathcal{E}_y^m e^{i(\omega t - \beta_m z)} + \text{c.c.} = \mu \frac{\partial^2}{\partial t^2}[P_{pert}(\mathbf{r},t)]_y \,, \qquad (1)$$

where $A_m(z)$ is the complex amplitude of the y-polarized m-th modal field $\mathcal{E}_y^m$, and P_{pert} is the perturbation polarization. From (1) we can see that A_m becomes a function of z only because of the presence of the perturbation in polarization, P_{pert}. If P_{pert} were zero, then A_m becomes a constant and we are back to the uncoupled modes. A host of devices such as directional couplers have been built on mode coupling of this kind.

For free-space Gaussian modes, no guiding is required for them to exist and propagate. Nothing happens when two Gaussian beams are brought close to each other in free space, which can have no polarization, P_{pert}. However, the situation is quite different in active media, where the existence of saturable gain distorts the transverse shape of a Gaussian mode, while not providing actual guiding, as discussed by Bridges[5]. Thus if two Gaussian modes are brought close to each other, together with the gain distributions that support them, the gain distribution for one mode will be perturbed by the existence of the gain distribution of the other mode, and vice versa, making P_{pert} in equation (1) non-

zero. Thus coupling between two Gaussian modes can occur. This happens only in polarizable media, in this case, the laser gain medium. The coupling of two channels through an active gain medium is different from regular waveguide mode coupling, in which the modes in two adjacent passive channels are coupled. Also, the Gaussian beam does not have a straight envelope in its propagation direction, and thus the coupling happens mostly in the sections of the beams where they have larger cross sections.

Because the one-dimensional Gaussian mode in our array does not differ from the regular two-dimensional Gaussian mode in its dimension, there is a possibility that two-dimensional free-space Gaussian modes from two or more non-waveguide lasers could also be coupled together, as long as the gain region of each laser extends sufficiently in the direction of coupling, but not so much as to make the gain region a smooth continuum. The utilization of this Gaussian mode coupling could possibly lead to a more powerful combination of lasers. It can also be applied to laser gain media other than CO_2.

In Chapter 4, we observed that the modes for a single channel slab laser are the free-space, Hermite-Gaussian modes in the transverse direction parallel to the waveguide plates. However, if the slab is very narrow, say, a strip of width comparable to the waveguide spacing, and gain medium is equally narrow, then the Gaussian mode can be distorted so that it is more like the gain-guided mode described by Streifer, et al.[6]

If the strip is narrow enough to support only the fundamental Gaussian mode, yet wide enough so that a considerable part of the Gaussian caustic curve in the y-z plane would not feel the boundary of the gain, then we can still regard the mode being free-space Gaussian. On the other hand, if the waveguide strip and the gain medium are the same size as or even narrower than the beam waist

of the Gaussian caustic curve, then the part of the Gaussian beam that exceeds the strip and gain region would be scattered by the gain-loss boundary; the stable modal distribution in such a laser cavity would have a profile in the x-y plane that does not vary with z, unlike the free-space Gaussian mode. Even in this situation, the modal intensity profile in the y-direction can still be Gaussian, as suggested by Streifer, et al.[6] Thus when a number of parallel, gain-guided strip waveguides are placed close together, the perturbation to the gain distribution is of the same nature as the aforementioned Gaussian mode array. This array should be called a gain-guided array, as in semiconductor lasers.

There is hardly a clear boundary between the coupled free-space Gaussian mode array and the gain-guided array. In our experiments, to be described in later sections, we used several arrays of strip waveguides, where the strip widths were from 3 mm to 6 mm, all supporting a fundamental mode for each strip. We can say that the 3 mm strip array is closer to the gain guided array and the 6 mm strip array is closer to the coupled Gaussian mode array.

The index of refraction of the active medium is related to the gain through the Kramers-Kronig relationship[4], as well as the change of gas density in this region. The former is weak in the low gain, relatively high-pressure waveguide CO_2 lasers[7], and the latter, although stronger than the former, is calculated from Colley et al.[8] to introduce a correction of about 10^{-5} to the index of refraction. Thus the real-index guiding is negligible and both effects can be ignored.

§5.4 Experimental Results

Stable, single in-phase mode operation was obtained in two, three and five-element arrays. The setup for the measurements is shown in Figure 3, where the laser power is divided into two beams with a grating. One of the beams is either sent into the CO_2 laser spectrum analyzer or dumped. The other beam goes through a variable focal length, two-lens system to be imaged. By adjusting the position and the focal length of the two-lens system, either the far field or the near field of the laser beam can be imaged at the plane of the HgCdTe fast detector ($f_{max} \simeq 200$ MHz). And by scanning the beam across the small detector area (1 mm^2), we could see the intensity distribution of the beam at the oscilloscope. The output from the fast detector is also sent to an RF spectrum analyzer so that the beat notes will appear if there is more than one mode. The far-field intensity distributions of 2, 3 and 5-channel arrays are given in Figure 4a. The near-field distribution of the five-element array is shown in Figure 4c. For all three arrays, we can adjust the cavity alignment to obtain high power output, a symmetrical intensity distribution, and no beat note evident on the spectrum analyzer. The polarization of the laser was TE-like, i.e., the electric field was parallel to the surface of the waveguide. From these observations, we can conclude that this was single, in-phase coupled mode operation.

The gradual evolution of the intensity distribution from the near field to the far field was recorded as burn-patterns on a piece of Lucite, as shown in Figure 5. A telescope was formed from lenses f_1 and f_2 to provide a focal spot 15″ from f_2, and a series of burn patterns were taken at distances 6″ to 15″ from lens f_2 at 1″ intervals.

To further investigate the robustness of the in-phase coupled mode, we performed the additional-loss test on the two-strip array shown in Figure 6. Up to

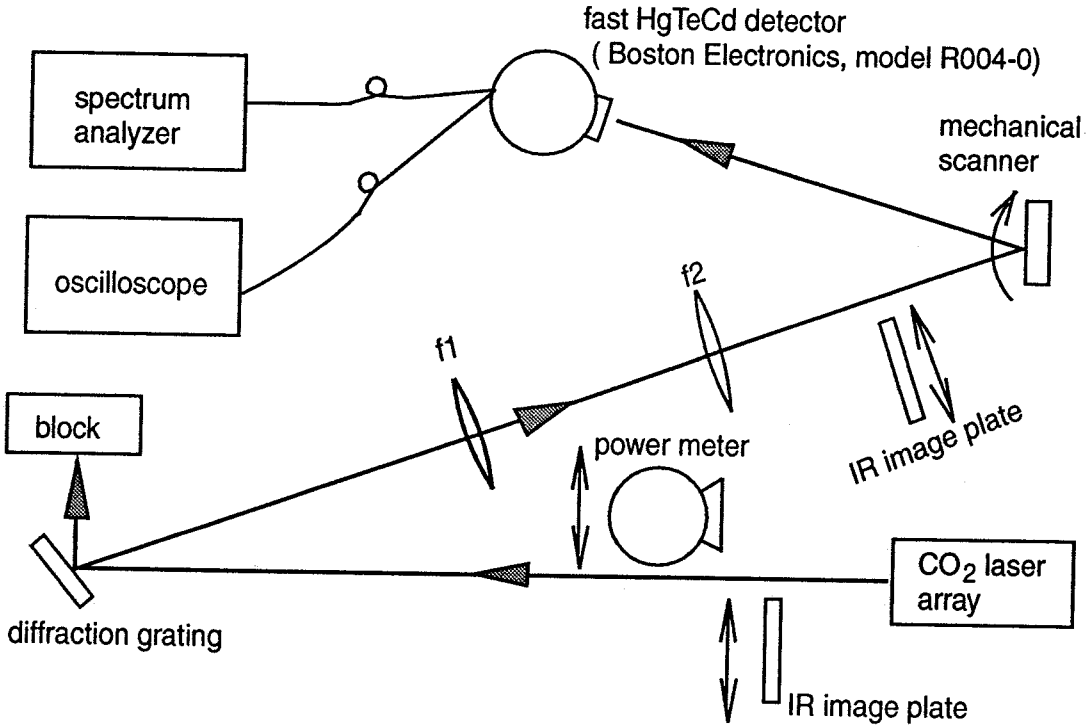

Figure 3. Measurement setup for the modal intensity scans of 2, 3 and 5-channel groove-coupled strip laser arrays.

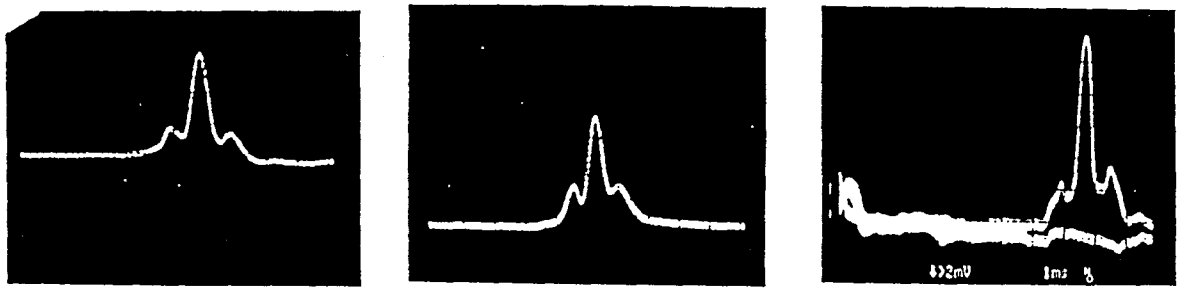

2-channel array 3-channel array 5-channel array

(a)

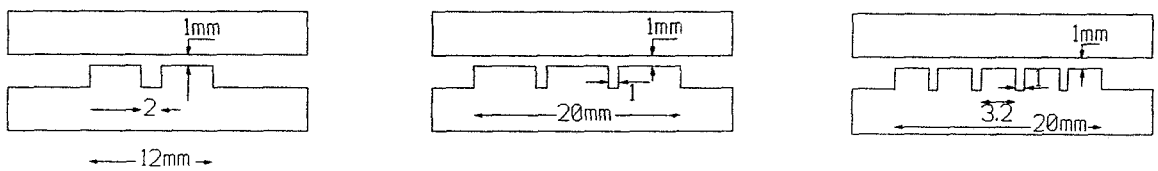

(b)

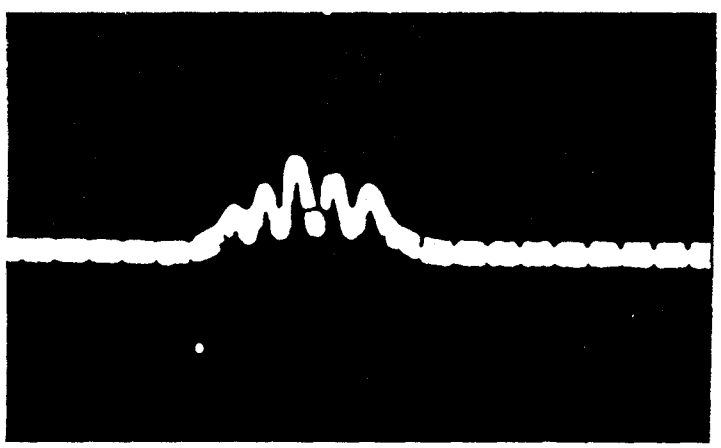

(c)

Figure 4. (a) Measured far-field intensity distributions for three arrays, (b) the sizes of the arrays, and (c) measured near-field intensity distribution for the five-channel array.

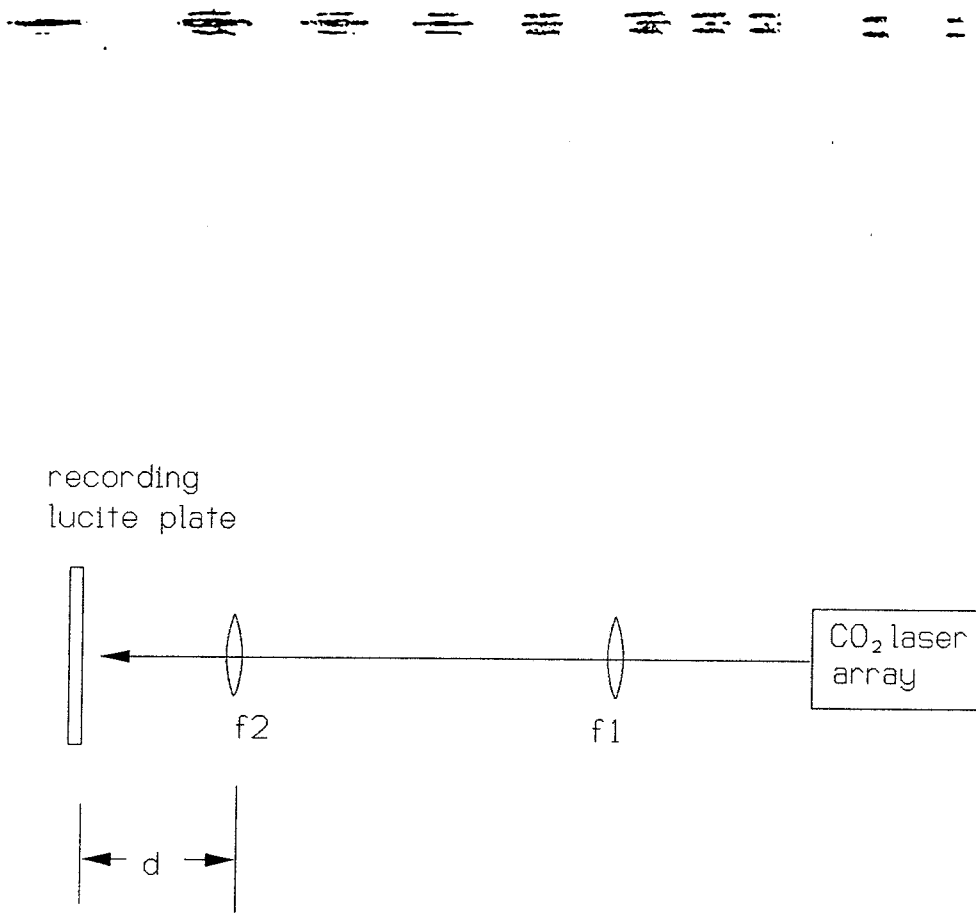

Figure 5. The evolution of the intensity distribution and the measurement setup. The mode patterns were measured 1″ apart in the direction of laser propagation by varying d.

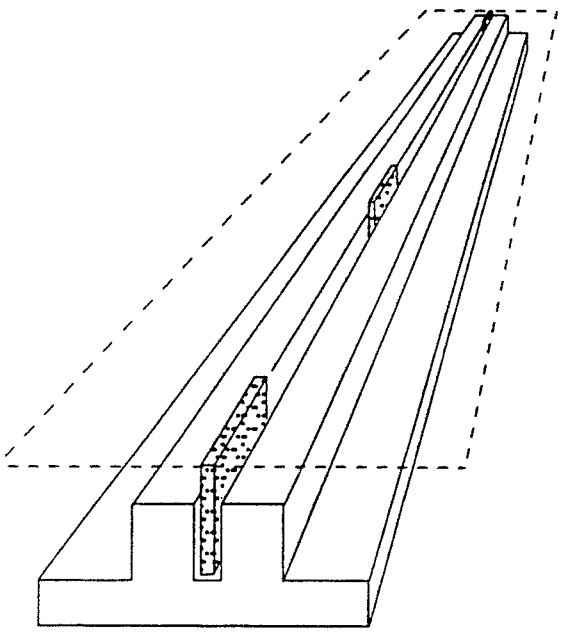

Figure 6. The groove coupled strip array with intentional loss introduced in the inter-element region. After the three pieces of glass were added one at a time, the in-phase coupled supermode still oscillated stably .

three small pieces of glass could be positioned in the inter-element region of the array with the in-phase coupled mode still dominant in oscillation. This result suggests that the in-phase coupled mode in the groove-coupled strip array is robust. It also contrasts with the similar test for the wall-slot coupled two bore array described in §3.3 (Figure 10), in which a single small piece of glass in the inter-element region completely eliminated the in-phase coupled mode.

As we observed in §5.2, at the edge of a strip laser, the RF driving field bends outward. If the groove between the elements is too narrow, we can imagine that the field in this region will be almost as strong as in between the top electrodes and the strips. Then the discharge will "ignore" the groove and the laser gain will be more or less uniform across the grooves, and thus uniform across the array. This will bring back the high order Gaussian mode. For example, Figure 7a shows experimental results indicating a mode with ***three*** zeros originating from a structure with ***two*** 0.5 mm wide grooves. This pattern was the same in both the near ***and*** far fields, showing that the adjacent lobes are 180° out of phase and the pattern is Hermite-Gaussian. However, when the two grooves were made slightly larger, e.g., 1.0 mm, the three laser channels were well defined and the near field changed to Figure 7b, where the number of zeros is the same as the number of grooves cut. The far-field pattern (Figure 4a) and beat spectrum confirm that this is indeed a single, in-phase coupled mode.

Our next test involved the laser power output comparison of the coupled-strip array operating in the in-phase coupled mode and a slab laser that operates on a third-order Gaussian mode. Both wall pairs were made of aluminum and had a surface finish of about 2 μm, from a milling machine. The power v.s. pressure curves are plotted in Figure 8. It can be seen that the array structure greatly improved the optical quality of the laser with a modest cost in power: the in-phase

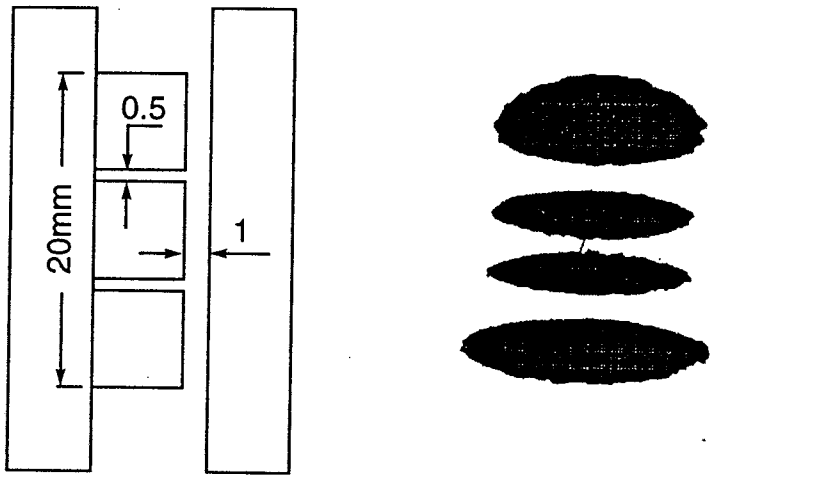

a) narrow groove

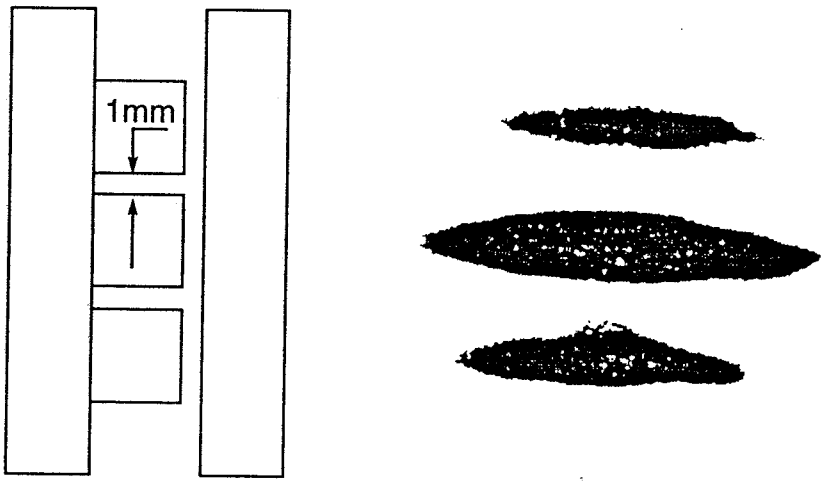

b) wider groove

Figure 7. The effect of groove width in a three-strip array: (a) narrow grooves being ignored by the discharge and the near-field intensity distribution is that of a third-order consine-Gausssian mode. Three nulls do not match two grooves. (b) Wider grooves yield a distribution of coupled mode: lowest-order consine-Gaussian mode in the strips coupled together. Two nulls match the number of gooves.

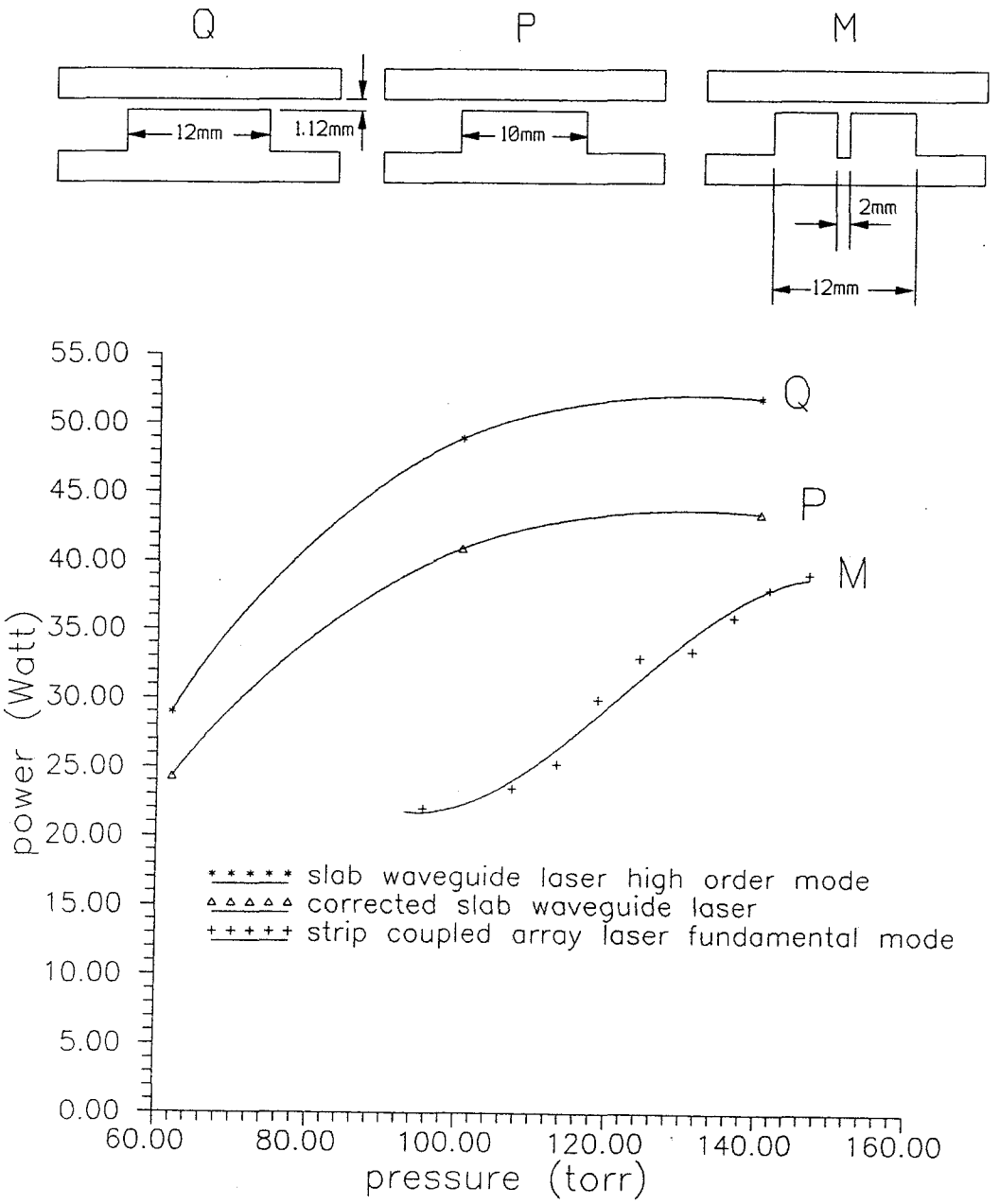

Figure 8. Output power comparison between the strip array laser and slab laser. Curve M is for the array. Curve Q is for the slab with the same overall volume as the strip array. Curve P is for a slab reduced in volume so that it has the same total discharge surface area as that of the array. The reduction in power from Q to P is assumed to be proportional to the reduction in area. The maximum point of M is 73% of Q and 87% of P.

array mode had 87% of the power of a higher-order mode from a slab laser of the same discharge volume (i.e., corrected by subtracting the volume over the groove). For the in-phase coupled mode, the power in the center, near-diffraction limited main lobe of the far-field distribution was measured to be between 60–70% of the total power. Thus, these two factors combine to place 52–61% of the total high-order Hermite-Gaussian mode power into the central lobe of the in-phase coupled mode. As can be seen from Figure 4b, the groove between the two elements in this array is 2 mm. If it were reduced to 1 mm, as in the cases of three and five-strip arrays, we could expect an even higher power concentration in the center main lobe.

The physics of coupling in our groove-coupled strip array is quite different from that of the anti-guiding array of semiconductor lasers, in which the transverse structure has to be at resonance with the guided wavelength in order to arrange the optical field in all active channels to oscillate at the same phase[9]. In our experiments, as can be seen from Figure 4b, we used quite different channel widths for different arrays, e.g., 3 mm, 5 mm, and 6 mm; and we used groove widths from 1.0 mm to 2.0 mm. They could all be coupled in-phase; no resonant-condition behavior depending on the width of strips and grooves was observed.

REFERENCES

1. Y. Zhang and W.B. Bridges,"Transverse Mode Control and Switching in Gas Laser Arrays," Submitted to IEEE Journal of Quantum Electronics, November 1992.

2. Y. Zhang, "In Phase Coupled Strip Waveguide CO_2 Laser," U.S. Patent 5,177,748, January 5, 1993.

3. D.R. Hall and H.J. Baker, "Area Scaling Boosts CO_2-Laser Performance," Laser Focus World, Vol. 25, No. 10, pp. 77–80, October 1989.

4 A. Yariv, Quantum Electronics, 3rd edition, John Wiley & Sons, 1989.

5 W.B. Bridges, "Gaussian Beam Distortion Caused by Saturable Gain or Loss," IEEE Journal of Quantum Electronics, Vol. QE-4, No. 11, pp. 820–827, November, 1968.

6. W. Streifer, D.R. Scifres and R.D. Burnham "Analysis of Gain-Induced Waveguiding in Strip Geometry Diode Lasers," IEEE Journal of Quantum Electronis, Vol. QE-14, No. 6, pp. 418–427, June 1978.

7. R.C. Sharp, "Chirp in Pulsed, RF-Excited CO_2 Waveguide Lasers," J. Appl. Phys., Vol. 64, No. 2, pp. 544–553, July 15, 1988.

8. A.D. Colley, K.M. Abramski, H.J. Baker and D.R. Hall, "Discharge-Induced Frequency Modulation of RF Excited CO_2 Waveguide Lasers," IEEE Journal of Quantum Electronics, Vol. 27, No. 7, pp. 1939–1945, July 1991.

9. D. Botez, L.J. Mawst, G.L. Peterson and T.J. Roth, "Phase-Locked Arrays of Antiguides: Modal Content and Distrimination," IEEE Journal of Quantum Electronics, Vol. 26, No. 3, pp. 482–495, March 1990.

CHAPTER 6. MICROWAVE EXCITED CO_2 WAVEGUIDE LASER

§6.1 Introduction

Our demonstration of a bare metal slab waveguide laser as described in Chapter 4 lead us to consider how we might make an ***all metal*** waveguide laser of simple construction and excited by an inexpensive power source. Figure 1 shows the evolution of our reasoning. Figure 1a shows the transverse cross section of the waveguide, matching inductance and the vacuum structure used in our slab laser. The two metal slabs forming the optical waveguide are separated by insulating spacers and joined by inductors to form a resonant LC circuit at 146 MHz. The entire assembly is suspended inside an external metal vacuum chamber. The RF excitation is brought into the vacuum chamber via a vacuum-tight coaxial feedthrough insulator. All waveguide lasers demonstrated to date that we know of utilize similar elements. Since the two metal slabs must have an RF potential difference between them, at least on of them must be insulated from the metal vacuum chamber walls.

If the resonating inductance could be made in the form of a vacuum-tight connecting metal wall, however, as shown in Figure 1b, there would be no need for the insulating spacer, since the RF potential difference could be supported across this inductance. Thus the electrodes/optical waveguide plus this inductive wall could form the outer vacuum envelope of the laser. Of course, such a wall would have much lower inductance L than the coils or straps used in our previous lasers, so that the resonant frequency ω_r that is given by

$$\omega_r = \frac{1}{\sqrt{LC}} \qquad (1)$$

would be increased greatly for the same inter-electrode capacitance C. We

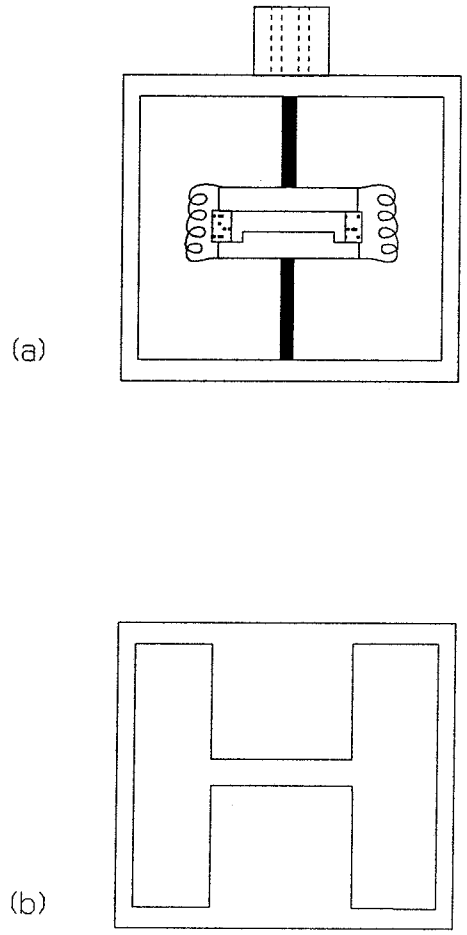

Figure 1. (a) Cross section of LC resonant slab laser inside a vacuum chamber, similar to the test bed laser used in this project. One side is grounded and the other is fed with RF at 146 MHz through a hermetically sealed coaxial fitting. (b) Cross section of a double ridge-loaded waveguide, with dimensions just above cutoff frequency at 2450 MHz. RF feeding can come from a connected waveguide.

normally think of a power source becoming more expensive as its frequency increases. However, there is an "anomalously low" cost associated with microwave power at 2.45 GHz, the frequency used by commercial microwave ovens. Thus we were motivated to consider what dimensions would be suitable for this frequency.

There have been several reports of microwave excited CO_2 lasers[1,2]. However, to our knowledge, the structures used provided waveguiding only for the microwave power; none of them used a structure that provided waveguiding for both the microwave excitation and the optical wave.

The structure in Figure 1b is referred to in the microwave literature as a double ridge-loaded waveguide, and is often used to decrease the transverse dimensions of a standard metal waveguide. As we propose to use it, the ridge surfaces form the optical waveguide and also concentrate the RF pump power in the guide. Strong electric field concentrations occur between the opposing surfaces of the ridges, so that this structure is not often used with high power microwave systems, since an RF discharge would be inclined to break down in this field-concentration region. However, that is just what we desire to have happen here: We want to form a discharge primarily between the ridges to form the active region of our laser. The discharge should concentrate here if we adjust the ridge spacing and the gas pressure to favor a Paschen minimum in that region. There may be a frequency dependence for the Paschen minimum constant, but we will have to determine this by experiment. We start with the gas pressure and spacing in the laser operating range for excitation at 146 MHz. All the above considerations apply to a ***single*** ridge waveguide, which we elected to use for simpler machining.

The other dimensions of the ridge waveguide are not arbitrary. To make

the discharge uniform in the laser length, about 38 cm, the waveguide needs to operate near cutoff, so the guided wavelength is (ideally) longer than the laser. The free space wavelength at 2.45 GHz is 12.25 cm, too short compared to the laser length. Thus, to make a long laser, the transverse guide dimensions need to be adjusted to near cutoff, but just a little larger. This design will assure strong, uniform fields to help initiate the discharge.

Of course, the calculations for the cutoff conditions only apply to the ridge waveguide ***before*** the discharge begins. Once the discharge strikes, the loading will drastically alter the conditions in the waveguide. The high electron density in the discharge, about 10^{11} cm^{-3}, yields a plasma frequency of about 9 GHz, which is above the 2.45 GHz power source. Thus, no propagation could occur if this were a collisionless or lossless plasma. However, this plasma is also collisional, with a collision frequency of 740 GHz, and thus is quite lossy. In fact, also these same conditions were in effect with the 146 MHz excitation used previously. The question did not arise since the physical dimensions of the laser suggested a lumped-element viewpoint. In the 146 MHz experiments, the discharge looked like an equivalent resistance of around 100 ohms across the LC circuit. Hall et al.[3] also concluded that the RF discharge was basically resistive. There are not many experiments published on microwave-excited laser discharges to turn to. Mendelsohn et al.[4] described a microwave pumped XeCl* excimer laser that exhibited "insignificant" reflection once the discharge was struck. However, the conditions in such a laser may not be readily scalable to a CO_2 laser.

What the discharge will look like at 2.45 GHz is not easily calculable, so we chose to proceed experimentally, with the design for operation at cutoff prior to the discharge, and then determine the proper matching elements experimentally once the discharge began.

§6.2 Ridge Waveguide Theory

There is no exact electromagnetic field solution for single-ridge waveguides shown in Figure 2. Various approximate solutions have been published by Ramo and Whinnery[5], Cohn[6], and Chen[7]. We chose to use the method given by Cohn[6], which treats the guide as a *propagating structure in the transverse direction.* The condition for cutoff of the longitudinal guide is when this transverse propagating system is an integral number of its guide wavelengths long and there is no longitudinal propagation, that is, when it is in resonance. Cohn's transverse resonance model treats the ridge region as one parallel plate transmission line and the "inductor loop" as another, shorted parallel-plate line. The step discontinuity where these two lines meet is treated by adding a lumped "discontinuity capacitance" to the transmission system, as calculated by Whinnery and Jamieson[8]. The dimensions of the transverse cross section are then varied to obtain the resonant condition. According to Cohn[6], for the single ridge waveguide shown in Figure 2, the dimensions b_1 and b_2 are related by the following equation:

$$\frac{b_1}{b_2} = \frac{\cot\theta_1 - B_c/Y_{01}}{\tan\theta_2} , \tag{2}$$

where B_c is the admittance due to the discontinuity capacitance, Y_{01} is the quasi-static admittance of a parallel-plane waveguide with height b_1. B_2 can be computed from Whinnery and Jamieson's paper[8]. The definitions for the θ's are:

$$\theta_2 \equiv \frac{2\pi}{\lambda_c}\left(\frac{a_2}{2}\right) , \qquad \theta_1 \equiv \frac{2\pi}{\lambda_c}\left(\frac{a_1 - a_2}{2}\right) , \tag{3}$$

where λ_c is the free space wavelength at the cutoff frequency.

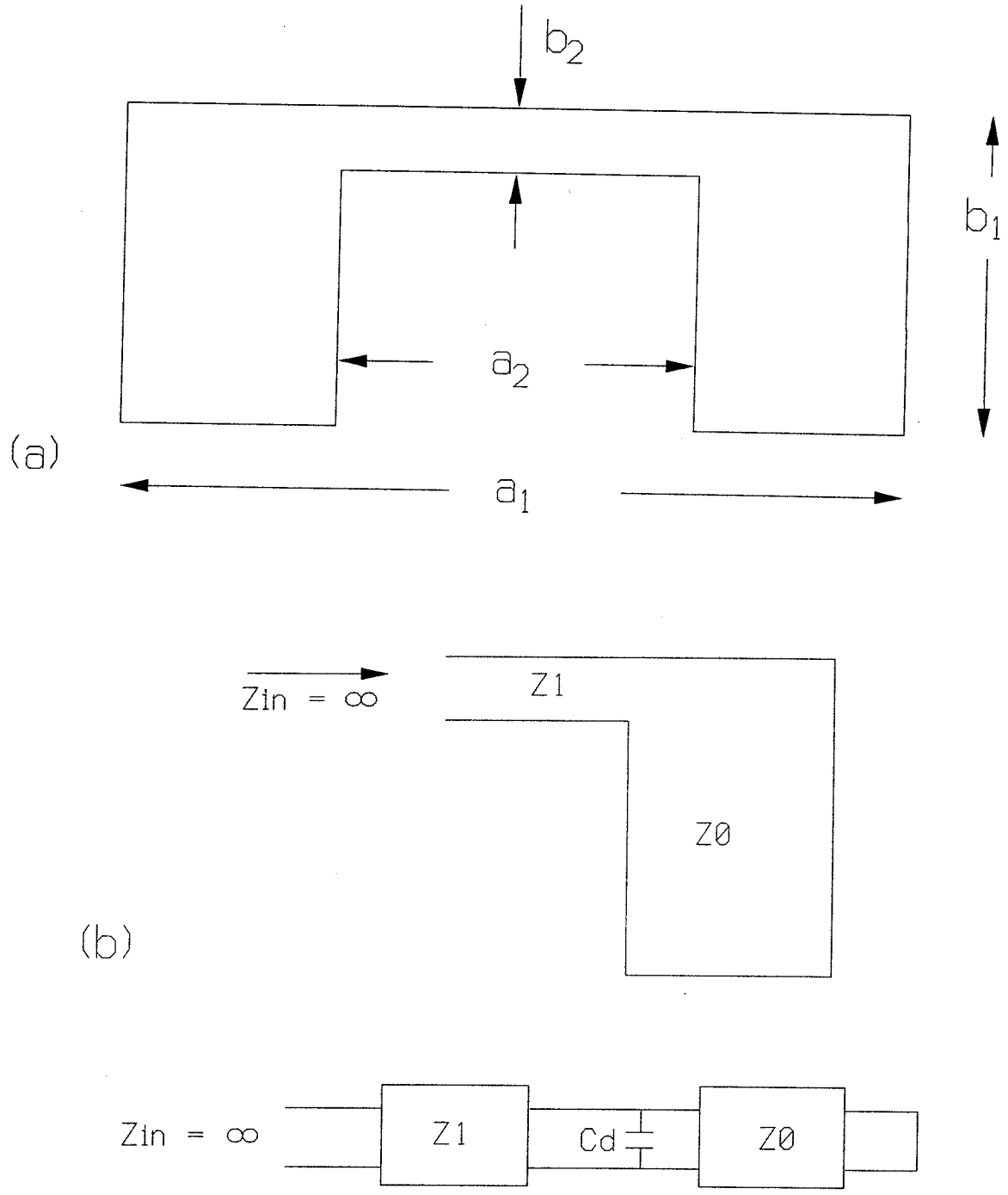

Figure 2. (a) Single ridge waveguide and (b) Its equivalent transmission line circuit for the lowest order mode.

We intended to use off-the-shelf waveguide metal stock as the enclosure of our ridge waveguide, so that we could fabricate a test vehicle without an undue amount of machining. Thus the two numbers a_1 and b_1 are fixed by waveguide standards. Because we planned to use an oven magnetron at 2.45 GHz, λ_c is fixed, too. The remaining variables are then the sizes for the ridge, a_2 and b_2.

Using equation (2), we computed a set of curves showing the relationship between a_2 and b_2 with frequency as a parameter around 2.45 GHz for the single ridge waveguide, as given in Figure 3. We find that we can make a reasonable single ridge waveguide, just cutoff at 2.45 GHz, with a gap spacing of 2.8 mm and a ridge width of 15 mm, and that further fits the overall rectangular dimension of a standard copper microwave waveguide, WR-137. Or we can make a ridge 10 mm wide with a narrower gap, 2.4 mm. WR-137 guide is cutoff at 4.3 GHz with the ridge absent. Thus, to obtain "short circuit" sections at the ends of the waveguide to confine the fields, we need only to have the ridge shorter than the waveguide; these ends are severely cutoff at 2.45 GHz and will reflect almost 100% of the incident power if they are just a few evanescent lengths long. The evanescent length is

$$\frac{1}{\alpha} = \frac{C}{2\pi f} \frac{1}{\sqrt{1 - (\frac{f}{f_c})^2}} . \qquad (4)$$

For $f = 2.45$ GHz and $f_c = 4.3$ GHz, $1/\alpha = 2.8$ cm.

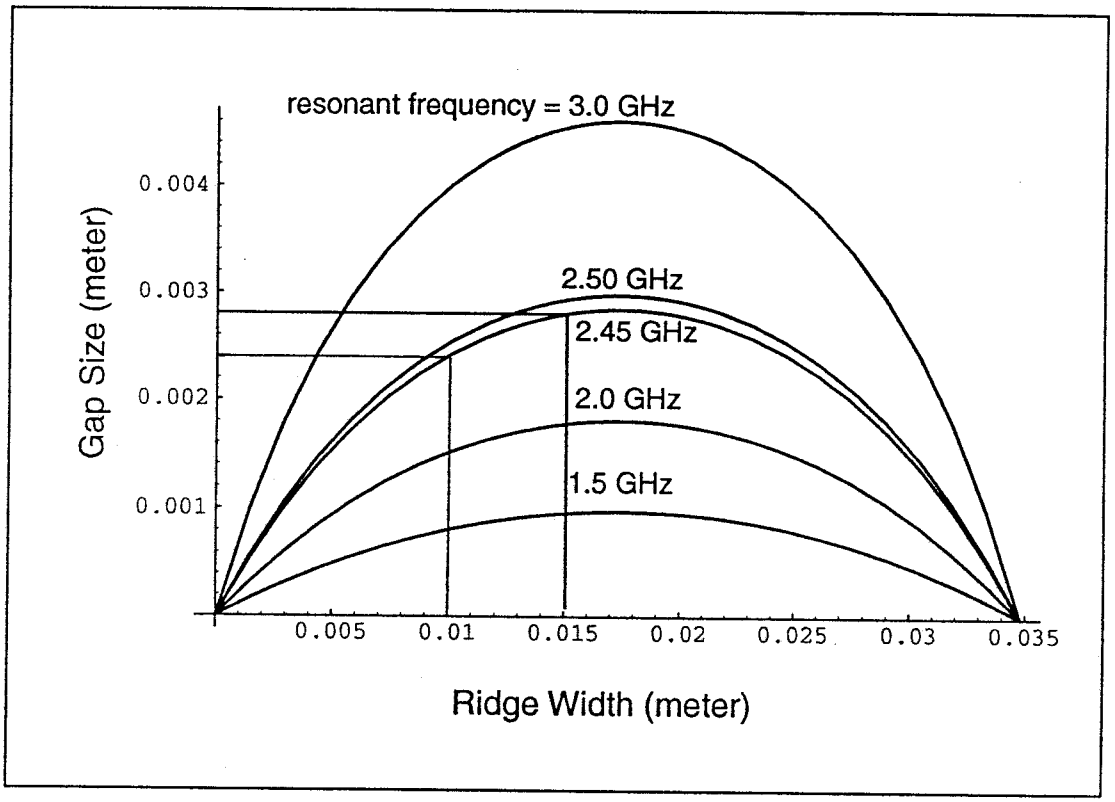

Figure 3. Cutoff conditions for the single ridge waveguide made from a standard WR-137 waveguide (34.8×12.4 mm^2). A 15 mm wide ridge and a 2.8 mm gap or a 10 mm wide ridge and a 2.4 mm gap makes the waveguide cutoff at 2.45 GHz.

§6.3 Experiments with Microwave Excitation

6.3.1 Measurement and cold test with the ridge waveguide

We measured the power distribution in the ridge waveguide in both the transverse and longitudinal directions and fine tuned the position and dimension of the ridge so that it was very close to the cutoff under the cold test conditions. The test setup is shown in Figure 4. Six small holes were opened on top of the ridge waveguide to monitor the field distribution along the direction of ridge. A small antenna can be inserted into the ridge waveguide from one end, and placed very close to the end of the ridge. Then the antenna was moved along the lateral direction across the ridge to measure the field distribution between the ridge and the top waveguide wall along this direction.

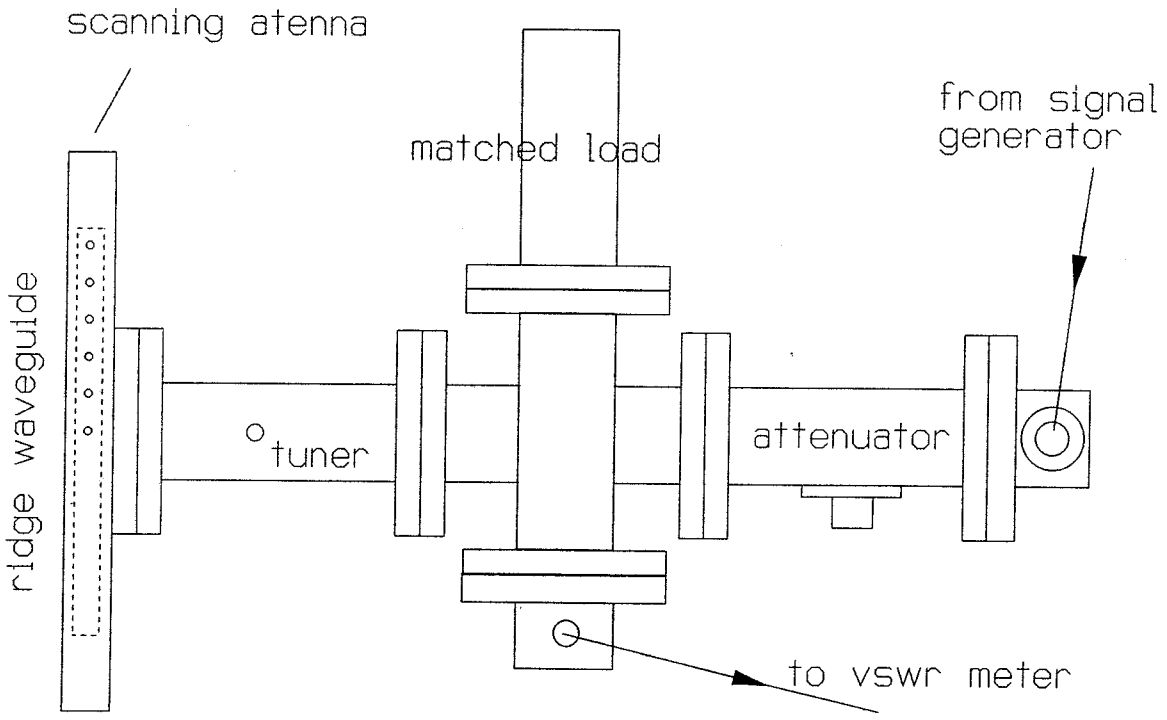

Figure 4. The setup for measuring the cutoff of the ridge waveguide.

It turned out that the 15 mm wide ridge we designed for cutoff at 2.45 GHz actually cutoff at 2.26 GHz. The discrepancy should be attributed to the finite length of the waveguide. When the frequency decreases to near the cutoff, the guide wavelength approaches infinity. Thus the length of the ridge waveguide is inevitably smaller than a wavelength. This introduces considerable error in our calculations, which assume the waveguide is infinitely long by ignoring the scattering at both ends. We found that one way to fine tune the cutoff frequency, without changing the shell waveguide and or ridge dimension, was to change the location of the ridge in the lateral direction, as indicated in Figure 5. This can be explained with the equivalent resonant circuit of the ridge waveguide[6], as shifting the ridge off center shortens the wall length on one side of the ridge waveguide, and reduces the total inductance and raises the cutoff frequency. The measured transverse field distribution is given in Figure 6a, and the measured longitudinal distribution in Figure 6b.

The cutoff frequency for the 10 mm wide ridge was slightly smaller than the designed cutoff frequency also. The step we took to remedy this was to reduce the height of the ridge so it could remain in the center of the waveguide. The measured transverse field distribution is given in Figure 7.

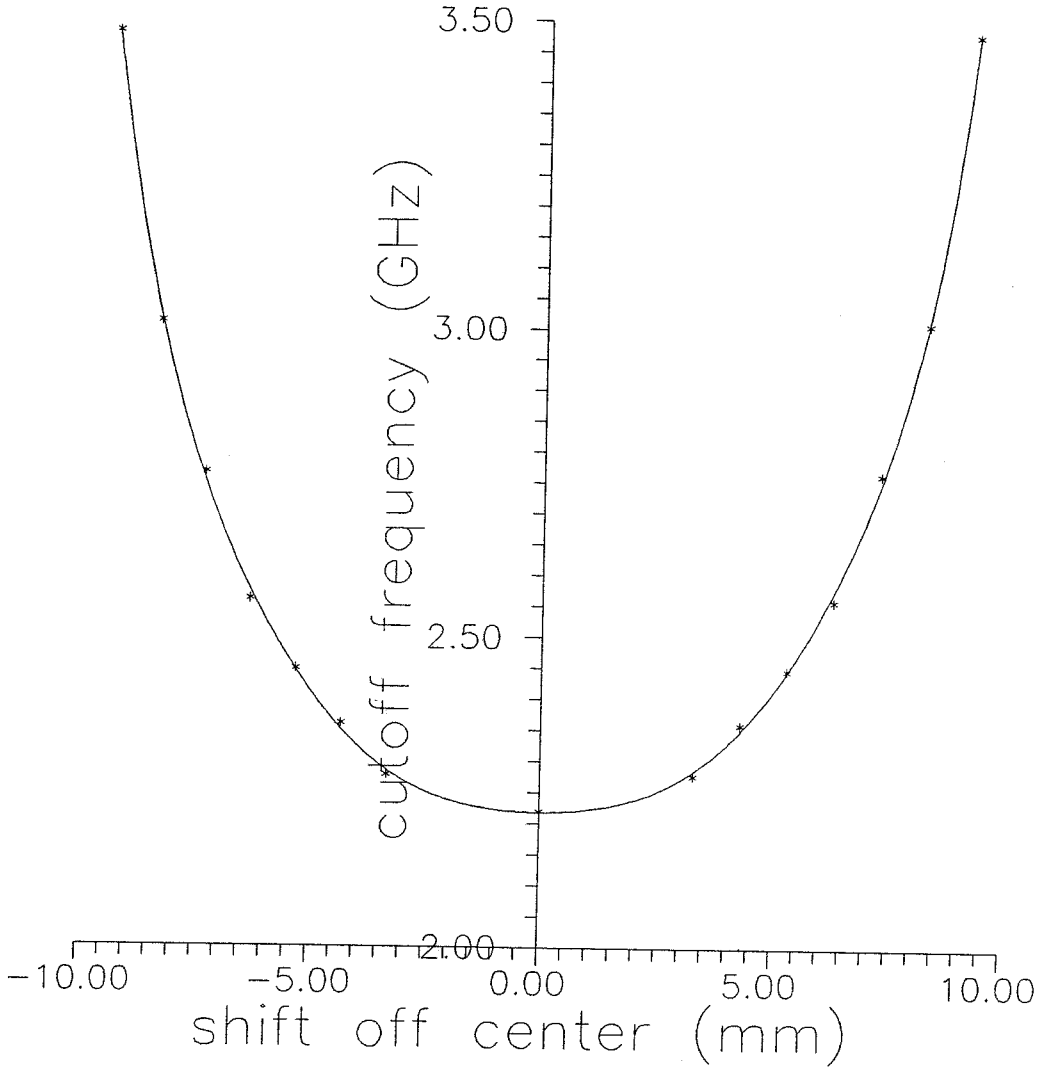

Figure 5. Measured cutoff frequency as a function of the off-center shift of the 15 mm ridge. Notice the curve is flat at the center. Thus if the shift is very small, the tuning can be very accurate.

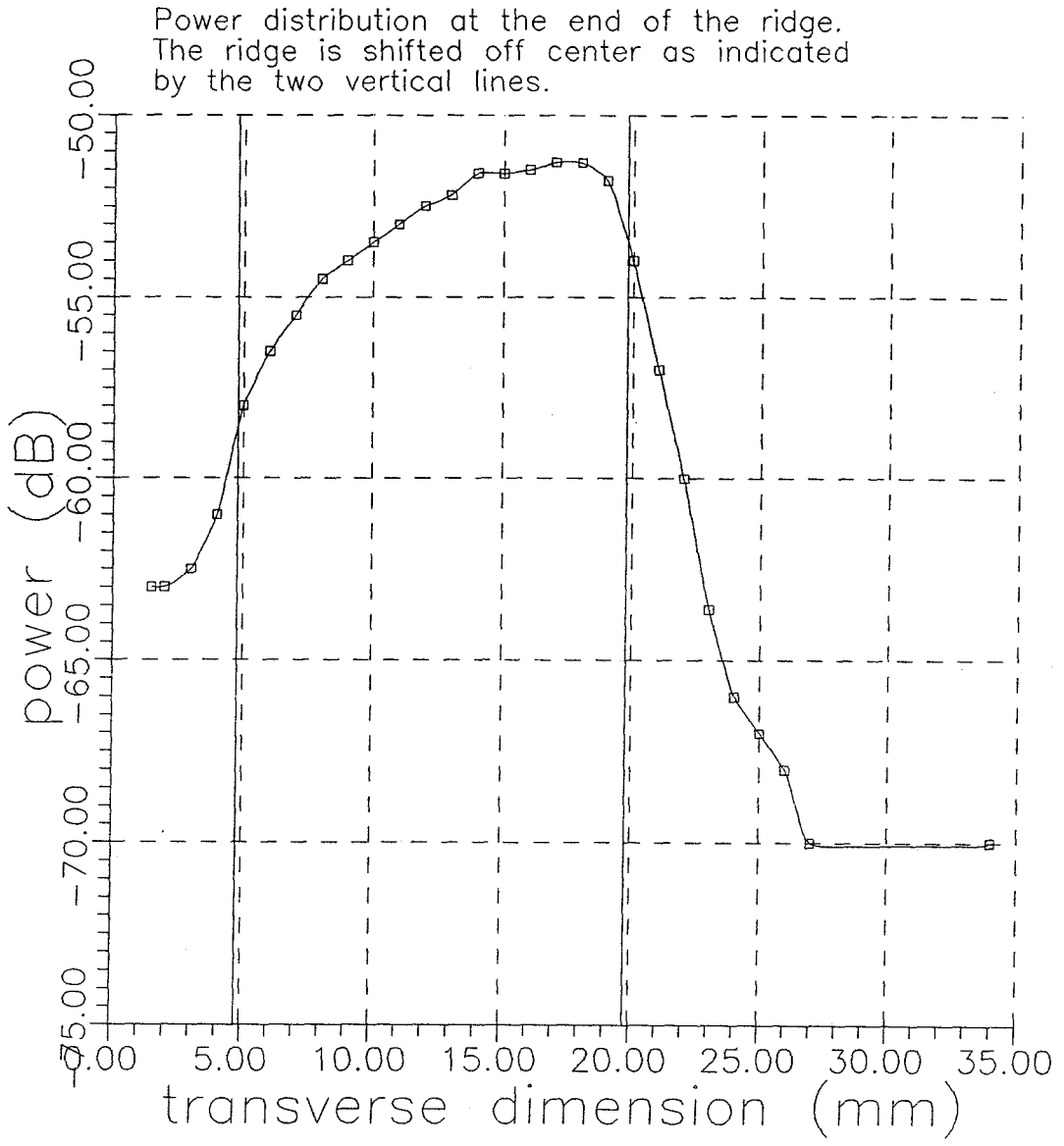

Figure 6. (a) The lateral field distribution in the ridge waveguide with the ridge off center. The total waveguide width is 34.8 mm, ridge width is 15 mm. The flat part of the curve at right indicates the noise level. (b) Longitudinal field distribution at different frequencies around 2.45 GHz.

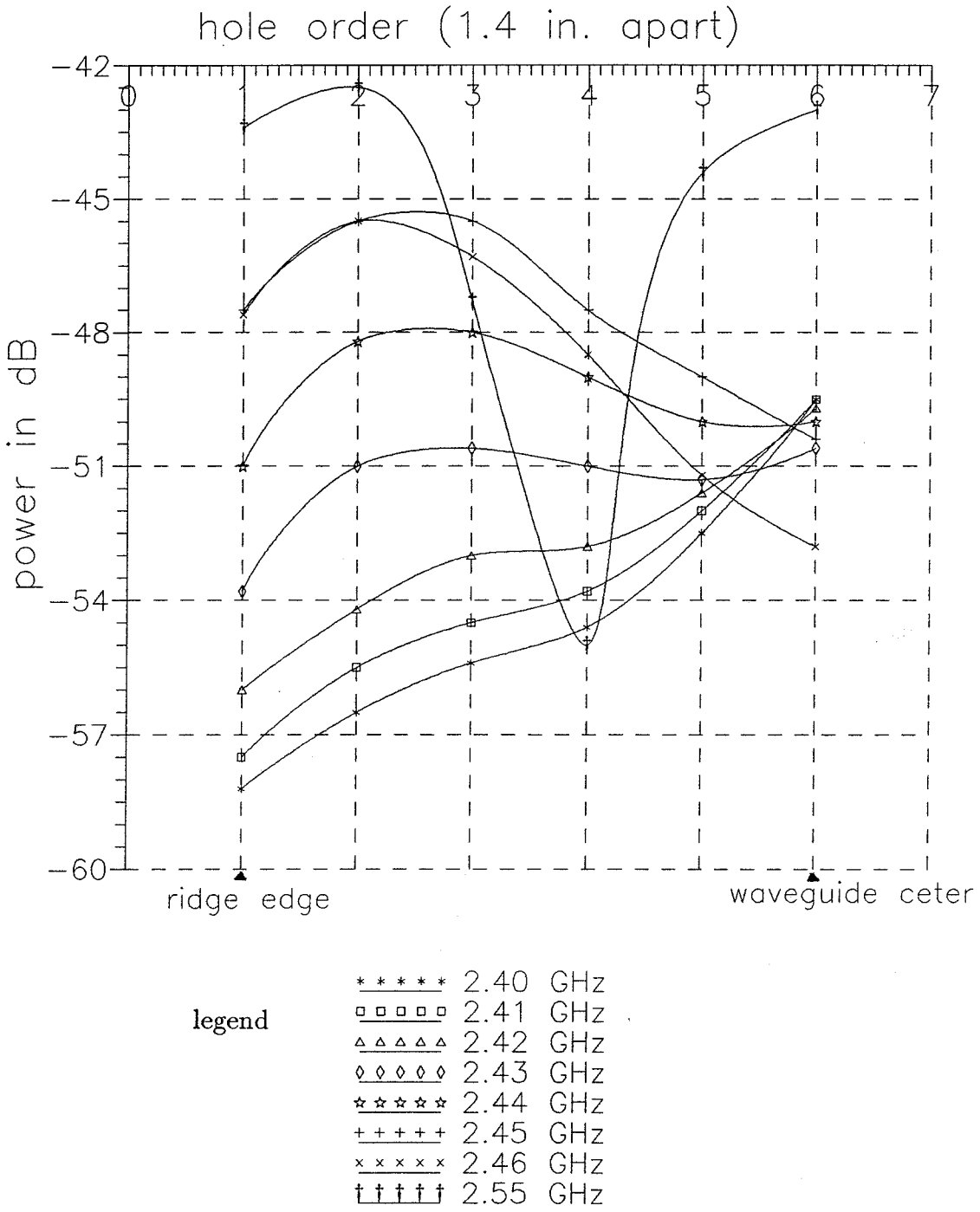

Figure 6. (b) The longitudinal field distribution at frequencies around 2.45 GHz in the ridge waveguide with the ridge off center. The total waveguide width is 34.8 mm; ridge width is 15 mm.

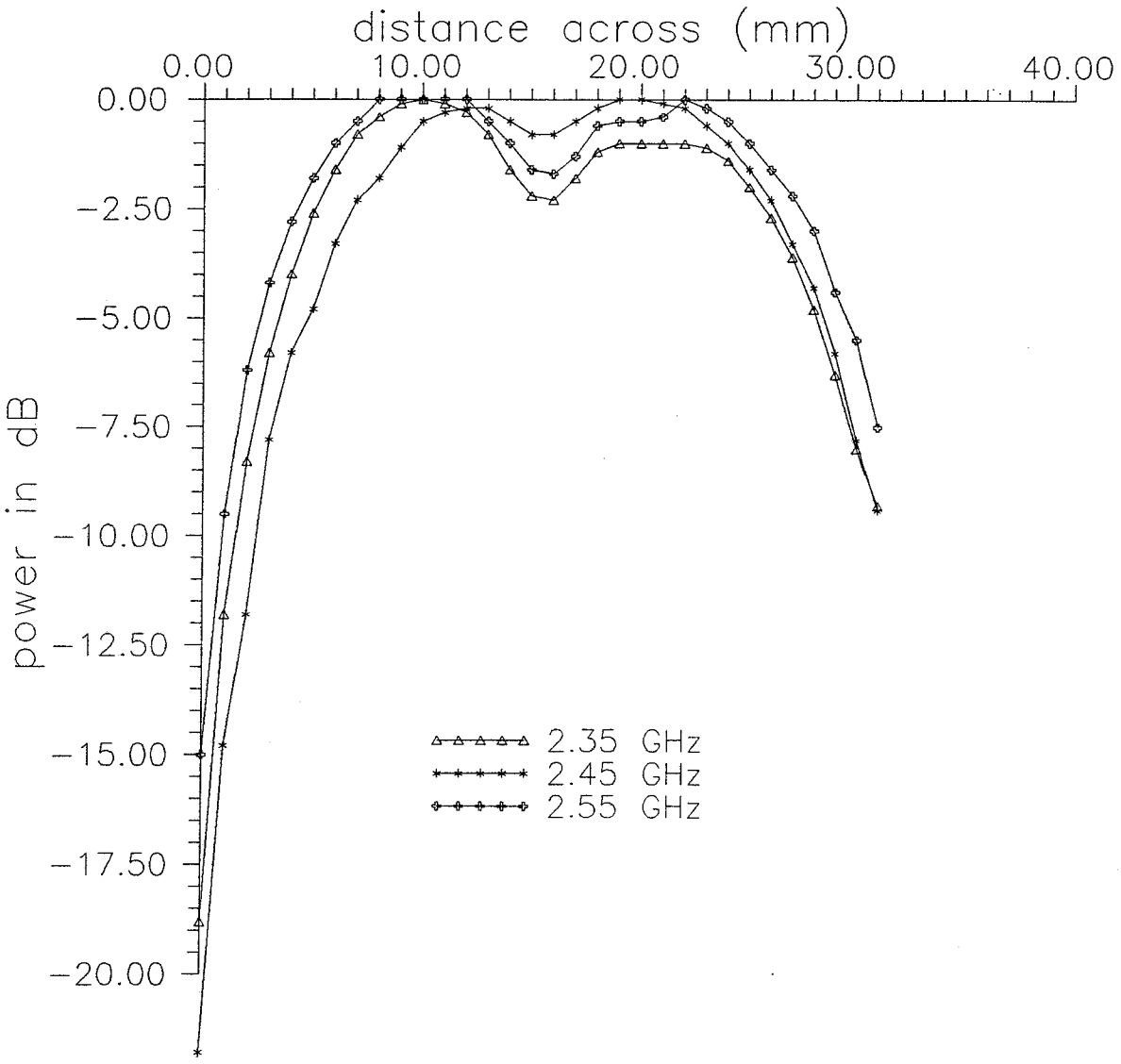

Figure 7. The lateral field distribution in the ridge waveguide with the ridge at the center. The total waveguide width is 34.8 mm; ridge width is 10 mm.

6.3.2 Experiments with microwave excitation

We tested the 15 mm ridge waveguide to investigate the conditions for obtaining a uniform discharge with 2.45 GHz microwave. The test setup is shown in Figure 8. A microwave oven magnetron rated at 750 watts average power was used as the RF power source, driven by a rectified DC power supply. The output of the magnetron was connected to a section of standard S-band waveguide, WR-284, in which a block of dielectric material, Rexolite, of half a guide-wavelength long forms the "half-wave vacuum window." Following this window we used a three-screw tuner for matching the discharge loaded laser section with the magnetron. The center of the discharge section, i.e., the ridge waveguide built from WR-137, was connected to the end of the tuner to form a T shape. To help reduce the reflection due to the discontinuity in heights between the ridge waveguide and WR-284, a ramp was added in front of the ridge, making a gradual change of the waveguide height as indicated in Figure 8.

The most difficult problem we have to face in high-frequency, high power excitation of a gas discharge is the following: We want to maintain a very low SWR to transfer a maximum amount of power to the plasma from the power source. Yet we also want to build up a high field strength on top of the ridge to start the discharge, which means the discharge chamber should be resonant with the driving frequency before the discharge strikes, yielding very high SWR. This initial high SWR is the major problem we have encountered so far. It results in the internal arcing at points other than the ridge. Such arcs have damaged Rexolite vacuum window very often, resulting in contaminated gas and vacuum leakage. It also led to unwanted discharges between the tips of the tuner screws and the bottom of the waveguide. This problem was so persistent that we abandoned the three-screw tuner altogether.

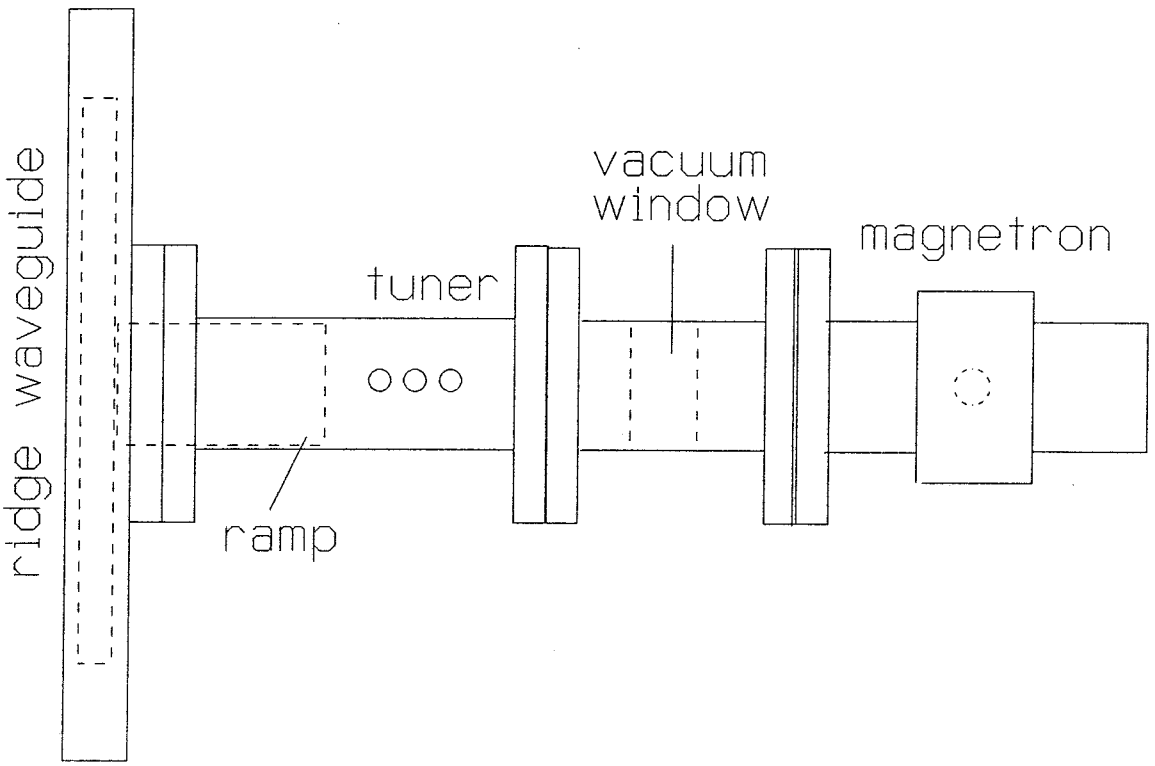

(a)

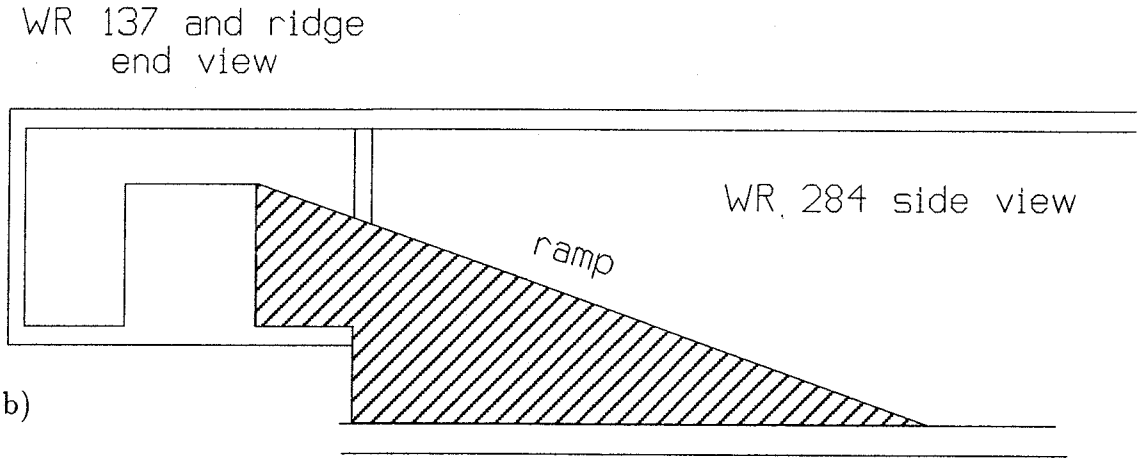

(b)

Figure 8. The microwave discharge test setup in a ridge waveguide, including a three-screw tuner. Ridge width is 15 mm. (a) The top view, and (b) the side view of the WR-284 waveguide and end view of the ridge waveguide.

We tested a second setup without the screw tuner. In this setup the vacuum front window is the only thing in between the magnetron and the ridge waveguide, but there is a sliding short on the other side of the ridge waveguide that we intended to use as a tuning device. A second ramp was added to help reduce the discontinuity in heights to this WR-284 extension. This movable short was separated by another vacuum window from the ridge waveguide. A sketch of this setup is given in Figure 9. Although we located the surface of the vacuum windows in nulls of the voltage standing wave, the high SWR was still a problem, for the vacuum window on the magnetron side was still burned after 20 seconds of discharge, slightly longer than when the three-screw tuner was present. The vacuum window on the sliding short side was not damaged, because most of the reflection was caused by the ridge waveguide.

The section of WR-137 was 380 mm long, and the ridge was chosen to be 270 mm long. Thus we had a 55 mm section of empty WR-137 waveguide on each end that was far bellow the cutoff frequency. The microwave power was reflected from these sections and only a little leaked out. The U.S. safety standards for microwave radiation at this frequency is 1 milliwatt per square centimeter. We measured the leakage with a relative method: We assume that the commercial microwave ovens all comply with this standard and measured the leakages from two microwave ovens in use in Caltech buildings using a commercial microwave leak detector (Tenma 72-220). We found the leakage from both ends of the ridge-waveguide to be smaller than the oven leakage. We then concluded that the leakage of our waveguide was below the U.S. safety standard.

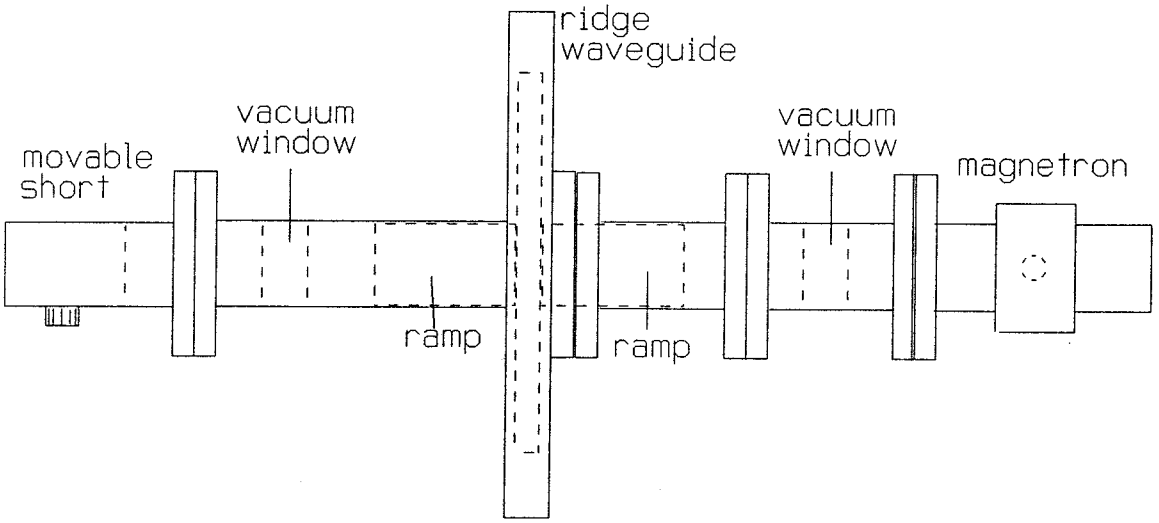

(a)

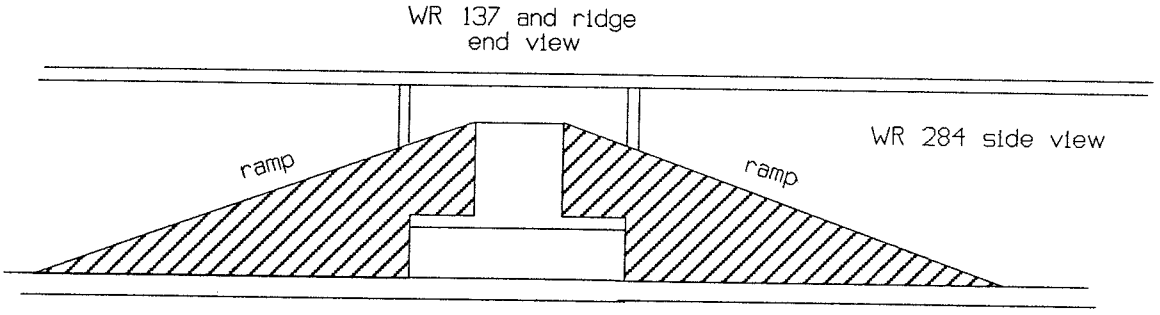

(b)

Figure 9. The second test setup for microwave excitation in a ridge waveguide. (a) The top view, and (b) the side view.

6.3.3 Future plans

The next step we plan to take is to use quartz vacuum windows, which hopefully will be able to endure large SWR and thermal shock, and thus will not break down. This would allow us to do some fine adjustment of the ridge position and find the resonant position with the magnetron frequency. Also, we have designed another transition scheme to direct the microwave into the ridge waveguide, in which the ridge waveguide section is parallel to the WR-284 waveguide. The ridge comes up gradually from within the WR-284 section and ramps up to the full height into the ridge section. The required length of the ramp ridge section, according to Moreno[9], is one guided wavelength long, in order to effectively reduce the reflection due to the discontinuity of the transition. We hope that this transition will expose the full length of the ridge section under microwave and make the discharge uniform. This design is shown in Figure 10. Although not suitable for a laser as it is shown, we feel that we must understand the discharge better before we can design a configuration that will allow both a good discharge and a good optical path. This will have to be accomplished in future experiments.

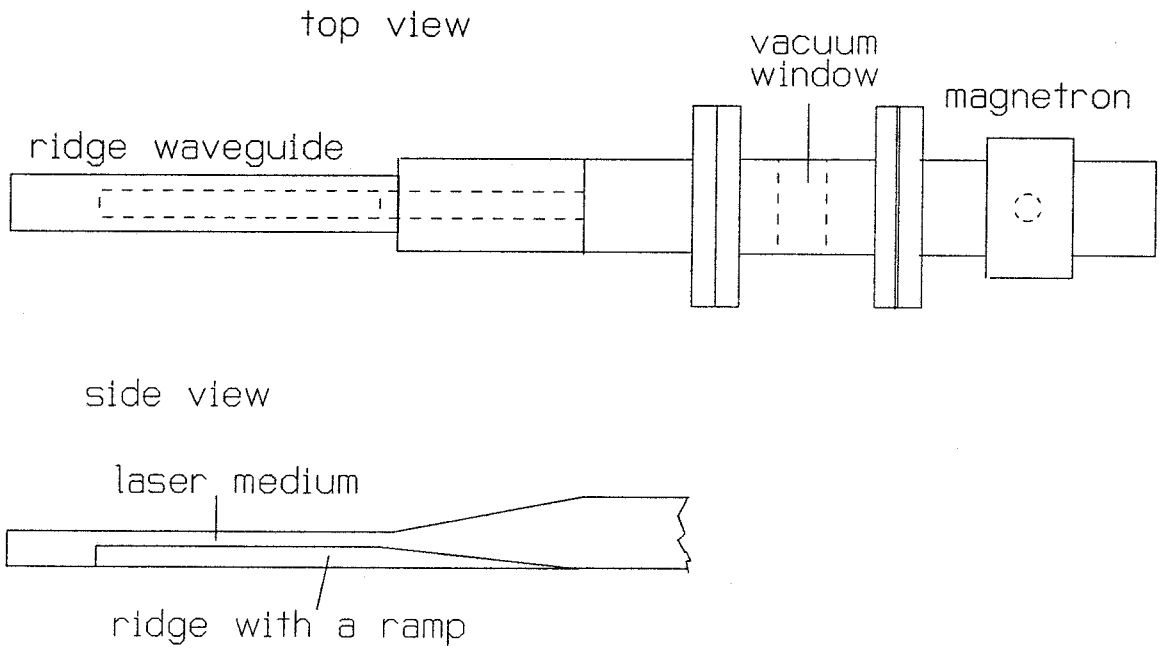

Figure 10. A suggested test setup for microwave excitation in a ridge waveguide. WR-284 waveguide and the ridge waveguide are in parallel.

REFERENCES

1. K.G. Handy and J.E. Brandelik, "Laser Generation by Pulsed 2.45-GHz Microwave Excitation," J. Appl. Phys., Vol. 49, No. 7, pp. 3753–3756, July 1978.

2. B. Freisinger, J.H. Schafer, J. Uhlenbusch and Z.B. Zhang, "Investigation of a 1-kw CO_2 Laser Excited by Microwaves," CLEO '89, THG3, Baltimore, MD, May, 1989.

3. D.R. Hall and C.A. Hill, "Radio Frequency-Discharge-Excited CO_2 Lasers," Handbook of Molecular Lasers, Edited by P.K. Cheo, Marcel Dekker, 1987.

4. A.J. Mendelsohn, R. Normandin, S.E. Harris and J.F. Young, "A Microwave-Pumped XeCl* Laser," Appl. Phys. Lett., Vol. 38, No. 8, pp. 603–605, 15 April, 1981.

5. S. Ramo and J. R. Whinnery, Fields and Waves in Modern Radio, John Wiley and Sons, 1944.

6. S.B. Cohn, "Properties of Ridge Waveguide," Proc. IRE, Vol. 35, pp. 783–788, August 1947.

7. T. Chen, "Calculation of the Parameters of Ridge Waveguides," IRE Transactions of Microwave Theory and Techniques, Vol. MTT-5, pp. 12–17, January 1957.

8. J.R. Whinnery and H.W. Jamieson, "Equivalent Circuits for Discontinuities in Transmission Lines," Proc. IRE, Vol. 32, pp. 98–116, February 1944.

9. T. Moreno, Microwave Transmission Design Data, Dover, 1958.

CHAPTER 7. SOME NEW IDEAS ON FUTURE RESEARCH

§7.1 A New Type of Optical Switch

Through analysis and experiments with two-element laser arrays, we have found that such arrays possess some special properties for an optical device:

(1) The array oscillation mode can be determined by the loss and gain in a very small portion of its total volume. The large portion of the gain volume in the two channels provides the power, while the gain or loss in the inter-element region provides the mode discrimination, and hence, switching.

(2) The loss or gain value does not have to change very much to switch the oscillation from one stable spatial mode to another. In the case of CO_2 lasers calculated in §2.4, a three-fold increase in the loss can switch the array from the in-phase coupled mode to the out-of-phase coupled mode.

(3) These two spatial modes (in-phase and out-of-phase coupled modes) have distinct far-field intensity distributions that basically do not overlap with each other.

These properties should be the same for two-channel laser arrays with other gain media, although the mathematics may be somewhat different due to the possibly different situation properties of the laser. This effect can be used to re-distribute the laser power spatially. Also, the two far-field mode patterns can be used to represent two logic states. Thus a two-element laser array can be used as an binary optical logic switch. Optical logic devices with three states should also be possible: Our experiments described in §5.3 showed that if the gain in the array channels expands too much into the inter-element region, the gain distribution becomes more or less uniform, thus the high order Gaussian mode takes over as the main oscillating mode. And this Gaussian mode had four lobes instead of the three that would have been dictated by the three-channel array structure. If this

also happens in two channel array, e.g., by selecting the width of the channels and the gain distribution we can elect to have a three-lobed Gaussian mode oscillate, then can make a thrinary switch among these three modes (states):

(1) The in-phase coupled mode with a single lobe at the far-field. The array has well-separated gain regions and small loss in the inter-element region.

(2) The out-of-phase coupled mode with a twin lobe at the far-field. The array has well-separated gain regions and large loss in the inter-element region.

(3) The second-order Gaussian mode with three lobes in the far-field. The laser has more-or-less uniform gain distribution across its width direction. It is not a coupled array anymore, but rather a single slab laser as described in Chapter 4.

The theoretical far-field intensity distribution for these three states are shown in Figure 1.

The near-field intensity of the in-phase coupled mode and the out-of-phase coupled mode are almost identical in their spatial distributions, with the exception of the inter-element region where they exhibit a small difference. Thus any mode discrimination method needs to be applied to this region, which occupies only a small portion of the total array volume, e.g., ten percent as indicated in §2.4. This small volume leads to small capacitance and hence lends itself to fast switching applications.

The switching can be triggered by controlling the gain or loss in this region, either optically or electrically or even mechanically.

For gain control electrically, suppose the laser is excited by electrical means; we can have three separate regions of excitation. The two side-electrode pairs do not need to be adjusted and they deliver most of the power. The central region can be switched on slightly or partially to favor the in-phase coupled array mode, or it can be turned off to favor the out-of-phase coupled mode, or it can be turned

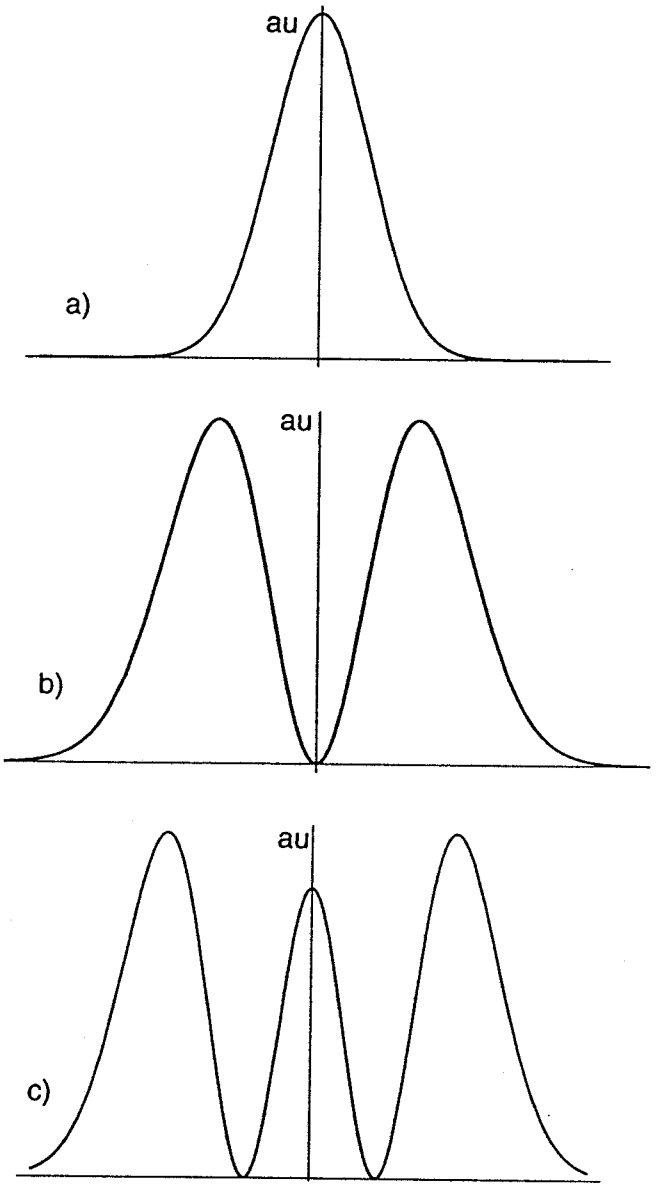

Figure 1. Salient features of the far-field intensity distributions for the two-channel laser array, suggested to represent three logical levels: (a) in-phase coupled mode, (b) out-of-phase coupled mode, and (c) a second order Hermite-Gaussian mode from the same array as the channel separation is filled with gain.

on completely to favor the slab waveguide high order Gaussian mode. Thus the trinary operation is realized.

To control gain optically, one might excite the array so that the in-phase coupled mode would oscillate, and then take the far field and feed it back by focusing it (possibly after some amplification) to the center of the laser cavity. This beam will bleach the gain locally so the out-of-phase coupled mode becomes the mode favored to oscillate. This, in turn, will reduce the center far-field intensity to zero, and thus eliminate the power in the feedback path and cause the gain in the inter-element region to recover, along with the in-phase coupled mode. This makes an all-optical binary multi-vibrator or pulse oscillator, the time constant of which is determined by the feedback path length or the time it takes for the modes to switch in the cavity, whichever is longer. Ozeki et al.[1] pointed out that the speed of switching between two modes of semiconductor lasers based on saturation phenomenon can be much faster than the traditional on-and-off method. They argue that in the former, the changes in carrier populations can be minimized if there is substantial overlap between the modes, and since there is always one mode lasing, the carrier lifetimes are shortened appreciably by ***stimulated*** emission; while in the latter, the switching speed is limited by the ***spontaneous*** carrier lifetime in the active region.

For loss control, we could excite the array in a way so that the in-phase coupled mode would oscillate, and then add some loss in the inter-element region electronically, in order to switch the mode to the out-of-phase coupled mode. One way to do this electronically in semiconductor lasers would be to bias the inter-element region so it becomes lossy and this would switch the laser to the out-of-phase coupled mode. The laser will flip between the in-phase and out-of-phase modes when the reverse bias current is turned off and on.

Another method that falls into the optically-controlled-loss category would be to excite the array so that the out-of-phase coupled mode oscillates, with some of the loss in the inter-element region being saturable, e.g., a piece of unexcited laser medium. If a beam is focused on a saturable loss region, it would be bleached and become transparent, thus causing the in-phase coupled mode to replace the out-of-phase mode. When this control beam is withdrawn or blocked, the array returns to the out-of-phase coupled mode. We can make this device bistable by sampling at the center of the far-field and then feed back the sample, amplified if necessary, to the lossy region. This way, once the in-phase coupled mode starts to oscillate, it will keep the loss bleached and maintain itself, even if the outside trigger source is withdrawn, until the feedback beam is re-directed, blocked, or some additional loss is added to the region beyond its focal area. The device will then stay in the out-of-phase coupled mode.

The two-element array can also be used as a multiple-modulation device: while the total intensity is modulated by some signal, the distribution of the intensity may be modulated by another signal. For example, the total intensity of a semiconductor laser array can be modulated by the injection current in an analog fashion, and the supermode switched according to some digital information.

The basic scheme of binary pulse code of this array can provide better error probability than the conventional on-and-off switching because it is antipodal as compared to the uni-podal scheme of the on-and-off switching.

§7.2 Two-Dimensional Arrays of Discharge Lasers

The linear array of groove-coupled strip waveguide CO_2 lasers in Chapter 5 has astigmatism as shown in Figure 5 of §5.4. In applications that require high power densities, this has to be corrected with additional optics. Two-dimensional arrays would avoid this disadvantage and at the same time increase the power density per laser length. Two-dimensional array of lasers has been a hot topic in semiconductor, surface emitting quantum well lasers. Our proposal here would be the first in gas medium lasers, and it can also be applied to lasers of other media. The basic element of a 2-d array is made of two cross-positioned dual-channel linear arrays, which can be considered as an array of four elements, as shown in Figure 2. If all the four elements are designed to oscillate in the lowest cosine-Gaussian hybrid mode, and the distance between the elements and the electrode gap are properly selected; we know from Chapter 5 that the two parallel elements can be coupled in-phase. To make a two-dimensional array, we will then need to couple two perpendicular linear arrays together. However, these two linear arrays have to oscillate in the same polarization in order to couple. Thus if the horizontal array oscillates in the TE mode, then the vertical array needs be in the TM mode, and *vice versa.* TE_1 and TM_1 modes for a pair of infinite plate waveguide have the same propagation constant. Thus we can expect these two modes in the perpendicularly oriented two waveguides of the same geometry in the laser cavity to have the same natural oscillation frequencies. In reality, however, even if a small frequency discrepancy exists, the two modes can still couple. In the tests described in Chapter 5, we measured the polarization of the array to be parallel to the surfaces of the electrodes. That is to say we had TE modes. For a pair of aluminum surface which has large conductivity, the TE modes suffer the least loss so they start to oscillate first. In the two-bore ceramic

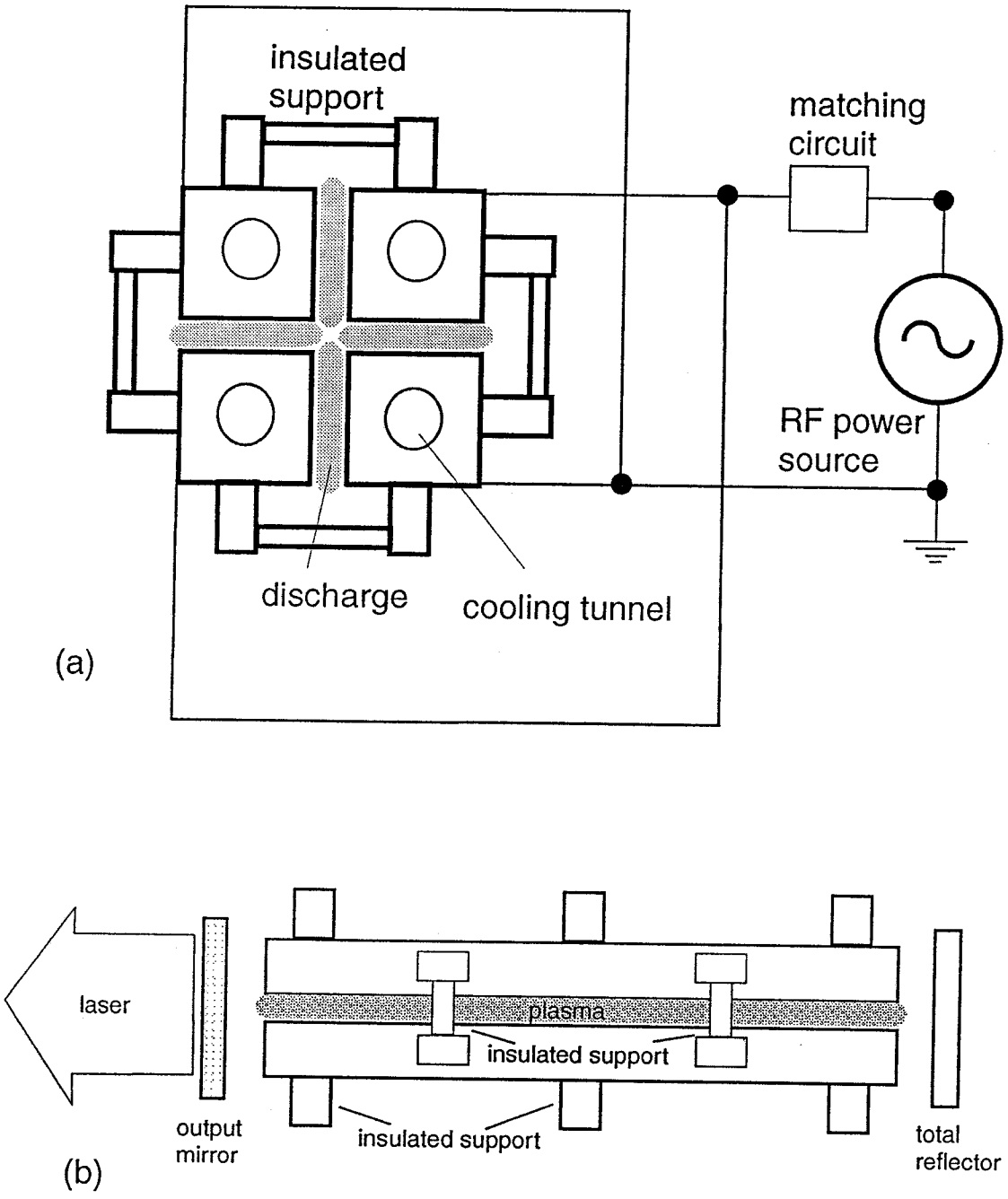

Figure 2. The suggested two-dimensional discharge laser array: (a) Cross section view, (b) side view at a reduced size to fit the page.

array described in Chapter 3 with the top plate being aluminum, the polarization was such that the electric field was perpendicular to the ceramic (alumina) side walls. Also from the calculations made in Chapter 4 for aluminum plate waveguides coated with Al_2O_3 (alumina), the loss to TM modes decreased drastically for the coating thickness above 2 μm (see Figure 7b in §4.3). Thus it should be possible that for a pair of electrodes coated with alumina, or anodized, the TM mode loss would be much less, so it can also oscillate, as long as the tendency for the TE mode to oscillate is suppressed. On the other hand, the TE mode in the alumina-coated waveguide may still oscillate because it may still have less loss than the TM mode as indicated in Figure 6 and Figure 7b in §4.3. In such a case it may become necessary to use a Brewster window to force the parallel polarization.

The electrode structure in Figure 2 is a so-called quadrupole electrode, with adjacent electrodes having opposite polarity and diagonal ones, the same polarity. The size of the center gap may be critical in obtaining an in-phase coupled array mode.

Once this four-element 2-d array is demonstrated, it can be grouped together to form arrays with even more elements. Such a laser array will need to have its back mirror made with holes on the center of each of the electrodes, so that cooling water and electric connections can be fed through the mirror. The electrode has to be water cooled in the center. It actually plays three roles: electric conduction for the pumping, waveguiding for the laser light, and thermal conduction for cooling. It also needs to be mechanically strong.

We have so far been discussing arrays of waveguide lasers. As we reported in §5.3, phase-coupled laser arrays can be made from free space Gaussian mode lasers as long as there is enough leakage among the elements in the active

its elements, instead of the waveguide laser.

The far field intensity distribution from a 2-d array cell was simulated in the computer, and is given in Fig.3. We see there are some side lobes in all four directions, but if the gap between the electrodes is not too narrow, the center lobe still possesses a considerable amount of power.

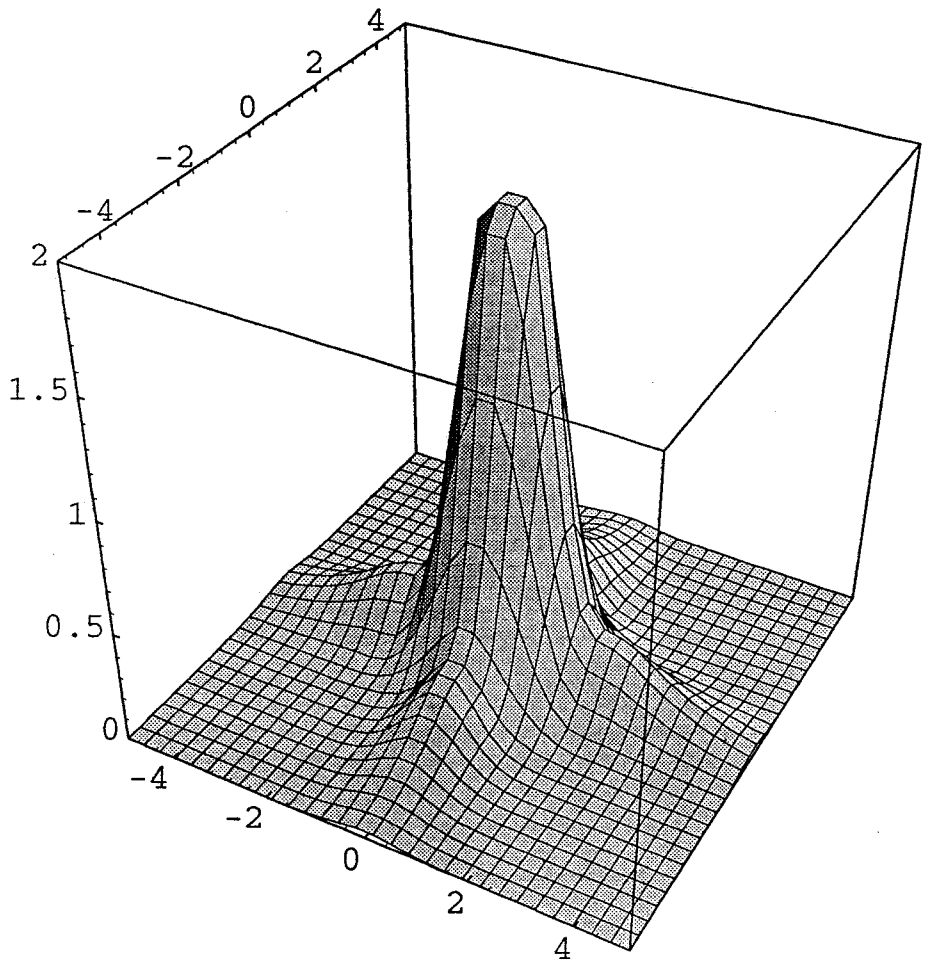

Figure 3. Far-field intensity distribution of a four-element, two-dimensional waveguide laser array. Each element has a cross section of 2 mm by 3 mm.

REFERENCES

1. Y. Ozeki, J. E. Johnson and C. L. Tang, "Polarization Bistability in Semiconductor Lasers with Intracavity Multiple Quantum Well Saturable Absorbers," Applied Phys. Lett., Vol. 58, No. 18, pp. 1958–1960, May 6, 1991.